Alma Mater Studiorum · Università di Bologna

SCUOLA DI SCIENZE
Corso di Laurea in Astrofisica e Cosmologia

Constraining the cosmological parameters through the galaxy cluster mass function in the AMICO KiDS-DR3 catalogue

Relatore:
Dr. Federico Marulli

Correlatori:
Ch.mo Prof. Lauro Moscardini
Dr. Alfonso Veropalumbo

Candidato:
Giorgio, Francesco Lesci

Sessione III
Anno Accademico 2018/2019

Contents

Abstract

The large-scale matter distribution of the Universe plays a key role in shading lights on the physical properties of dark matter, dark energy, and gravity at cosmological scales. During the last decades, several multi-band surveys have been undertaken to collect representative samples of cosmic tracers. Aiming at reaching an accurate and precise characterization of the Universe on the largest scales, the combination of independent methods and observations is employed. Among the main probes that will provide the answers to the most challenging questions in cosmology and fundamental physics, galaxy clusters play a crucial role. Reaching masses larger than $10^{15}\,\mathrm{M}_{\odot}$, galaxy clusters are the biggest virialized structures in the Universe, tracing the highest peaks of the dark matter density field. In particular, the mass function of galaxy clusters has a fundamental role in cosmology, given its dependency on fundamental cosmological parameters.

In this Thesis work, we consider the specific mass regime of galaxy clusters, since these objects mark the transition between the linear and the non-linear regime of the gravitational perturbations, so that their formation and evolution can be theoretically described with excellent accuracy. The dark matter component is dominant in galaxy clusters. Therefore it is accurate enough, given current observational uncertainties, to model the cluster mass function through N-body dark matter simulations, thus neglecting the astrophysical effects due to the baryonic matter component. In fact, the cluster statistical properties can be linked directly to the physical quantities of their host dark matter haloes, which depend on the cosmological model parameters. During the last few years, galaxy cluster observations have begun to provide strong constraints on cosmological parameters, making these objects fundamental tools to test the standard cosmological model, the so-called Λ-cold dark matter (ΛCDM) model.

In this Thesis, we present a new cosmological analysis of cluster counts, exploiting the AMICO KiDS-DR3 catalogue (Maturi et al. 2019), which is a sample of photometrically-selected galaxy clusters, built up through the use of the cluster detection algorithm called Adaptive Matched Identifier of Clustered Objects (AMICO) (Bellagamba et al. 2018), on the third data release of the Kilo Degree Survey (KiDS; de Jong et al. 2017). The catalogue contains 7988 candidate galaxy clusters, in the redshift range $z \in [0.1, 0.8]$, on an effective area of $377\,\mathrm{deg}^2$. We develop a method to assign a statistical weight to each object

in the catalogue, by deriving the selection function of the sample from a mock catalogue. Exploiting the results of the weak-lensing analysis provided by Bellagamba et al. (2019), we derive the masses of the objects. Then we develop two cosmological pipelines in order to retrieve in a ΛCDM Universe the constraints on the matter density parameter, Ω_m, the normalization of the power spectrum, σ_8, and the cluster normalization condition parameter, $S_8 = \sigma_8(\Omega_m/0.3)^{0.5}$, fixing the other parameters at the values obtained by Planck Collab. (2018). In order to accomplish this task, we introduce a new model for the cluster counts. Subsequently, we implement in the analysis a peculiar source of uncertainty, namely the super sample covariance, aiming at accounting for systematics that intrinsically affects our data. We derive the following constraints: $\Omega_m = 0.28^{+0.01}_{-0.01}$, $\sigma_8 = 0.85^{+0.02}_{-0.01}$, $S_8 = 0.82^{+0.01}_{-0.01}$, which are consistent with ΛCDM predictions, and competitive, in terms of uncertainties, with results of state-of-the-art cluster number count analyses.

The whole cosmological analysis of this Thesis work has been performed with the CosmoBolognaLib (CBL; Marulli et al. 2016), a large set of *free software* C++/Python libraries, that provide an efficient numerical environment for cosmological investigations of the large-scale structure of the Universe. The new likelihood model for the cluster number counts, as well as the whole formalism for the super sample covariance, which have been originally developed for this Thesis work, will be released in the forthcoming public version of the CBL.

Sommario

La distribuzione della materia a grande scala nell'Universo ricopre un ruolo cruciale nel fare luce sulle proprietà fisiche della materia oscura, così come su quelle dell'energia oscura e della gravità su scale cosmologiche. Nell'ultimo decennio sono state eseguite diverse survey in multi-banda, al fine di ottenere campioni significativi di traccianti cosmici. Con lo scopo di raggiungere una precisa e accurata caratterizzazione dell'Universo a grande scala, viene sfruttata la combinazione di metodi e osservazioni indipendenti. Tra gli oggetti cosmici più importanti, il cui studio permetterà di dare risposta alle più stimolanti domande nei campi della cosmologia e della fisica fondamentale, troviamo gli ammassi di galassie. Raggiungendo masse maggiori di 10^{15} $M_{\odot}$, questi oggetti sono le strutture virializzate più grandi nell'Universo, e tracciano i picchi più alti del campo di densità della materia oscura. In particolare, la funzione di massa degli ammassi di galassie ha un ruolo essenziale in cosmologia, data la sua dipendenza da parametri cosmologici fondamentali.

In questo lavoro di Tesi, consideriamo lo specifico regime di massa degli ammassi di galassie, poiché tali oggetti segnano il confine tra il regime lineare e il regime non lineare delle perturbazioni gravitazionali, cosicché la loro formazione ed evoluzione può essere descritta teoricamente con eccellente precisione. La componente di materia oscura è dominante negli ammassi di galassie. Di conseguenza, date le attuali incertezze osservative, è sufficientemente accurato modellare la funzione di massa degli ammassi di galassie tramite l'utilizzo di simulazioni a N corpi di materia oscura, trascurando dunque gli effetti astrofisici dovuti alla componente di materia barionica.

Di fatto, le proprietà statistiche degli ammassi possono essere legate direttamente alle quantità fisiche dei loro aloni di materia oscura, le quali dipendono dai parametri del modello cosmologico. Negli ultimi anni, le osservazioni di ammassi di galassie hanno iniziato a fornire forti vincoli sui parametri cosmologici, rendendo questi oggetti degli strumenti fondamentali per testare il modello cosmologico standard, il cosiddetto modello Λ-cold dark matter (ΛCDM).

In questa Tesi, presentiamo una nuova analisi cosmologica di conteggi di ammassi, sfruttando il catalogo AMICO KiDS-DR3 (Maturi et al. 2019), il quale è un campione di ammassi di galassie selezionati fotometricamente, costruito tramite l'utilizzo dell'algoritmo di detezione di ammassi denominato Adaptive Matched

Identifier of Clustered Objects (AMICO) (Bellagamba et al. 2018), sulla terza data release della Kilo Degree Survey (KiDS; de Jong et al. 2017). Il catalogo contiene 7988 candidati di ammassi di galassie, nell'intervallo di redshift $z \in [0.1, 0.8]$, su un'area effettiva di $377\,\mathrm{deg}^2$. Sviluppiamo quindi un metodo che assegna un peso statistico a ogni oggetto nel catalogo, derivando la funzione di selezione del campione da un catalogo mock. Sfruttando i risultati ottenuti dall'analisi di weak-lensing forniti da Bellagamba et al. (2019), deriviamo le masse degli oggetti. Dunque sviluppiamo due pipeline cosmologiche al fine di ottenere, in un Universo ΛCDM, vincoli sul parametro di densità della materia, Ω_m, sulla normalizzazione dello spettro di potenza, σ_8, e sul parametro di condizione di normalizzazione dei cluster, $S_8 \equiv \sigma_8(\Omega_m/0.3)^{0.5}$, fissando gli altri parametri ai valori ottenuti da Planck Collab. (2018). Al fine di raggiungere questo obiettivo, introduciamo un nuovo modello per i conteggi di ammassi. Successivamente, implementiamo nell'analisi una peculiare fonte di incertezza, ovvero la super sample covariance, mirando a tenere conto di sistematiche che affliggono intrinsicamente i nostri dati. Deriviamo i seguenti vincoli: $\Omega_m = 0.28^{+0.01}_{-0.01}$, $\sigma_8 = 0.85^{+0.02}_{-0.01}$, $S_8 = 0.82^{+0.01}_{-0.01}$, i quali sono consistenti con le predizioni del ΛCDM, e competitivi, in termini di incertezze, con i risultati di analisi di conteggi di ammassi allo stato dell'arte.

L'intera analisi cosmologica in questo lavoro di Tesi è stata eseguita con le CosmoBolognaLib (CBL; Marulli et al. 2016), un grande insieme di librerie *free software* in C++/Python, che forniscono un efficiente ambiente numerico per investigazioni cosmologiche della struttura dell'Universo a larga scala. Il nuovo modello di likelihood per i conteggi di ammassi, come anche il formalismo per la super sample covariance, che sono stati in origine sviluppati in questo lavoro di Tesi, saranno rilasciati nella prossima versione pubblica delle CBL.

Introduction

In accordance with the predictions of the standard cosmological framework, the so-called ΛCDM, we live in an expanding Universe whose main components are the dark energy, parameterized in terms of the cosmological constant, Λ, and the cold dark matter (CDM), that constitutes $\sim 68\%$ and $\sim 27\%$ of the energy/matter content of the Universe, respectively. In turn, only $\sim 5\%$ of the Universe is in the form of ordinary matter, which nevertheless provides the most relevant contribution in astronomical and cosmological investigations, as it composes the luminous side of the Universe.

In this context, we describe the large-scale structure of the Universe as the result of the gravitational growth of local density perturbations, within an expanding background. Among the gravitationally bound structures in the cosmos, galaxy clusters play a crucial role in cosmology, tracing the highest peaks of the density perturbations. The development of increasingly advanced instruments to allowed the detection of large galaxy cluster samples in different wavelengths have dramatically enhanced our knowledge of the Universe on large scales. Observations in X-rays, optical and NIR, as well as gravitational lensing studies allow to investigate in depth the statistical properties of objects. In this framework, it is necessary to construct pure and complete galaxy cluster catalogues up to high redshifts, in order to derive cosmological constraints from the physical properties of these structures.

Galaxy clusters are the biggest virialized structures in the Universe, reaching masses higher than 10^{15} $M_{\odot}$. Gravity is the dominant interaction on such large scales, where the information of the initial cosmological conditions is preserved. Conversely, the interactions involving the ordinary matter erase the cosmological information. Nevertheless, for cosmological purposes, the gas physics in galaxy clusters is negligible, given the current uncertainties on cluster statistics measurements. Consequently, it is accurate enough to describe the formation and evolution of galaxy clusters only in terms of the dark matter potential wells. This simplification allows also to exploit N-body dark matter simulations of large volumes of the Universe. Since theoretical models for cluster evolution can be accurately developed, these objects provide remarkable cosmological probes with a wide spectrum of applications.

The two-point correlation function of galaxy clusters can be used in com-

bination to cluster mass measurements to assess the auto-correlation function of the density contrast field (Marulli et al. 2018), and test the gravity theory through redshift-space distortions in the clustering pattern. Another important cosmological probe is provided by the mass function of galaxy clusters, which is highly sensitive to the values of the main cosmological model parameters. Due to the high complexity of the structure formation and evolution, the calibration of the mass function models requires N-body simulations. Several mass function models have been developed in the past decade (e.g. Tinker et al. 2008, Watson et al. 2013; Despali et al. 2016), and a plenty of observational studies of cluster counts have been employed. Recent investigations on cluster counts have derived remarkable constraints on the matter density parameter, Ω_m, the power spectrum normalization, σ_8, and the derived parameter $S_8 \equiv \sigma_8(\Omega_m/0.3)^{0.5}$. Among these studies, Costanzi et al. (2018) obtained the following constraints: $\Omega_m = 0.22^{+0.05}_{-0.04}$, $\sigma_8 = 0.91^{+0.11}_{-0.10}$, $S_8 = 0.79^{+0.05}_{-0.04}$ from a dataset of photometrically-selected clusters detected in the SDSS catalogue. Furthermore, Pacaud et al. (2018) derived $\Omega_m = 0.316^{+0.060}_{-0.060}$, $\sigma_8 = 0.814^{+0.054}_{-0.054}$ from a catalogue of X-ray selected galaxy clusters.

In this Thesis work we extract constraints on Ω_m, σ_8 and S_8 from the AMICO KiDS-DR3 galaxy cluster catalogue (see Maturi et al. 2019). To do this, we develop two alternative pipelines. In the second of them, we improve the formalism of the mass function and we introduce an additional source of uncertainty at the likelihood level, namely the super sample covariance.

This Thesis is organized as follows:

- in Chapter 1, we introduce the modern cosmological scenario, describing the main properties of the Universe in a theoretical context;
- in Chapter 2 we present an overview on the physical properties of galaxy clusters, and the methods employed for their detection;
- in Chapter 3 we outline the importance of the mass function in cosmology, describing the basic theoretical background and the properties of this extraordinary tool;
- in Chapter 4 we describe the dataset this Thesis work is based on, that is the AMICO KiDS-DR3 catalogue;
- in Chapter 5 we present the methods developed for the analysis of the data, along with our results;
- finally, in Chapter 6 we summarize the main results of this Thesis work and discuss the future perspectives.

Chapter 1

Fundamentals of Cosmology

Our aim in this chapter is to describe the main theoretical and observational achievements of modern cosmology. In the first part we will provide an overview of the current mathematical formalism in cosmology, based on the General Relativity and the Friedmann equations. Then the main features of the standard cosmological model, the so called ΛCDM, will be presented, followed by a discussion on the formation and evolution of the gravitational perturbations in the universe.

1.1 Two principles

The scientific study of the universe as a whole, or cosmology, is based on two fundamental principles: the *Fair Sample Principle*, better discussed in Section 1.11, and the *Cosmological Principle*.
The former becomes necessary when we face the problem that the universe is a unique object, not reproducible, and this would imply the impossibility of a statistical approach for cosmological studies. However, the Fair Sample Principle states that considering distinct volumes of universe, sufficiently large in order to be considered independent, is equivalent to consider many realizations of universe.[1]
On the other hand, the Cosmological Principle allows the mathematical description of the universe. It states, indeed, that the universe is homogeneous and isotropic, the two properties at the foundations of the Friedmann-Robertson-Walker metric. Nowadays isotropy is observed in the cosmic microwave background (CMB) and on scales greater than 100 Mpc, i.e. on scales larger than the ones of superclusters and voids. Therefore the only principle is that of homogeneity, or Copernican Principle.

[1] The sizes of the volumes required to satisfy this principle are dependent on the cosmological epoch.

1.2 The central role of General Relativity

The description of the universe relies on a theory of gravitation, the General Relativity (GR, Einstein, 1915). Gravitation is indeed the dominant field on large scales and GR is the best candidate we have to describe it.
In this theory, the content of energy and matter acts on the geometry of the space-time, which is described by the *metric tensor* g_{ij}. The minimum interval between two events in the space-time is expressed as

$$\mathrm{d}s^2 = g_{\alpha\beta}\,\mathrm{d}x^\alpha \mathrm{d}x^\beta \qquad \alpha, \beta = 0,\, 1,\, 2,\, 3, \tag{1.1}$$

where repeated indexes imply summation. In particular, the three space coordinates x^1, x^2, x^3 are generally labeled with the indexes i, j, while the time coordinate is $x^0 = ct$ where t is the proper time. *Timelike* and *spacelike* intervals are respectively related to $\mathrm{d}s^2 > 0$ and $\mathrm{d}s^2 < 0$, while for $\mathrm{d}s^2 = 0$ the interval is called *lightlike* and holds for photons.
Due to the curvature of the space-time geometry, outlined by $g_{\alpha\beta}$, free particles move along non-straight *geodesics*. In particular the integral along the path of a particle is such that

$$\delta \int_{path} \mathrm{d}s = 0, \tag{1.2}$$

and from this equation derives the *geodesic equation*

$$\frac{\mathrm{d}^2 x^\alpha}{\mathrm{d}s^2} + \Gamma^\alpha_{\mu\nu} \frac{\mathrm{d}x^\mu}{\mathrm{d}s} \frac{\mathrm{d}x^\nu}{\mathrm{d}s} = 0. \tag{1.3}$$

The metric tensor is related to the content of energy and matter, defined by the energy-momentum tensor T_{ij}, through the fundamental Einstein's field equations

$$R_{\alpha\beta} - \frac{1}{2} g_{\alpha\beta} R = \frac{8\pi G}{c^4} T_{\alpha\beta}. \tag{1.4}$$

$R_{\alpha\beta}$ and R are, respectively, the Ricci tensor the Ricci scalar, G is the Newton's gravitational constant and c the speed of light. The universe can be described as a perfect fluid with pressure p and energy density ρc^2, so that the energy-momentum tensor has the form

$$T_{\alpha\beta} = (p + \rho c^2) u_\alpha u_\beta - p g_{\alpha\beta}, \tag{1.5}$$

where u_α is the four-velocity of the fluid.

1.3 The Friedmann-Robertson-Walker metric

As discussed in the previous sections, a mathematical representation of the universe is needed in order to attempt to describe it. General Relativity is the core of

the description of the universe, and being this a geometrical theory it is necessary to introduce the functional form of the space-time metric. This is the Friedmann-Robertson-Walker (FRW) metric, based on the Cosmological Principle.
For a homogeneous and isotropic universe, the equation (1.1) can be written more explicitly as

$$\mathrm{d}s^2 = g_{00}\mathrm{d}t^2 - \mathrm{d}l^2 = c^2\mathrm{d}t^2 - \mathrm{d}l^2, \tag{1.6}$$

where the first and the second terms are, respectively, time and space terms. At any instant defined by the proper time t, or *cosmic time*, the spatial metric $\mathrm{d}l^2$ is identical in all the places and directions. The cosmic time varies monotonically and is zero in correspondence of the intersections of all the geodesics of the space-time.
In order to find the suitable form of the three-dimensional spatial metric, the two-dimensional case is considered first. The possible spaces that satisfy the Cosmological Principle are the flat Euclidean space, the sphere and the hyperboloid. In the case of the flat space,

$$\mathrm{d}l^2 = \mathrm{d}x^2 + \mathrm{d}y^2, \tag{1.7}$$

that in polar coordinates $0 \leq \rho < \infty$, $0 \leq \phi < 2\pi$, is expressed as

$$\mathrm{d}l^2 = \mathrm{d}\rho^2 + \rho^2\mathrm{d}\phi^2. \tag{1.8}$$

We can define $\rho \equiv ar$, where a has the dimension of a length while r has no dimension, and $0 \leq r < \infty$. Then the final relation is

$$\mathrm{d}l^2 = a^2(\mathrm{d}r^2 + r^2\mathrm{d}\phi^2). \tag{1.9}$$

In the case of a spherical surface, we have

$$\mathrm{d}l^2 = R^2(\sin^2\theta\,\mathrm{d}\phi^2 + \mathrm{d}\theta^2), \tag{1.10}$$

where R is the radius, $0 \leq \theta \leq \pi$ and $0 \leq \phi < 2\pi$. Imposing $R \equiv a$ and $\sin\theta = r$, the previous equation has the form

$$\mathrm{d}l^2 = a^2\left[r^2\mathrm{d}\phi^2 + \frac{\mathrm{d}r^2}{1-r^2}\right]. \tag{1.11}$$

For an hyperbolic surface, similarly to the spherical case, the equation

$$\mathrm{d}l^2 = R^2(\sinh^2\theta\,\mathrm{d}\phi^2 + \mathrm{d}\theta^2) \tag{1.12}$$

becomes

$$\mathrm{d}l^2 = a^2\left[r^2\mathrm{d}\phi^2 + \frac{\mathrm{d}r^2}{1+r^2}\right]. \tag{1.13}$$

The general expression for $\mathrm{d}l^2$ in two dimensions is then

$$\mathrm{d}l^2 = a^2 \left[\frac{\mathrm{d}r^2}{1 - kr^2} + r^2 \mathrm{d}\phi^2 \right], \tag{1.14}$$

where k is the curvature parameter, and $k = 0$ for the flat space, $k = 1$ for the sphere and $k = -1$ for the hyperboloid. The curvature parameter k is related to the amount of energy and matter densities and defines the sign of the *Gaussian curvature* C_G:

$$C_G = \frac{k}{a^2} \ . \tag{1.15}$$

In three dimensions, the solid angle

$$\mathrm{d}\Omega = \mathrm{d}\theta^2 + \sin^2\theta \, \mathrm{d}\phi^2 \tag{1.16}$$

has to be taken into account and the previous expressions become

$$\mathrm{d}l^2 = a^2 \left[\mathrm{d}r^2 + r^2 \mathrm{d}\Omega^2 \right] \qquad \text{(flat space)}, \tag{1.17}$$

$$\mathrm{d}l^2 = a^2 \left[r^2 \mathrm{d}\Omega^2 + \frac{\mathrm{d}r^2}{1 - r^2} \right] \qquad \text{(hypersphere)}, \tag{1.18}$$

$$\mathrm{d}l^2 = a^2 \left[r^2 \mathrm{d}\Omega^2 + \frac{\mathrm{d}r^2}{1 + r^2} \right] \qquad \text{(constant negative curvature)}. \tag{1.19}$$

By generalizing these equations with the introduction of the k parameter, and considering the Equations (1.16) and (1.6), we find the functional form of the Friedmann-Robertson-Walker metric:

$$\mathrm{d}s^2 = c^2 \mathrm{d}t^2 - a^2(t) \left[\frac{\mathrm{d}r^2}{1 - kr^2} + r^2 (\mathrm{d}\theta^2 + \sin^2\theta \, \mathrm{d}\phi^2) \right]. \tag{1.20}$$

In this framework $a(t)$ is the *cosmic scale factor*, t is the aforementioned proper time and r, θ, ϕ are the *comoving coordinates*, with r dimensionless. As mentioned above, k can be either 0, 1 or -1, and in particular the space is flat ($k = 0$), closed ($k = 1$) or open ($k = -1$) if the *density parameter* $\Omega(t)$, defined as

$$\Omega(t) = \frac{\rho}{\rho_c}, \tag{1.21}$$

is, respectively, equal to, greater or less than unity. The term ρ_c is the *critical density* of the universe, defined as the density for which the universe is flat:

$$\rho_c = \frac{3}{8\pi G} \left(\frac{\dot{a}}{a} \right)^2 . \tag{1.22}$$

Nowadays, at the cosmic time t_0, the value of the critical density $\rho_{0,c}$ is

$$\rho_{0,c} = 1.9 \, 10^{-29} \, h^2 \ \ \mathrm{g \ cm^{-3}}, \tag{1.23}$$

where

$$h = \frac{\dot{a}(t_0)}{100\, a(t_0)} \ . \tag{1.24}$$

Another important quantity in cosmology is the *deceleration parameter* q, defined as

$$q = -\frac{\ddot{a}a}{\dot{a}^2} \ . \tag{1.25}$$

This parameter will be useful for the understanding of the nature of the expansion in different universes.

1.4 Proper and comoving distances

From the FRW metric derive two fundamental quantities: the proper distance and the comoving distance. The *proper distance* d_P of a point P from the origin of a set of polar coordinates (r, θ, ϕ), is defined by imposing $\mathrm{d}t = \mathrm{d}\theta = \mathrm{d}\phi = 0$ in Eq. (1.20). Therefore it is the geodesic passing through the point P and the origin, and has the form

$$d_P = \int_0^r \frac{a(t)\, \mathrm{d}r'}{(1 - kr'^2)^{1/2}} = a(t) f(r), \tag{1.26}$$

where $f(r)$ has a different form for each value of the curvature parameter, namely

$$f(r) = \sin^{-1} r \qquad (k = 1), \tag{1.27}$$

$$f(r) = r \qquad (k = 0), \tag{1.28}$$

$$f(r) = \sinh^{-1} r \qquad (k = -1). \tag{1.29}$$

From the definition of d_P, given for $\mathrm{d}t = 0$, it is clear that this quantity can not be measured, given that it does not account for the limits on the propagation speed of information. However it has a crucial role for the comprehension of the expansion of the universe, as we will see in the next section.
Moreover, at the present time t_0 the proper distance is called *comoving distance*, d_c:

$$d_c = a_0 f(r), \tag{1.30}$$

where $a_0 = a(t_0)$. The proper and comoving distances are therefore related by the equation

$$d_c = \frac{a_0}{a} d_P. \tag{1.31}$$

1.5 The Hubble-Lemaître law

The Hubble-Lemaître Law (Lemaître, 1927; Hubble, 1929) describes the expansion of our universe and descends from the Cosmological Principle, therefore from the FRW metric.

In fact, by considering the definition of proper distance, Eq. (1.26), we obtain the radial velocity of a source at a point P with respect to the origin of a set of polar coordinates (r, θ, ϕ):

$$v_r = \frac{\mathrm{d}d_P}{\mathrm{d}t} = \dot{a} f(r) = \frac{\dot{a}}{a} d_P. \tag{1.32}$$

This relation is the Hubble-Lemaître Law and the quantity

$$H(t) = \frac{\dot{a}}{a} \ , \tag{1.33}$$

is often called the *Hubble parameter*, which is constant at a given proper time. For the present cosmic time we refer to $H(t_0) = H_0$ as the *Hubble constant*, which has the value

$$H_0 = 67.4 \pm 0.5 \text{ km s}^{-1} \text{ Mpc}^{-1}. \tag{1.34}$$

In particular, this is the value obtained by the ESA Planck mission (Planck Collaboration 2018, Paper VI) from the power spectrum of the cosmic microwave radiation (CMB), assuming a ΛCDM model for the universe.[2] There is however a discrepancy between this value of the Hubble constant and those obtained with other independent methods, such as observations of type Ia supernovae (S. Dhawan et al. 2018) or Cepheids in nearby galaxies (Riess et al. 2019). These differences are subject of debate and raised doubts about the ΛCDM model for the universe.

1.6 Cosmological redshift

Due to the expansion of the universe, the light from distant sources shows a shift towards longer wavelengths, namely a redshift. The redshift z is a physical observable and is defined as

$$z = \frac{\lambda_0 - \lambda_e}{\lambda_e} \ . \tag{1.35}$$

The quantity λ_e is the wavelength of radiation in the rest frame of the source, which is at a comoving coordinate r and emits the signal at time t_e. On the other hand, λ_0 is the wavelength observed at time t_0 at a point O (which we consider as the origin of our coordinate system). Light travels along a null geodesic, therefore $\mathrm{d}s^2 = 0$ and for $\mathrm{d}\theta = \mathrm{d}\phi = 0$ the Eq. (1.20) becomes

$$\int_{t_e}^{t_0} \frac{c\,\mathrm{d}t}{a(t)} = \int_0^r \frac{\mathrm{d}r}{\sqrt{1 - kr^2}} = f(r). \tag{1.36}$$

The important property of $f(r)$ is that it does not vary with time, because both the source and the observer are moving with the cosmological expansion and

[2] See Section 1.9 for a description of the ΛCDM model.

therefore r is a constant. Consequently, if we consider the light emitted from the source at $t' = t_e + \delta t_e$ and received by the observer at $t'_0 = t_0 + \delta t_0$, we can write

$$\int_{t'}^{t'_0} \frac{c\,\mathrm{d}t}{a(t)} = f(r). \tag{1.37}$$

If δt_e and δt_0 are small, from Equations (1.36) and (1.37) we derive that

$$\frac{\delta t_0}{a_0} = \frac{\delta t_e}{a}\ , \tag{1.38}$$

where $a = a(t_e)$. By expressing the frequencies of emitted and observed light as $\nu_e = 1/\delta t_e$ and $\nu_0 = 1/\delta t_0$, we obtain

$$\nu_e a = \nu_0 a_0, \tag{1.39}$$

from which

$$1 + z = \frac{a_0}{a}\ . \tag{1.40}$$

In an expanding universe the value of $a(t)$ increases with time, resulting in a redshift of the light emitted by the galaxies in the Hubble flow, i.e. the galaxies that are receding from us due to the expansion of the universe.

1.7 Cosmological distances

The proper distance d_P is defined from the FRW metric imposing $\mathrm{d}t = 0$, which implies that this quantity should be measured in a null time interval. Being this physically impossible, it is necessary to define new measurable distances.
One such distance is the *luminosity distance* d_L, defined as

$$d_L = \left(\frac{L}{4\pi l}\right)^{1/2}, \tag{1.41}$$

where L is the luminosity emitted by the source, which is at a comoving distance r, at time t. The quantity l is the flux measured by the observer at time t_0, expressed as

$$l = \frac{L}{4\pi a_0^2 r^2}\left(\frac{a}{a_0}\right)^2, \tag{1.42}$$

where $4\pi a_0^2 r^2$ is the area of a spherical surface centered on the source and passing through the position of the observer. The factor $(a/a_0)^2$ contains two effects caused by the expansion of the universe: redshift and dilatation of time intervals. Firstly, from Eq. (1.40) we know that the photons have been redshifted by a factor a/a_0. Then, from Eq. (1.38) it turns out that there is a time-dilatation due to the expansion of the universe, which implies that the photons emitted by

the source in a time interval δt arrive to the observer in an interval $\delta t_0 = (a_0/a)\delta t$. From Eq. (1.42), the Eq. (1.41) can be expressed as

$$d_L = a_0^2 \frac{r}{a} = a_0 r(1+z). \tag{1.43}$$

An additional measurable cosmological distance is the *angular-diameter distance* d_A:

$$d_A = \frac{D_P}{\Delta\theta} \ . \tag{1.44}$$

Here D_P is the proper diameter of a source with comoving coordinate r at time t, while $\Delta\theta$ is the angle subtended by D_P. In particular $D_P = ar\Delta\theta$, therefore

$$d_A = ar = \frac{a_0 r}{1+z} \ . \tag{1.45}$$

The luminosity distance d_L and the angular-diameter distance d_A can be exploited in presence of standard candles and standard rulers, respectively. A standard candle is a source with known luminosity, while a standard ruler has a known spatial dimension.
Moreover, d_L and d_A are defined in order to preserve Euclidean properties, respectively the inverse-square law and the variation of angular size with the distance. Additionally, from these quantities we can define the so called *duality relation*, derived from Equations (1.43) and (1.45):

$$\frac{d_L}{d_A} = (1+z)^2. \tag{1.46}$$

Deviations from the factor $(1+z)^2$ quantify the deviations from the FRW metric and in turn from homogeneity and isotropy, however it is quite difficult to find objects that are both standard candles and standard rulers.

1.8 Friedmann models

The Friedmann models are fundamental in the description of the universe as a whole. They are based on the FRW metric and describe the content of matter and energy of the universe as a perfect fluid with, in general, pressure p and density ρ.

1.8.1 Friedmann equations

In a universe described by General Relativity, the geometry of space-time is related to the matter content through the Einstein Equations, Eq. (1.4). From these equations derive the Friedmann equations, which are based on two fundamental assumptions: the FRW metric, and the description of the content of

matter in the universe as a perfect fluid, so that the energy-momentum tensor has the form expressed in Eq. (1.5).
With these assumptions, the Einstein equations yield

$$\ddot{a} = -\frac{4\pi}{3} G \left(\rho + 3\frac{p}{c^2}\right) a \tag{1.47}$$

for the time-time component, and

$$a\ddot{a} + 2\dot{a}^2 + 2kc^2 = 4\pi G \left(\rho - \frac{p}{c^2}\right) a^2 \tag{1.48}$$

for the space-space components ($i,\, j = 1,\, i,\, j = 2,\, i,\, j = 3$). The space-time components, given the assumption of the Cosmological Principle, give $0 = 0$. From the combination these two equations we obtain

$$\dot{a}^2 + kc^2 = \frac{8}{3}\pi G \rho a^2. \tag{1.49}$$

Equations (1.47) and (1.49) - the Friedmann equations (Friedmann, 1922) - are not independent under the assumption of an adiabatic expansion of the universe. The second, indeed, can be derived from the first through the adiabaticity relation

$$\mathrm{d}(\rho\, c^2 a^3) = -p\, \mathrm{d}a^3. \tag{1.50}$$

1.8.2 The cosmological constant

Friedmann obtained his equations in 1922 and at that time was generally accepted the idea of a static, not evolving universe. However from Eq. (1.47) it turns out that the universe can not be static, unless either the pressure p or the energy density ρc^2 are negative. This is not possible, merely for the physical definition of p and ρc^2.
In order to describe a static universe, Einstein yet in 1917 introduced a cosmological constant Λ that modified the gravitation itself:

$$R_{\alpha\beta} - \frac{1}{2} g_{\alpha\beta} R - \Lambda g_{\alpha\beta} = \frac{8\pi G}{c^4} T_{\alpha\beta}. \tag{1.51}$$

With an appropriate choice of Λ, which must be sufficiently small to not change the laws of planetary motions, one can obtain a static cosmological model.
Nowadays we know that the universe is an expanding object, therefore the cosmological constant should not be necessary. However, from observations of the flux of distant type Ia supernovae, we know that the universe is expanding in an accelerated way (Riess et al. 1998), while Eq. (1.47) predicts a decelerated expansion. Therefore Λ is still considered in the generally accepted cosmological model, but its place in the Einstein filed equations is different. It indeed is set in the energy-momentum tensor, modifying the content of energy and matter of

the universe, intended as the energy density of an unknown *dark energy*. We can then define the modified energy-momentum tensor $\tilde{T}_{\alpha\beta}$ as

$$\tilde{T}_{\alpha\beta} = T_{\alpha\beta} + \frac{\Lambda c^4}{8\pi G} g_{\alpha\beta} = -\tilde{p} g_{\alpha\beta} + (\tilde{p} + \tilde{\rho} c^2) u_\alpha u_\beta, \tag{1.52}$$

where $\tilde{p}$ and $\tilde{\rho}$ are the effective pressure and the effective density, respectively, and they are related to the corresponding quantities for a perfect fluid by

$$\tilde{p} = p - \frac{\Lambda c^4}{8\pi G}, \quad \tilde{\rho} = \rho + \frac{\Lambda c^2}{8\pi G} \ . \tag{1.53}$$

The Einstein field equations can be therefore expressed as

$$R_{\alpha\beta} - \frac{1}{2} g_{\alpha\beta} R = \frac{8\pi G}{c^4} \tilde{T}_{\alpha\beta}, \tag{1.54}$$

and the Friedmann equations become

$$\ddot{a} = -\frac{4\pi}{3} G \left(\tilde{\rho} + 3\frac{\tilde{p}}{c^2} \right) a, \tag{1.55}$$

$$\dot{a}^2 + kc^2 = \frac{8}{3} \pi G \tilde{\rho} a^2. \tag{1.56}$$

1.8.3 The general Friedmann model

The Friedmann equations, along with the adiabaticity relation expressed in Eq. (1.50), describe a perfect fluid and allow to calculate the time evolution of $a(t)$, as well as $\rho(t)$ and $p(t)$, if the equation of state is known.
The general Friedmann model accounts for the Cosmological Principle, therefore the pressure can only be isotropic. Moreover, the isotropic pressure is a necessary condition for a perfect fluid. In particular perfect fluids, at rest, are completely described in terms of their energy density ρc^2 and pressure p, from which we can define the equation of state of the fluid in the form

$$p = w \rho c^2, \tag{1.57}$$

where the parameter w is assumed to be constant with time, and is defined in the range

$$0 \leq w < 1, \tag{1.58}$$

called *Zel'dovich interval*. This range descends from the definition of the sound speed v_s in a medium,

$$v_s^2 = \left. \frac{\partial p}{\partial \rho} \right|_{S=const} \tag{1.59}$$

where S is the entropy. From the given definition of the equation of state, it turns out that for $w > 1$ the sound speed would exceed the speed of light. On the other hand, for $w < 0$ the sound speed would not be a real variable.
In particular w can assume the value $w = 0$ for pressureless matter, or *dust*. A fluid of dust is described by $p = 0$ because it represents a good approximation to the behavior of a non-relativistic gas. Indeed the energy at rest of a particle, $m_p c^2$, is typically larger than its kinetic energy, therefore the exerted pressure is negligible. On the other hand, we have $w = 1/3$ for a non-degenerate *radiative fluid*, which can be composed of photons or ultrarelativistic particles in thermal equilibrium.
From the adiabaticity relation, Eq. (1.50), and the general equation of state, Eq. (1.57), it is straightforward to obtain

$$\rho_w = \rho_{0,w} \left(\frac{a}{a_0} \right)^{-3(1+w)}, \tag{1.60}$$

which for the case of a matter (or dust) universe, $w = 0$, becomes

$$\rho_m = \rho_{0,m} \left(\frac{a}{a_0} \right)^{-3} = \rho_{0,m} \, (1+z)^3, \tag{1.61}$$

while for a radiative universe we have

$$\rho_r = \rho_{0,r} \left(\frac{a}{a_0} \right)^{-4} = \rho_{0,r} \, (1+z)^4. \tag{1.62}$$

The densities of matter and radiation change in different ways with time, or with redshift, and the reason is simple. Let us consider a comoving box that expands with the universe and contains particles which can not be created nor destroyed. If these are particles of dust, their density decreases as the cube of the scale factor, as expressed in Eq. (1.61). However, if the particles are relativistic they behave like photons, therefore additionally to the decrease in density caused by the expansion of the box they undergo an increase in wavelength by a factor a, as described in Eq. (1.62).
In addition to the cases of matter and radiation universes, we can deal with a peculiar case given by $w = -1$. This derives from the Equations (1.53), in which are defined the pressure and the density associated to the cosmological constant:

$$p_\Lambda = -\frac{\Lambda c^4}{8\pi G}, \qquad \rho_\Lambda = \frac{\Lambda c^2}{8\pi G} \, . \tag{1.63}$$

A peculiarity manifest itself by considering the Eq. (1.60) for $w = -1$, indeed it turns out that the dark energy density does not vary as the universe expands.

Let us focus now on the evolution of the scale parameter $a(t)$. We can consider the Eq. (1.49) at the present time t_0, and dividing by a_0^2 we obtain

$$H_0(1-\Omega_{0,w}) = -\frac{kc^2}{a_0^2} \ , \tag{1.64}$$

where $\Omega_{0,w}$ is the density parameter at the present time for a fluid component:

$$\Omega_{0,w} = \frac{\rho_{0,w}}{\rho_{0,cr}} \ . \tag{1.65}$$

Combining this result with the Eq. (1.49) considered at a generic time t and divided by a_0^2, we have

$$\frac{\dot{a}^2}{a_0^2} = H_0^2 \left[1 - \Omega_{0,w} + \Omega_{0,w} \left(\frac{a_0}{a}\right)^{1+3w}\right] . \tag{1.66}$$

This is the most frequent form of the Friedmann equation. We can also express it in terms of the evolution of the Hubble parameter,

$$H^2(t) = H_0^2 \left(\frac{a_0}{a}\right)^2 \left[1 - \Omega_{0,w} + \Omega_{0,w} \left(\frac{a_0}{a}\right)^{1+3w}\right] , \tag{1.67}$$

and for a universe with more than one fluid component this expression becomes

$$H^2(t) = H_0^2 \left(\frac{a_0}{a}\right)^2 \left[1 - \sum_i \Omega_{0,w_i} + \sum_i \Omega_{0,w_i} \left(\frac{a_0}{a}\right)^{1+3w_i}\right] . \tag{1.68}$$

1.8.4 Flat models

Let us consider a universe with a single component and with a flat geometry, i.e. $\Omega_w = 1$. This kind of models are called *Einstein-de Sitter* (EdS) universes. Then the Eq. (1.66) becomes

$$\frac{\dot{a}^2}{a_0^2} = H_0^2 \left(\frac{a_0}{a}\right)^{1+3w} , \tag{1.69}$$

which can be integrated, obtaining

$$a(t) = a_0 \left(\frac{t}{t_0}\right)^{2/3\,(1+w)} . \tag{1.70}$$

Therefore the expansion in these universes, for $w = 0$ or $w = 1/3$, is eternal. Moreover from the last equation we can obtain the relation between time and redshift:

$$t = t_0 (1+z)^{-3(1+w)/2} . \tag{1.71}$$

From Equations (1.70), (1.71) and (1.60), derive the following relations:

$$H \equiv \frac{\dot{a}}{a} = \frac{2}{3(1+w)t} = H_0 \frac{t_0}{t} = H_0(1+z)^{3(1+w)/2}, \tag{1.72}$$

$$q \equiv -\frac{a\ddot{a}}{\dot{a}^2} = \frac{1+3w}{2} = \text{const} = q_0, \tag{1.73}$$

$$t_{0,w} \equiv t_0 = \frac{2}{3(1+w)H_0}, \tag{1.74}$$

$$\rho = \rho_{0,w}\left(\frac{t}{t_0}\right)^{-2} = \frac{1}{6(1+w)^2\pi G t^2}\ . \tag{1.75}$$

Then in these models the age of the universe t_0 is closely related to the Hubble constant H_0. Moreover the deceleration parameter q is constant, therefore the expansion is steadily braked with time for positive values of w. It turns out that for high values of w and, therefore, for higher values of pressure, also the deceleration parameter increases. On the other hand, negative values of w cause a steadily accelerated expansion. In Table 1.1 are shown the cases for a matter-dominated universe ($w = 0$) and a radiation-dominated universe ($w = 1/3$).

Matter ($w = 0$)	Radiation ($w = 1/3$)
$a(t) = a_0\left(\frac{t}{t_0}\right)^{2/3}$	$a(t) = a_0\left(\frac{t}{t_0}\right)^{1/2}$
$t = t_0(1+z)^{-3/2}$	$t = t_0(1+z)^{-2}$
$H = \frac{2}{3t} = H_0(1+z)^{3/2}$	$H = \frac{2}{3t} = H_0(1+z)^2$
$q_0 = \frac{1}{2}$	$q_0 = 1$
$t_0 = \frac{2}{3H_0}$	$t_0 = \frac{1}{2H_0}$
$\rho_m = \frac{1}{6\pi G t^2}$	$\rho_m = \frac{3}{32\pi G t^2}$

Table 1.1: Expressions of the fundamental parameters in matter-dominated and radiation-dominated flat universes.

1.8.5 Curved models

In case of the density parameter with values $\Omega_w \neq 1$, we are in the case of curved universes. At early times, that now we consider by setting $\dot{a} = 0$ in Eq. (1.66),

we can neglect the term $(1-\Omega_{0,w})$ because

$$\frac{a_0}{a} = 1 + z \gg |\Omega_{0,w}^{-1} - 1|^{1/(1+3w)} \equiv \frac{a_0}{a(t^*)} = 1 + z^*. \tag{1.76}$$

Consequently, for $0 < a \leq a(t^*) = a^*$ the Eq. (1.66) has the form

$$\frac{\dot{a}^2}{a_0^2} \simeq H_0^2 \Omega_{0,w} \left(\frac{a_0}{a}\right)^{1+3w}, \tag{1.77}$$

which, for $\Omega_{0,w} = 1$, is the same expression derived for the flat models. This result is extremely relevant, because allows us to generalize the behavior of any sort of universe at times close to the Big Bang as equivalent to the flat case.

More in detail, for *open universes* ($\Omega_w < 1$) in Eq. (1.66) is evident that $\dot{a}$ can not be zero, it is always positive and therefore a grows indefinitely, as in the case of the flat universes.
For $a \gg a^*$ from Eq. (1.66) we obtain

$$\dot{a} = a_0 H_0 (1 - \Omega_{0,w})^{1/2}, \tag{1.78}$$

therefore $\dot{a}$ tends to a constant for $t \gg t^*$, then $a \propto t$ asymptotically. Consequently can be derived the following relations:

$$H \simeq t^{-1}, \tag{1.79}$$

$$q \simeq 0. \tag{1.80}$$

On the other hand, for *closed universes* ($\Omega_w > 1$) the first derivative of a can be zero in Eq. (1.66), at a time t_{max}. In this case $a(t_{max}) = a_{max}$ is equal to

$$a_{max} = a_0 \left(\frac{\Omega_{0,w}}{\Omega_{0,w} - 1}\right)^{1/(1+3w)}. \tag{1.81}$$

For $t > t_{max}$ the deceleration parameter decreases at the same rate of its increment, therefore at a time $t_f = 2t_{max}$ the universe collapses in another singularity, the Big Crunch.
In Fig. 1.1 is shown the time evolution of $a(t)$ for each model of universe.
Having the general behaviors of the curved models, we can consider the effects of the different fluids that can compose them.

Let us consider first the *dust models*, i.e. with $w = 0$, for which the Eq. (1.66) becomes

$$\frac{\dot{a}^2}{a^2} = H_0^2 \left(1 - \Omega_{0,m} + \Omega_{0,m} \frac{a_0}{a}\right). \tag{1.82}$$

For open models this equation has a solution in the parametric form:

$$a(\psi) = a_0 \frac{\Omega_{0,m}}{2(1 - \Omega_{0,m})} (\cosh \psi - 1), \tag{1.83}$$

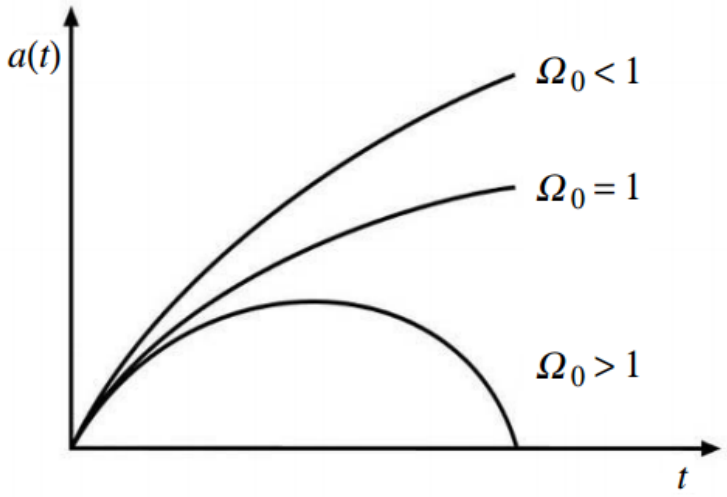

Figure 1.1: Time evolution of the expansion parameter $a(t)$ in a closed model ($\Omega_0 > 1$), flat model ($\Omega_0 = 1$) and closed model ($\Omega_0 < 1$). Image from P. Coles, F. Lucchin, [1] p. 40.

$$t(\psi) = \frac{1}{2H_0} \frac{\Omega_{0,m}}{(1-\Omega_{0,m})^{3/2}} (\sinh\psi - \psi). \tag{1.84}$$

From these last relations it is possible to derive that

$$t_0 > \frac{2}{3H_0} \ , \tag{1.85}$$

where $2/(3H_0)$ is the age of the universe predicted in a flat model with $w = 0$. For closed models, instead, the parametric solutions for Eq. (1.66) are

$$a(\theta) = a_0 \frac{\Omega_{0,m}}{2(1-\Omega_{0,m})} (1 - \cos\theta), \tag{1.86}$$

$$t(\theta) = \frac{1}{2H_0} \frac{\Omega_{0,m}}{(1-\Omega_{0,m})^{3/2}} (\theta - \sin\theta), \tag{1.87}$$

and from these relations is derived t_0:

$$t_0 < \frac{2}{3H_0} \ . \tag{1.88}$$

Turning to the *radiative models*, for which $w = 1/3$, Eq. (1.66) has the form

$$\frac{\dot{a}^2}{a^2} = H_0^2 \left[1 - \Omega_{0,r} + \Omega_{0,r} \left(\frac{a_0}{a} \right)^2 \right], \tag{1.89}$$

and the solution is

$$a(t) = a_0 (2H_0 \Omega_{0,r}^{1/2} t)^{1/2} \left(1 + \frac{1-\Omega_{0,r}}{2\Omega_{0,r}^{1/2}} H_0 t \right)^{1/2} . \tag{1.90}$$

In open models, for $t \gg t^*$ this last equation becomes

$$a(t) \simeq a_0(1-\Omega_{0,r})^{1/2} H_0 t, \tag{1.91}$$

and it is possible to show that for the present cosmic time t_0 holds the relation

$$t_0 > \frac{1}{2H_0} \ , \tag{1.92}$$

where $1/(2H_0)$ is the value of t_0 in a flat universe.
For closed models, instead,

$$t_0 < \frac{1}{2H_0}. \tag{1.93}$$

1.8.6 Evolution of the density parameter

The density parameter depends on time, or redshift, and in the case of a single dominant fluid component it can be written as

$$\Omega_w(z) = \frac{\rho_w(z)}{3H^2(z)/(8\pi G)} \ . \tag{1.94}$$

Considering the Eq. (1.60) for $\rho_w(z)$ and Eq. (1.67) for $H(z)$, we obtain the expression

$$\Omega_w(z) = \frac{\Omega_{0,w}(1+z)^{1+3w}}{(1-\Omega_{0,w}) + \Omega_{0,w}(1+z)^{1+3w}}, \tag{1.95}$$

which can be written in a more intuitive form:

$$\Omega_w^{-1}(z) - 1 = \frac{\Omega_{0,w}^{-1} - 1}{(1+z)^{1+3w}} \ . \tag{1.96}$$

This is a fundamental relation, indeed from this it turns out that all universes remain always with the same geometry, i.e. the density parameter can not change its sign and the flat universes preserve their flatness. The comprehension of this result is straightforward: the expansion can not change the sign of the curvature parameter k. Moreover, this relation shows a result previously obtained, for which at early times in the history of the universe all the kinds of universe behave like the Einstein-de Sitter (EdS) model.

1.8.7 Cosmological horizons

Given the time evolution of the expansion parameter $a(t)$, it is possible to know the extension of the proper distance $R_H(t)$, defined as

$$R_H(t) = a(t) \int_0^t \frac{c\,\mathrm{d}t'}{a(t')} \ . \tag{1.97}$$

This quantity defines a sphere centered on a particle, or an observer, containing all the points in causal connection with that particle. Moreover, the definition of $R(t)$ accounts for the expansion of the universe, indeed the generic distance $c\,\mathrm{d}t'$ covered by a photon in the interval $[t',\, t'+\mathrm{d}t']$ has to be multiplied by a factor $a(t)/a(t')$, in order to obtain a proper distance.[3] In Eq. (1.97) the integral could diverge for times close to the Big Bang, for which $a(t)$ tends to zero. In this case every particle can, potentially, have received a signal from the whole universe. However if the integral is not divergent for this lower limit, then $R_H(t)$ defines the so called *particle horizon*.
In general for a Friedmann universe $a(t) \propto t^\beta$, with $\beta > 0$, therefore

$$R_H(t) \propto t^\beta \int_0^t t^{-\beta}\mathrm{d}t. \tag{1.98}$$

Then R_H exists only if $\beta < 1$. Moreover, considering the Eq. (1.47) we have

$$\ddot{a} = -\frac{4\pi}{3}Ga\left(\rho + \frac{3p}{c^2}\right) \propto \beta(\beta-1)t^{\beta-2}, \tag{1.99}$$

from which

$$\beta(\beta-1) \propto -\frac{4\pi}{3}Gt^2\left(\rho + \frac{3p}{c^2}\right). \tag{1.100}$$

Therefore, given that the existence condition of the Big Bang is $\ddot{a} < 0$, it is necessary that $\beta(\beta-1) < 0$, i.e. $0 < \beta < 1$. This means that the Big Bang implies the finiteness of $R_H(t)$.
Lastly, for a flat Friedmann model it can be shown that

$$R_H(t) \simeq 3\frac{1+w}{1+3w}ct, \tag{1.101}$$

and for the cases of dust and radiation flat universes we have $R_H = 3ct$ and $R_H = 2ct$, respectively.

Another typology of horizon is the *Hubble sphere*, defined by the radius R_c,

$$R_c = \frac{c}{H}\ , \tag{1.102}$$

that represents the proper distance travelled by light in the characteristic expansion time $\tau_H = 1/H$. In an Einstein-de Sitter model we have $R_c = 3(1+w)ct/2$, therefore it is of the same order of magnitude of the particle horizon:

$$R_c = \frac{1+3w}{2}R_H. \tag{1.103}$$

[3] In Eq. (1.37) is expressed the value of the function $f(r)$ for a photon, that combined with the definition of proper distance gives the relation for $R_H(t)$.

However, the Hubble sphere and the particle horizon are two completely different entities: the former is defined instantaneously at a time t, while the latter accounts for the past history of the considered particle up to time t. It is possible that objects inside the particle horizon are outside the Hubble sphere. Being outside the Hubble sphere means that the recession velocity is greater than the speed of light, indeed Eq. (1.102) is an expression of the Hubble-Lemaître Law. Objects can be outside R_c at a given time, within it at a later time, and outside again. On the other hand, an object can not go outside the particle horizon once it is inside it.

1.9 The Standard Cosmological Model

The basic idea for the description of the observed universe lies in the *hot Big Bang model*, based on the Cosmological Principle and the Friedmann equations. In this framework the evolution is described as a thermal history, and this is the reason of the term "hot": going back to times close to the Big Bang, the universe becomes increasingly hotter. In particular the temperature of the universe at the present time is $T = 2.726 \pm 0.005\,\mathrm{K}$. This is the temperature of the cosmic microwave background (CMB), the black-body radiation that started to freely propagate when the first recombination of the free electrons occurred. Moreover, CMB is one of the strongest evidences of the Big Bang.
Based on the hot Big Bang, the standard cosmological model is the ΛCDM, where Λ represents the dark energy contribution in terms of the cosmological constant while CDM stands for *cold dark matter*, a dust component of dark matter. Other than CDM, there is a smaller contribution to the matter content given by baryonic matter, estimated for example through the mass-luminosty ratio of the observable structures in the universe or from primordial nucleosynthesis studies (see the review by Thuan & Izotov, 2000). The mass-luminosity ratio can be obtained through dynamical studies of galaxies, galaxy groups and clusters, and it is also a fundamental evidence of dark matter.

The reason for which cold dark matter is considered in the modern standard model is that it becomes non-relativistic earlier, with respect to hot dark matter. Given that the universe is described in terms of a thermal history, cosmic time is always related to a temperature. Therefore the time for which a fluid becomes non-relativistic can be estimated from the relation $k_B T \simeq m_x c^2$, where k_B is the Boltzmann constant and m_x is the characteristic mass of the fluid. Cold dark matter is more massive than hot dark matter, then it becomes non-relativistic first. Moreover CDM has another particular advantage with respect to the hot counterpart, indeed it is non-relativistic at the moment of the decoupling from the radiation component.[4] This allows an immediate formation of CDM grav-

[4]The decoupling of the dark matter takes place before the decoupling of baryons, and it

itational perturbations, which is a phenomenon at the basis of the concordance *hierarchical model* for the formation of the cosmic structure. The latter consists in the formation of small structures first in the universe, that undergo mergers that lead to larger gravitationally-bound objects.

The other fundamental aspect of our cosmological model is the presence of Λ as a dark energy. This is necessary because CMB observations showed that the universe has a flat geometry, that is $\Omega_{tot} = 1$. However dynamical studies of galaxies and galaxy aggregations provide density parameters for the matter $\Omega_m \simeq 0.30$, therefore the dark energy must fill, in terms of Ω_Λ, the gap $1 - \Omega_m \simeq 70$.[5]
Another evidence of dark energy is the accelerated expansion of the universe (Riess et al. 1998), indeed from the first Friedmann equation, Eq. (1.47), we should expect a decelerated expansion in a universe without any sort of dark energy. Focusing on the first Friedmann equation and recalling the general equation of state of the perfect fluid, Eq. (1.57), we see that

$$\ddot{a} = -\frac{4\pi}{3} G a (\rho + \frac{3p}{c^2}) = -\frac{4\pi}{3} G a \rho (1 + 3w). \tag{1.104}$$

Density ρ and pressure p are classically positive, therefore all the homogeneous and isotropic universes with $-1/3 < w < 1$ present the Big Bang singularity,[6] because the scale parameter $a(t)$ has negative concavity and therefore it intersects the time axis. The Big Bang could be avoided in universes that do not follow the Cosmological Principle, or that are not described by means of a perfect fluid. Another possibility is $w < -1/3$, and the cosmological constant Λ is an ideal candidate for this case, having $w = -1$. However the energy density associated to Λ is too low,

$$\rho_{0,\Lambda} = \rho_\Lambda = \text{const} = 10^{-29} \text{ g cm}^{-3}, \tag{1.105}$$

and is dominant only since $z \simeq 0.67$, therefore it is not sufficient to elude the Big Bang. Nowadays we associate the cosmological constant to the energy density of vacuum, and in this idea it is responsible of the inflationary era, i.e. an epoch where the scale factor $a(t)$ grew exponentially with time. In this period of the history of the universe arose the gravitational perturbations, which led to the formation of the structures in the cosmos.

After the introduction of a theoretical background, it is necessary to parametrize the ΛCDM model. It is indeed described by six fundamental parameters:

- Ω_m: total matter density parameter;

is the latter that leads to the free propagation of the cosmic microwave background in the universe.

[5] The density parameter of radiation, at $z \simeq 0$, is completely negligible.

[6] The upper limit for w is set by the Zel'dovich interval, Eq. (1.58).

- Ω_b: baryonic matter density parameter;
- A: normalization of the power spectrum;
- H_0: Hubble constant;
- n: spectral index of the primordial power spectrum;
- τ: reionization optical depth.

The power spectrum and its features will be described in Section 1.11. The parameter τ can be relevant only in CMB observations. Lastly, we stress that in the ΛCDM model the dark energy equation of state parameter is $w = -1$.

1.10 Linear perturbations

In the standard model of the large scale structure formation, the existence of the observed gravitationally bound systems is ascribed to the growth of small perturbations. The origin of such perturbations is attributed to the presence of quantum fluctuations in the early universe, whose growth has been possible thanks to the extremely accelerated expansion of the universe during the inflationary era. The observable smaller form of these resulting perturbations can be seen in the temperature fluctuations of the CMB.[7]
The study of the growth rate of the perturbations, the so called *growth factor*, covers a fundamental role in the estimate of the expansion rate of the universe. The more the expansion is intense, indeed, the more the gravitational collapse will be hindered; therefore, by induction, it is possible to infer the cosmic expansion rate. Operationally, many observations at different redshifts provide the Hubble parameter $H(z)$, that parametrizes the expansion rate.
The density perturbations observed in the cosmic microwave background, at redshift $z \simeq 1100$, are very small, corresponding to a density contrast δ

$$\delta = \frac{\rho - \bar{\rho}}{\bar{\rho}} = \frac{\delta\rho}{\rho} \simeq 10^{-5}, \tag{1.106}$$

where $\bar{\rho}$ represents the mean density of the universe. In the recent universe the density contrast has reached values of 100 or even 1000, and this is a problem in an Einstein-de Sitter scenario, because this kind of model of universe does not predict such a high growth of the perturbations. We will see in the following discussion that this problem can be solved with the so called baryon catch-up.

[7] The cosmic microwave background is a black-body, therefore the energy of the photons can be related to a temperature. Moreover, it is possible to show that fluctuations of this temperature correspond to matter density fluctuations.

The mathematical linear regime of the fluid equations is a good approximation for the description of the great part of the structure evolution and growth. Therefore we will pay attention to this regime of perturbations first, for which we also have analytic solutions, and subsequently will be treated also the non-linear regime and the methods used to describe it.

1.10.1 The Jeans theory

The Jeans theory describes the collapse in a homogeneous and isotropic fluid. The general idea, indeed, is that density perturbations that exceed a critical scale in this fluid could trigger a gravitational collapse, which would result in a growth of these perturbations. The denser these fluctuations become the more they will accrete, resulting in an instability which can cause the formation of a self-gravitating structure.
Gravitational collapse, however, is not that trivial but involves several hydrodynamical and dynamical effects, such as gas heating and the increase of the angular momentum, resulting in an inhibition of the collapse. These effects can not be described in a linear regime and mainly affect the formation of galaxies, or in general the baryonic matter. On larger scales the dominant matter contribution is given by dark matter, which is weakly interactive therefore does not undergo the physical processes of a gas, and in addition the interaction on large scales is driven by gravitation only. Large scales and dark matter, therefore, are two ingredients for a linear regime, and this is the main framework we will focus on in the following analytic discussion.
Before the description of the evolution of perturbations in the universe, it is useful to shed light on the significance of the gravitational collapse in the Jeans theory. Consider a spherical inhomogeneity of radius R, in a background fluid of mean density $\bar{\rho}$, with mass M and a positive density fluctuation $\delta\rho$:

$$\delta\rho = \rho - \bar{\rho} > 0. \tag{1.107}$$

In order to have a collapse, the gravitational potential energy E_p must exceed, in absolute value, the thermal kinetic energy E_k. We define

$$E_k = \frac{1}{2}Mv^2, \quad \text{and} \tag{1.108}$$

$$E_p = -\frac{GM^2}{R} = -\frac{GM}{R}\rho R^3, \tag{1.109}$$

where v is the mean velocity derived from the Maxwell-Boltzmann distribution. The condition for the collapse, $|E_p| > E_k$, then can be expressed as

$$G\rho R^2 > \frac{v^2}{2}. \tag{1.110}$$

From this expression we can rewrite the collapse condition by means of the *Jeans scale* R_J:

$$R > R_J = v\frac{1}{\sqrt{2G\rho}}. \tag{1.111}$$

Having the principles of the gravitational collapse in mind, now we can proceed with a more detailed discussion of the perturbation evolution.

1.10.2 Jeans instability in a static universe

Originally, Jeans studied the gravitational instability of a cloud of gas, for which the local auto-gravitation makes the effects of the expansion of the universe negligible. For a collisional, self-gravitating, perfect fluid in a static universe we can write the equations of motion, in the Newtonian approximation:

$$\frac{\partial \rho}{\partial t} + \nabla \cdot \rho \boldsymbol{v} = 0 \qquad \text{(continuity equation)} \tag{1.112}$$

$$\frac{\partial \boldsymbol{v}}{\partial t} + (\boldsymbol{v} \cdot \nabla)\boldsymbol{v} = -\frac{1}{\rho}\nabla\rho - \nabla\phi \qquad \text{(Euler equation)} \tag{1.113}$$

$$\nabla^2\phi = 4\pi G\rho \qquad \text{(Poisson equation)} \tag{1.114}$$

$$p = p(S, \rho) \qquad \text{(equation of state)} \tag{1.115}$$

$$\frac{\mathrm{d}S}{\mathrm{d}t} = 0 \qquad \text{(entropy conservation)} \tag{1.116}$$

where ϕ is the gravitational potential, and $\boldsymbol{v}$ the flow velocity. From observations of the cosmic microwave background it turned out that the primordial fluctuations can be described as adiabatic perturbations (Planck Collaboration 2018, Paper VI), therefore we can consider the conservation of entropy S. This means that the pressure p depends only on the density ρ, i.e. $p = p(\rho)$. We then have four variables: ρ, $\boldsymbol{v}$, ϕ, p.

This system of equations admits the static solution with $\rho = \rho_0 = const$, $\boldsymbol{v} = \boldsymbol{0}$, $\phi = \phi_0 = const$, $p = p_0 = const$. It has to be noted that this static solution descends from the Cosmological Principle, but it is evident that a homogeneous and isotropic fluid can not be static. Indeed, looking at the Poisson equation, if $\rho_0 \neq 0$ then the gravitational potential must vary. Therefore the incompatibility of a homogeneous and isotropic universe with the staticity condition is evident not only in a relativistic framework, but also in the Newtonian theory. However we will continue our discussion based on this model, because it leads to relevant and valid results.

We can perturb the static solution for a small perturbation, so that $\delta\rho$, $\delta\boldsymbol{v}$, δp,

$\delta\phi$ are $\ll 1$ and therefore the linear regime is valid:

$$\rho = \rho_0 + \delta\rho, \tag{1.117}$$
$$\boldsymbol{v} = \delta\boldsymbol{v}, \tag{1.118}$$
$$p = p_0 + \delta p, \tag{1.119}$$
$$\phi = \phi_0 + \delta\phi. \tag{1.120}$$

Given that the pressure p can be expressed in terms of the density ρ, we can consider three variables, ρ, $\boldsymbol{v}$ and ϕ, and three equations: the continuity, Euler and Poisson equations. We can then substitute the perturbed solutions in these three equations, obtaining new equations for which we look for solutions in the form of Fourier modes $f(r,t)$:

$$f(r,t) = f_k \exp(i\boldsymbol{k}\cdot\boldsymbol{r} + i\omega t). \tag{1.121}$$

Here $\boldsymbol{r}$ is a position vector, $\boldsymbol{k}$ is a wavevector, ω is the wave pulsation. The general expression $f(r,t)$ stands for $\delta\rho$, $\delta\boldsymbol{v}$, $\delta\phi$, and f_k is the amplitude. In these terms it is possible to obtain the *dispersion relation* from the system defined by the continuity, Euler and Poisson equations. In particular we set equal to zero the determinant of the representative matrix of this linear system of equations, from which the dispersion relation is:

$$\omega^2 = c_s^2 k^2 - 4\pi G\rho_0, \tag{1.122}$$

where $c_s \simeq (\delta p/\delta\rho)$ is the sound speed for adiabatic perturbations. The Eq. (1.122) admits two types of solutions, according to the value of the wavelength $\lambda = 2\pi/k$ (where k is a wavenumber) with respect to the *Jeans length* λ_J:

$$\lambda_J = \frac{2\pi}{k_J} = c_s\sqrt{\frac{\pi}{G\rho_0}}. \tag{1.123}$$

Indeed Eq. (1.122) can be written as

$$\omega = \pm\, kc_s\left[1 - \left(\frac{\lambda}{\lambda_J}\right)^2\right]^{1/2}, \tag{1.124}$$

then, for $\lambda < \lambda_J$ the perturbation propagates as a sound wave with constant amplitude, and for $\lambda \to 0$ the wave propagates at the sound speed, otherwise if $\lambda \to \lambda_J$ the wave becomes static. On the other hand, if $\lambda > \lambda_J$ the pulsation ω is imaginary and this implies a non-propagating, stationary solution. Defining the density contrast $\delta(\boldsymbol{x},t)$ as

$$\delta(\boldsymbol{x},t) = \frac{\delta\rho(\boldsymbol{x},t)}{\rho_0}, \tag{1.125}$$

we find, for the case $\lambda > \lambda_J$, an exponential form for the solution:

$$\delta = \delta_k \exp(i\boldsymbol{k} \cdot \boldsymbol{r}) \exp(\pm |\omega| t). \tag{1.126}$$

Of the two solutions given in this equation, we are interested to the increasing one, representing the growth of a perturbation due to gravitational collapse. It is important to note that the exponential growth holds for sufficiently large scales, i.e. for $\lambda \gg \lambda_J$, for which gravity dominates.
To summarize, perturbations described by Fourier modes with $\lambda < \lambda_J$ propagate as sound waves. Only in the case $\lambda \gg \lambda_J$ it is possible to have a growth of the perturbation, that in the static scenario is exponential. We can already understand that this growth will be lower in an expanding universe, where the expansion hinders the collapse.

1.10.3 Instabilities in an expanding universe

Let us now consider the effect of the expansion of the universe on the growth of the perturbations.
Consider first perturbations on scales larger than the particle horizon R_H. In this case the dominant interaction is gravity, therefore we can describe this physical situation in terms of General Relativity. In particular we consider a perturbation described as a closed universe, embedded in a EdS, homogeneous and isotropic background universe. We label with b the properties of this background universe and with p those of the perturbation, so we have

$$H_p^2 + \frac{c^2}{a^2} = \frac{8\pi}{3} G \rho_p, \tag{1.127}$$

$$H_b^2 = \frac{8\pi}{3} G \rho_b, \tag{1.128}$$

and for simplicity we set $H_p = H_b$. Gravity couples the behaviors of the different fluid components in the universe, in particular the minor components follow the time dependency of the density contrast of the dominant one. Before the *equivalence* between the radiation and matter densities, i.e. for $t < t_{eq}$, the dominant contribution is given by radiation, and it turns out that the radiation density contrast δ_r has the following dependency on time,

$$\delta_r \propto t, \tag{1.129}$$

so that also the matter density contrast is directly proportional to t. On the other hand, after the equivalence the matter is dominant, implying

$$\delta_m \propto t^{2/3}. \tag{1.130}$$

and therefore also $\delta_r \propto t^{2/3}$.[8] These dependencies are still valid for scales $< R_H$, but with the condition that they are much greater than the Jeans scale. In this case, however, the minor components do not follow the dependencies of the dominant one. The general result, in brief, is that perturbations larger than the particle horizons always grow with time.
On the other hand, for perturbations on scales inside the particle horizon it is necessary to invoke the dynamics of self-gravitating fluids. As described in Section 1.10.2, we look for perturbed adiabatic solutions. We focus first on the case of matter-dominated universes, meaning that we consider times $t > t_{eq}$. Differently from the situation described in Section 1.10.2, now the flow velocity u is not null but it is given by the expansion of the universe:

$$u = \frac{\mathrm{d}r}{t} = \dot{a}x + a\dot{x} = Hr + a\dot{x} = Hr + v_p, \tag{1.131}$$

where r is the proper coordinate, while x is the comoving component. The first term in the left hand side of Eq. (1.131) represents the *Hubble flow*, i.e. the expansion of the universe, while the second term is a *peculiar velocity* given by the perturbation. The functional form of the solutions $f(x,t)$ is still a Fourier mode, but now the amplitude f_k depends on time because of the expansion of the universe:

$$f(x,t) = f_k(t)\exp(i\boldsymbol{k}\cdot\boldsymbol{x}). \tag{1.132}$$

Considering again the same three variables, and substituting the relative solutions in the continuity, Euler and Poisson equations, the dispersion relation can be expressed as

$$\ddot{\delta_k} + 2H\dot{\delta_k} + \delta_k[k^2c_s^2 - 4\pi G\rho_0] = 0. \tag{1.133}$$

Here δ_k is the amplitude of the wave that represents the Fourier transform of the density contrast field. The second term of this relation is a tidal contribution deriving from the expansion of the universe, and it acts against gravity. The second term in the square brackets represents the mean gravity, while the term $\delta_k k^2 c_s^2$ accounts for the characteristic velocity field of the fluid. In particular this term hinders the collapse in terms of pressure, which is ingrained in the sound speed.
From the dispersion relation, considering solutions in the form of a power-law, i.e. $\delta_k \propto t^\alpha$, we can derive the behavior of perturbations smaller than the scale of the particle horizon R_H, in a matter-dominated universe. With the same arguments described in Section 1.10.2, in an EdS universe we find a propagation as waves for $\lambda < \lambda_J$, while for $\lambda > \lambda_J$ we have

$$\delta_\pm = \delta_k(t)_\pm \exp(ikx) = \exp(ikx)\, t^{\left[-1\pm5\sqrt{1-(\lambda_J/\lambda)^2}\right]/6}. \tag{1.134}$$

[8] It has to be noted that after the equivalence the baryonic matter is still coupled to radiation. Indeed the baryonic matter is decoupled, and therefore can accrete, after recombination. In general, indeed, a matter perturbation can not grow if the matter fluid is coupled to radiation, because the radiative pressure inhibits the collapse.

For the case of $\lambda \gg \lambda_J$, we then have

$$\delta_+ \propto t^{2/3} \qquad \text{(growing solution)}, \tag{1.135}$$

$$\delta_- \propto t^{-1} \qquad \text{(decaying solution)}. \tag{1.136}$$

As already mentioned, due to the expansion of the universe we do not obtain the exponential growth found in Eq. (1.126).
Turning to curved universes, the growing solution has the following expression:

$$\delta_+ \propto H(t) \int \frac{\mathrm{d}t}{H^2 a^2} \ , \tag{1.137}$$

which has no analytic solution. It is possible to derive an approximate form for the variation of the growing solution, namely the *growth factor* f:

$$f \equiv \frac{\mathrm{d}\ln\delta_+}{\mathrm{d}\ln a} \simeq \Omega_m^{0.55} + \frac{\Omega_\Lambda}{70}\left(1 + \frac{\Omega_m}{2}\right). \tag{1.138}$$

This expression is extremely important because the exponent 0.55 derives from General Relativity, therefore the measure of f is a test of General Relativity. Moreover f depends mainly on Ω_m, and this is reasonable because the matter interacts gravitationally, while the dependency on the cosmological constant Λ, which participates to the expansion of the universe, is weaker. It has to be noted that in an EdS universe $f = 1$, because from Eq. (1.135) we find $\delta_+ \propto a$. However, in our ΛCDM universe, the value of f deviates from unity.
So far we treated matter fluctuations in matter-dominated universes. However we should point out that after the equivalence and before recombination, the baryonic matter is still coupled with radiation. When recombination occurs, baryons fall in the already formed potential wells of dark matter, and this occurrence is called *baryon catch-up*. In particular the baryonic density contrast $\delta_{k,B}$ depends on the dark matter one $\delta_{k,DM}$ in terms of the scale factor at the decoupling a_{dec}:

$$\delta_{k,B} = \delta_{k,DM}\left(1 - \frac{a_{dec}}{a}\right) \tag{1.139}$$

This explains the rapid growth of the baryonic perturbations from $z \simeq 1100$ to the present day.
Lastly, we can mention the main results obtained for perturbations smaller than R_H in a radiative universe, i.e. for times $t < t_{eq}$. In this framework the Jeans scale for radiative perturbations has no physical meaning, because it is greater than the scale of the particle horizon R_H. Consequently, there are no gravitational radiative instabilities inside the horizon in this epoch. On the other hand considering dark matter perturbations in a radiative universe, on scales much greater than the Jeans scale, we find the so called *Meszaros effect*. This effect consists of a inhibited growth of the dark matter perturbations before the equivalence. In

particular the perturbations exist, but can grow at most of a factor 5/2. This effect can be intuitively explained by considering the free-fall timescale

$$\tau_{ff} = \frac{1}{\sqrt{G\rho_{DM}}} \tag{1.140}$$

and the expansion timescale

$$\tau_{exp} = \frac{1}{H} \simeq \frac{1}{G\sqrt{\rho_{DM} + \rho_r}} \tag{1.141}$$

where ρ_{DM} and ρ_r are, respectively, the density of dark matter and radiation. Therefore $\tau_{ff} \gg \tau_{exp}$ in a radiative universe, so the gravitational collapse in ineffective.

1.11 Statistical properties of the Universe

The growth of the perturbations is fundamental for the comprehension of the universe, and it is necessary to describe the probability distribution of these density fluctuations. A problem related to this is that the universe is a unique object, not reproducible, and this could make difficult the construction of a meaningful statistical framework.
However there is a solution to this. As evidenced in Eq. (1.133), we can consider the density contrast $\delta(\boldsymbol{x}) = \delta\rho(\boldsymbol{x})/\rho$, in the real space, as the fundamental property of the perturbations. It can also be expressed as

$$\delta(\boldsymbol{x}) = \frac{1}{(2\pi)^3} \int_{-\infty}^{+\infty} \delta(\boldsymbol{k}) \exp(i\boldsymbol{k} \cdot \boldsymbol{x}) \, \mathrm{d}^3\boldsymbol{k}, \tag{1.142}$$

i.e. it is the inverse Fourier transform of the imaginary $\delta(\boldsymbol{k})$. The quantity $\delta(\boldsymbol{x})$ has no dimension, while $\delta(\boldsymbol{k})$ has the dimensions of a volume.
We consider $\delta(\boldsymbol{x})$ as a *continuum* and *stochastic* field.[9] In particular we are not interested in the exact value of $\delta(\boldsymbol{x})$ in the point $\boldsymbol{x}$,[10] but the aim is to investigate the mean properties of this field. In a first instance we consider the *ergodic principle*, or fair sample principle, which states:

> *"The result of the mean of many realizations of universe is equivalent to the mean obtained considering separate, and sufficiently large, volumes in the universe."*

[9] The stochasticity of this field derives from the stochastic nature of the fluctuations generated during the inflationary era.

[10] And knowing the value of $\delta(\boldsymbol{x})$ would be operationally impossible, given that the observed matter density field is not continuum.

These volumes must be sufficiently large to be considered statistically independent, and their size depends on the cosmic epoch and on the level of non-linearity of the perturbations, which grows with time.
If the distribution of $\delta(\boldsymbol{x})$ is Gaussian, then the ergodic principle becomes a theorem. On this regard, another time the Fourier transforms show their extreme usefulness. We know that $\delta(\boldsymbol{k})$ is a stochastic field, as well as $\delta(\boldsymbol{x})$. In particular, given that $\delta(\boldsymbol{k})$ is imaginary, then also the phases of these quantities are stochastically distributed. A theorem states that:

"Imaginary numbers with casual phases are normally distributed."

The quantity $\delta(\boldsymbol{k})$ represents the decomposition in Fourier modes of the field $\delta(\boldsymbol{x})$. This implies that, if $\delta(\boldsymbol{k})$ follows a Gaussian distribution, also $\delta(\boldsymbol{x})$ is normally distributed. Therefore, the *fair sample theorem* is valid for the $\delta(\boldsymbol{x})$ field.

A fundamental statistical indicator in cosmology is the *two-point correlation function* $\xi(r)$, defined as

$$\xi(r) \coloneqq \langle \delta(\boldsymbol{x})\, \delta(\boldsymbol{x}+\boldsymbol{r}) \rangle, \tag{1.143}$$

that measures the autocorrelation of the field $\delta(\boldsymbol{x})$ in positions at a distance $\boldsymbol{r}$ from $\boldsymbol{x}$. This is a double operation of mean, because the mean is evaluated for all the positions $\boldsymbol{x}$ and for all points at a distance $\boldsymbol{r}$ from each $\boldsymbol{x}$. For the isotropy of the universe on large scales, ξ is a function of the modulus of $\boldsymbol{r}$. It is possible to write the expression for ξ in terms of Fourier transforms:

$$\xi(r) = \frac{1}{(2\pi)^6} \int \mathrm{d}^3\boldsymbol{k} \int \mathrm{d}^3\boldsymbol{k}' \langle \delta(\boldsymbol{k})\, \delta(\boldsymbol{k}') \rangle \exp[i\boldsymbol{k}\cdot(\boldsymbol{x}+\boldsymbol{r})] \exp[i\boldsymbol{k}'\cdot\boldsymbol{r}], \tag{1.144}$$

from which we define

$$\langle \delta(\boldsymbol{k})\, \delta(\boldsymbol{k}') \rangle \coloneqq (2\pi)^3 P(\boldsymbol{k})\, \delta_D^{(3)}(\boldsymbol{k}+\boldsymbol{k}'), \tag{1.145}$$

where $P(\boldsymbol{k})$ is the *power spectrum* and $\delta_D^{(3)}(\boldsymbol{k}+\boldsymbol{k}')$ is the three-dimensional Dirac delta. From this definition descends the Wiener-Khinchin theorem, which states that the two-point correlation function is the inverse Fourier transform of the power spectrum:

$$\xi(r) = \frac{1}{(2\pi)^3} \int \mathrm{d}^3\boldsymbol{k}\, P(\boldsymbol{k}) \exp(i\boldsymbol{k}\cdot\boldsymbol{r}). \tag{1.146}$$

In general the power spectrum is $P(k) \propto \langle |\delta(k)|^2 \rangle$, because

$$\langle \delta(\boldsymbol{k})\, \delta^*(\boldsymbol{k}) \rangle \equiv \langle |\delta(\boldsymbol{k})|^2 \rangle \coloneqq (2\pi)^3 P(\boldsymbol{k})\, \delta_D^{(3)}(\boldsymbol{k}-\boldsymbol{k}) \tag{1.147}$$

where $\delta^*(\boldsymbol{k})$ in the complex conjugate of $\delta(\boldsymbol{k})$, and in general $\delta^*(\boldsymbol{k}) = \delta(-\boldsymbol{k})$. Therefore $P(k)$, similarly to $\xi(r)$, depends only on the modulus of $\boldsymbol{k}$, k, and it is a mean over the set of $\{k_x, k_y, k_z\}$ that give the same value of k.[11]

[11] Moreover, for the isotropy it is not important what is the set of $\{k_x, k_y, k_z\}$ that originates a vector with modulus k.

We showed that $\delta(\boldsymbol{x})$ is normally distributed, therefore its distribution is uniquely defined by its mean and its variance. In particular the *variance* σ^2 is defined as $\sigma^2 \coloneqq \langle \delta^2(\boldsymbol{x}) \rangle$, therefore it is an operation of mean of the δ^2 over a volume, followed by a second operation of mean over many volumes. Moreover, it is possible to show that

$$\sigma^2 = \frac{1}{(2\pi)^3} \int \mathrm{d}^3\boldsymbol{k}\, P(\boldsymbol{k}), \tag{1.148}$$

i.e. the variance is a three-dimensional integral of the power spectrum $P(k)$.
However our observable is not the $\delta(\boldsymbol{x})$ field, but the distribution of the galaxies, that is not continuum. We define this observable, called δ_{gal}, considering volumes instead of single points:

$$\delta_{gal} = \frac{N_{gal}(V) - \bar{N}_{gal}(V)}{\bar{N}_{gal}(V)} = \frac{\delta N(V)}{\bar{N}(V)}, \tag{1.149}$$

where $N_{gal}(V)$ is the number of galaxies in a given volume V. Similarly, we can define the density contrast of the matter field, δ_M as

$$\delta_M = \frac{M(V) - \bar{M}(V)}{\bar{M}(V)} = \frac{\delta M(V)}{\bar{M}(V)}. \tag{1.150}$$

We can also write this relation in terms of a convolution of δ with a window function or *filter* $W(\boldsymbol{k}R)$,

$$\delta_M(\boldsymbol{x}) = \delta(\boldsymbol{x}) * W(\boldsymbol{k}R), \tag{1.151}$$

from which the *mass variance* σ_M^2 can be obtained in the form

$$\sigma_M^2 = \frac{1}{(2\pi)^3} \int \mathrm{d}^3\boldsymbol{k}\, P(\boldsymbol{k}) \hat{W}^2(\boldsymbol{k}R) \tag{1.152}$$

where $\hat{W}(\boldsymbol{k}R)$ is the Fourier transform of the window function. For high values of R, or similarly for high values of the mass M, we filter on large scales and the mass variance σ_M^2 tends to zero. Conversely, for small values of R we have $\sigma_M^2 \to \sigma^2$.
In addition, we can not know in principle if the galaxy distribution reflects the distribution of the total matter in the universe. For this reason we parametrize the relation between δ_{gal} and δ_M with a *bias factor* b:

$$\delta_{gal} = b\, \delta_M \tag{1.153}$$

The bias factor depends on the cosmology, and is defined by the Mo-White relation (Mo & White, 1996)

$$b(M, z) = 1 + \frac{1}{\delta_c} \left(\frac{\delta_c^2}{\sigma_M^2 \delta_+^2(z)} - 1 \right), \tag{1.154}$$

where δ_c is the critical density contrast for the collapse, derived in the spherical collapse formalism (described in Chapter 3).
The arguments that led to Eq. (1.150) and Eq. (1.153) affect, obviously, also the two-point correlation function $\xi(r)$. The bias factor grows with the redshift z and, particularly, with the mass M. Then we expect that galaxy clusters have a two-point correlation function larger than galaxies.

Lastly, we will focus on another fundamental topic related to the theory of the perturbations: the evolution of the power spectrum $P(k)$.

1.11.1 The evolution of the power spectrum

The power spectrum $P(k)$ can be expressed, in a first instance, as a power-law of the wavenumber k with an arbitrary amplitude A,

$$P(k) = Ak^n, \tag{1.155}$$

where n is the *spectral index*. In the linear regime we have seen that the growing solution δ_+ for the evolution of the perturbations is independent on k, or equivalently on the physical scale R.[12] This is a relevant advantage of the linear regime, for which the growth of an initial perturbation with density contrast $\delta_{in}(k)$ is modulated as $\delta_+(t)\delta_{in}(k)$. Indeed, given that $P(k) \propto \langle|\delta(k)|^2\rangle$, we therefore have a parallel shift of the initial power spectrum P_{in} with time:

$$P(k) = P_{in}(k)\delta_+^2(t). \tag{1.156}$$

It is important to point out that these arguments are valid for the primordial power spectrum. In particular the inflationary models predict a value for the spectral index $n \simeq 1$, which in terms of gravitational potential translates in perturbations with the same amplitude on all scales, giving rise to the so called *white noise*. The Planck satellite measured the value of n (Planck Collaboration 2018, Paper VI), that can be expressed as

$$n = 1 + 2\epsilon - 6\eta, \tag{1.157}$$

where ϵ and η are the *slow-roll parameters* defined in the inflationary models (see Linde, 2007), obtaining $n \simeq 0.96$. This result is extremely important because it is in accordance with the prediction of the modern models of inflation, and in addition it supports the hierarchical clustering scenario. The latter, indeed, predicts a range $-3 < n < 1$ for the spectral index.
This particular range can be derived with simple considerations. From the expression for σ_M^2, Eq. (1.152), and considering the Eq. (1.156), neglecting the effect of the window function we have

$$\sigma_M^2 \propto \delta_+^2(t)k^{n+3} \propto \delta_+^2(t)R^{-(n+3)} \propto \delta_+^2(t)M^{-(n+3)/3}. \tag{1.158}$$

[12] It is important to stress that the dimension of the wavenumber k is the inverse of a physical scale.

Now, the *assumption* for the non-linear regime is the following:

> *"The upper limit of the linear regime is in general set by $\sigma^2 \simeq 1$, $\delta \simeq 1$. When the variance of the perturbation distribution reaches the value $\sigma^2 \simeq 1$, the structures are formed and the non-linear regime is established."*

With this assumption, from Eq. (1.158) we have $1 \propto \delta_+^2(t) M_*^{-(n+3)/3}$, where M_* is the mass of the structure that forms at a given time t_*. Therefore

$$M_* \propto \delta_+^{6/(n+3)}, \tag{1.159}$$

and for a matter-dominated EdS model (a good approximation for our universe) we know that $\delta_+(t) \propto a \propto t^{2/3}$, so that

$$M_* \propto (1+z)^{-6/(n+3)} \tag{1.160}$$

and, from Table 1.1,

$$t_* \propto (1+z)^{-3/2} \propto M_*^{(3+n)/4}. \tag{1.161}$$

In a hierarchical model the formation time must be smaller for the smaller objects, therefore $n > -3$. In addition the energetic of the systems should increase with the mass, therefore $n < 1$. Then we have obtained the aforementioned range $-3 < n < 1$.
Another implication of $n \simeq 1$ is that when the perturbations begin to be contained in the particle horizon, they have the same power. We also know that, as discussed in Section 1.10.3, the dark matter perturbations that enter the horizon before the equivalence undergo the Meszaros effect, i.e. their growth is almost inhibited. In this way, before the equivalence, the perturbations enter the horizon in correspondence of the same wavenumber k and can no longer grow. On the other hand, the perturbations on scales bigger than the horizon continue to grow at the same rate, following the parallel shift of the power spectrum. As a consequence, the power spectrum at the moment of the equivalence has a peak in correspondence of k_{eq}, and is expressed in the form

$$P(k, t_{eq}) = P_{in} T^2(k) = A k^n T^2(k), \tag{1.162}$$

where $T^2(k)$ is the transfer function, whose values are $T^2(k) \propto k^0$ for $k < k_{eq}$, and $T^2(k) \propto k^{-4}$ for $k > k_{eq}$.
Moreover, non-linearity manifests itself on the small physical scales first, or in correspondence of the big wavenumbers k, indeed the variance σ^2 decreases with the physical scale. As a consequence, the probability distribution of the density contrasts δ on small scales becomes larger with time first, until the form of the distribution deviates completely from a Gaussian. Indeed the original Gaussian distribution is centered on zero, and the wing in the regime of the underdensities

con not extend to density contrasts lower than -1. This originates a non-zero skewness in the distribution, which in particular tends to privilege the formation of underdensities. This is the reason of the existence of the *cosmic web*.
Moreover, given that the non-linear regime is manifested on the small scales first, also the power spectrum changes its shape at high values of k. For this reason the power spectrum in the linear regime is reflected in the observable structures only at high redshifts, or in the evolved universe on large scales. In particular in the local universe non-linearity is reached on scales of $\sim 8\,\mathrm{Mpc}$.

1.12 Non-linearity

As discussed in the previous section, the non-linearity of perturbations is achieved when a self-gravitating structure as a galaxy or galaxy cluster is formed. In these cases, an analytic description of the evolution of the perturbations is almost impossible to attain. An analytic approach to the collapse of cosmic structures is the *spherical collapse*, which leads to the Press-Schechter formalism of the mass function, and that will be detailed in Chapter 3.
In general, however, it is necessary to use numerical methods in order to understand the non-linear nature of the structures in the universe. Therefore the exploitation of N-body simulations is mandatory, and typically the initial conditions are set through the use of the Zel'dovich approximation.

1.12.1 The Zel'dovich approximation

The Zel'dovich approximation provides remarkable results for density contrasts of the order of unity. It consists of an extension of the linear regime formalism for systems in a weakly non-linear regime, and in particular it is a Lagrangian perturbative theory at the first order.[13]
We consider a fluid whose particles are distributed on a grid, and each particle is subjected to a displacement caused by a density perturbation. The position r, in physical coordinates, can be expressed as

$$r(q,t) = a(t)\left[q - b(t)\nabla_q \phi(q)\right] \tag{1.163}$$

where q is the initial position of the particle, $a(t)q$ represents the Hubble flow with $a(t)$ dimensionless, while the second term in the brackets descends from the factorization of a perturbation $F(q,t)$. The latter represents, therefore, the displacement of the particle and ϕ is the potential of the peculiar velocity field, while $b(t)$ can represent the linear growing solution $\delta_+(t)$.

[13] In the Lagrangian point of view, the description of the fluid is based on the motion of the single particles. Conversely, the Eulerian formalism focuses on a given point of the fluid, from which we observe the passing particles.

The main limit of this approach is that the particles feel only the initial force, which causes their displacement, but in later times there are no additional interactions. This implies that two particles can cross each other without any interaction, giving rise to the so called shell-crossing problem. However these problems affect mainly the representation of the small scales, where non-linearity develops first. On large scales, but also for small times, the Zel'dovich approximation is a fundamental computational tool.
Considering the equivalence of the mass differential $\mathrm{d}M$ in the r and q coordinates, $\bar{\rho}\,\mathrm{d}^3q = \rho(r,t)\,\mathrm{d}^3r$, we obtain

$$\rho(r,t) = \frac{\bar{\rho}}{a^3}\left[\delta_{ij} - b(t)\frac{\partial^2\phi}{\partial q_i \partial q_j}\right] = \tag{1.164}$$

$$= \frac{\bar{\rho}}{a^3}\left[1 - b(t)\lambda_1\right]^{-1}\left[1 - b(t)\lambda_2\right]^{-1}\left[1 - b(t)\lambda_3\right]^{-1}, \tag{1.165}$$

where $\lambda_1 > \lambda_2 > \lambda_3$ are the eigenvalues of the symmetric deformation tensor, expressed in the brackets in Eq. (1.164). This framework is a representation of an ellipsoidal perturbation, for which the length of each axis is related to the value of the corresponding λ_i. For positive eigenvalues, given that $b(t)$ is a monotonically increasing function, the brackets $[1-b(t)\lambda_i]^{-1}$ tend to zero, making the density $\rho(r,t)$ divergent. Apart from this problem, the general idea is that the bracket containing the largest λ_i tends to zero first, and this means that the minor axis collapses first.
On the other hand, if the eigenvalues are negative the brackets can not be null at any time, and a dilatation takes place, instead of a collapse.
Therefore different combinations of positive and negative eigenvalues lead to different formed structures.

1.12.2 N-Body simulations

Computational methods are necessary in order to reproduce observations, when the non-linear regime of the perturbations manifests itself. In particular the cosmological simulations involve cubes of universe containing a large number N of point masses. We will focus on N-body simulations rather than hydro N-body simulations: the former consider only gravitational interactions between the N particles, while the latter also consider the effects of gas such as shocks, cooling, turbulence. Indeed for large simulations, i.e. for large simulated volumes of universe, accounting for the gas physics would require enormous computational times. In particular, in the specific case of simulations on grids, the resolution is not sufficient for the evaluation of these effects.
The initial conditions are set through the use of the Zel'dovich approximation. A possible method consists of particles distributed on a grid that undergo a small perturbation.

In general each of the N particles has a mass M_i, and the aim of the simulations is the resolution of the following system:

$$\begin{cases} \boldsymbol{F}_i = GM_i \sum_{i \neq j} \dfrac{M_j}{r_{ij}^2} \hat{\boldsymbol{r}}_{ij} \\ \ddot{\boldsymbol{x}}_i = \dfrac{\mathrm{d}^2 \boldsymbol{x}_i}{\mathrm{d}t^2} = \dfrac{\mathrm{d}\boldsymbol{v}_i}{\mathrm{d}t} = \dfrac{\boldsymbol{F}_i}{M_i} \\ \dot{\boldsymbol{x}}_i = \dfrac{\mathrm{d}\boldsymbol{x}_i}{\mathrm{d}t} = \boldsymbol{v}_i \end{cases} \tag{1.166}$$

where $\boldsymbol{F}_i$ is the gravitational force acting on the i-th particle, $\boldsymbol{x}_i$ and $\boldsymbol{v}_i$ are respectively the comoving coordinates and the velocity of the i-th particle, r_{ij} is the comoving distance between i-th and j-th particles, and $\hat{\boldsymbol{r}}_{ij}$ is the related versor.
Given the system (1.166), the fundamental equations to consider for gravitational interactions are, in comoving coordinates, the Euler equation

$$\frac{\mathrm{d}\boldsymbol{v}_i}{\mathrm{d}t} + 2\frac{\dot{a}}{a}\boldsymbol{v}_i = -\frac{1}{a^2}\nabla\phi = -\frac{G}{a^3}\sum_{i \neq j,\, j} M_j \frac{\boldsymbol{x}_i - \boldsymbol{x}_j}{||\boldsymbol{x}_i - \boldsymbol{x}_j||^3} = \frac{\boldsymbol{F}_i}{a^3}, \tag{1.167}$$

and, applying the second Friedmann equation (1.49), the Poisson equation

$$\nabla^2\phi = 4\pi G\bar{\rho}(t)a^2\delta = \frac{3}{2}H_0^2\,\Omega_0\frac{\delta}{a}. \tag{1.168}$$

Here a is the scale factor, $\bar{\rho}(t)$ is the average non-relativistic matter density of the universe, δ the density contrast, H_0 the Hubble constant, and Ω_0 the matter density contrast.
Given a time t, the force $\boldsymbol{F}_i$ is evaluated for each particle. Then after a time step δt are evaluated the new velocities and positions, $\boldsymbol{v}_i(t+\delta t)$ and $\boldsymbol{x}_i(t+\delta t)$, resolving the system (1.166). In these new positions is evaluated again the force, and the process is repeated iteratively at each time step.
There are different computational methods used in N-body simulations, that we will describe below: particle-particle (PP), particle-mesh (PM), particle-particle-particle-mesh ($\mathrm{P^3M}$), and hierarchical tree (HT) methods.

Particle-Particle (PP)

The PP method is the simplest method and also the most accurate, because it consists in the evaluation of the gravitational force acting on each particle at any time step. However it is the most computationally expensive, because for each time step it requires the computation of the $N(N-1)/2$ distances between the particles, i.e. the number of operations scales as $\mathcal{O}(N^2)$.

Particle-Mesh (PM)

With the PM method, the gravitational potential is computed on a regular grid with periodic boundary conditions, which allows to use the Fast Fourier Transform (FFT) methods. In particular from the interpolation of the particle positions is computed the density on the grid, from which is evaluated the FFT of the density. Consequently, thanks to the Poisson equation, it is possible to retrieve the potential on the grid and therefore the force in the Fourier space. Applying the inverse FFT one obtains the force in the real space, on the grid. Then the force acting on each particle is evaluated through an interpolation. Given that most of the operations are made in the Fourier space, the scaling of the number of operations is $\mathcal{O}(N \log N)$, better than the PP case.

Particle-Particle-Particle-Mesh ($\mathbf{P^3M}$)

The P^3M method combines and exploits the advantages of PP and PM. The gravitational force is computed most accurately by PP, therefore on small scales $\boldsymbol{F}_i$ is computed with this method. On the other hand, good and less computationally expensive results are provided by the PM method on large scales. The number of operations scales as $\mathcal{O}(k\, N \log N)$, where k is a factor depending on the chosen scale.

Hierarchical Tree (HT)

The HT method consists in the division of the simulated volume of universe in cells, whose sizes follow a hierarchy based on the spatial distribution of the particles. Firstly the volume is divided into large cells, then each cell can be subdivided in smaller ones if it contains more than one particle, and this division continues until each cell contains approximatively one particle. Considering a given particle P, the gravitational interaction is computed with the single particles if they are sufficiently close to P. On the other hand, for distant clumps of particles it is sufficient to compute the force produced by the biggest cell containing the clump, i.e. the highest cell in the hierarchy, considering its barycenter as the distance between the clump and P.
The number of operations involved with this method scales as $\mathcal{O}(N \log N)$.

Chapter 2

Galaxy clusters

Galaxy clusters, reaching masses larger than $10^{15}\,M_{\odot}$, are the biggest virialized structures present in the Universe, lying on the highest peaks of the dark matter density field. These objects are critically important probes in cosmology and their observed properties can be linked to the physical quantities of their host haloes of dark matter, modelled as functions of cosmological parameters. In this chapter we will describe the main properties of galaxy clusters and how these objects play a role in cosmological studies.

2.1 Clusters as cosmological probes

The use of clusters for cosmological studies dates back to Zwicky's discovery of dark matter in the Coma Cluster (Zwicky, 1933). Indeed the masses obtained from the measured velocity dispersions were found to exceed the total mass of all the member galaxies by factors of $\sim 200 - 400$, which implied the necessity to postulate the existence of large amounts of dark matter. A further confirmation of dark matter relied on the discovery of an extended hot intracluster medium (ICM) emitting by thermal bremsstrahlung in X-rays. Measurement of the temperature of this gas additionally implied that the depth of potential wells of clusters requires the presence of a dark component.

According to the standard model of cosmic structure formation, the *hierarchical model*, clusters are thought to be the result of a sequence of mergers and accretion of smaller systems driven by gravity and dark matter. Indeed the dark component dominates the gravitational field and the evolution of galaxy clusters can be determined, in a first approximation, simply by the initial conditions, dark matter, and gravity.

In particular, gravitational dynamics is the dominant interaction on the large scales for which the linear or weakly non-linear regime is valid. In these cases gas physics effects are negligible, and the gravitational dynamics preserves memory of initial conditions. On smaller scales instead, i.e. on scales of the galaxies, the

physical processes related to baryonic matter such as gas cooling, star formation, feedback from supernovae and active galactic nuclei produce a complex ensemble of effects on the gas, that significantly change the cosmic evolution of baryons, erasing the cosmological information. In these cases, the non-linear regime holds. Since galaxy clusters mark the transition between the two regimes of the perturbations, and additionally are the largest virialized objects in the Universe, they can be considered as extremely important tools in cosmological investigations.

Galaxies have, indeed, mass-luminosity ratios of the order of $M/L \sim 10$, therefore baryons significantly contribute to the total mass and for this reason non-linearity is dominant. On the other hand we know that in the Universe the dark matter fraction increases with the mass of the systems, and for galaxy clusters the mass-luminosity ratio is $M/L \gg 100$, where L is essentially the luminosity of the member galaxies. In these systems the dominant contribution to the baryonic component is given by the ICM, that however reaches $\sim 15\%$ of the total mass.

Consequently the formation and evolution of galaxy clusters can be described only in terms of the dark matter potential well, and this simplification also allows to run simulations of large volumes of universe reproducing the large scale structure. Accounting also for the physics of baryons is possible, albeit it is much more computationally expensive and implies strict limitations on the simulated volume.

Having a model for their evolution, galaxy clusters become powerful cosmological probes with a wide spectrum of applications. As we shall see in Chapters 3 and 5, the galaxy cluster mass function strongly depends on cosmological parameters, allowing the assessment of the evolutionary models of the Universe from the study of the distribution of galaxy clusters at different redshifts.

Moreover, the correlation function of galaxy clusters is another fundamental topic in cosmology. As discussed in Section 1.11 the two-point correlation function $\xi(r)$, as well as the general N-point correlation function are tracers of the bias factor b. Moreover the correlation function is a measure of the autocorrelation of the density contrast field, and with galaxy clusters it is possible to measure the impact of non-Gaussianity on the density field (e.g. Mana et al. 2014). Lastly, galaxy clusters are good tracers of linear and non-linear effects leading to redshift space distortions (e.g. Marulli et al. 2017).

2.2 Bulk properties

Galaxy clusters studies have developed into a broad and multiwavelength field. Observations in X-rays, optical, NIR and also gravitational lensing studies allow to study in depth these objects, as we shall discuss in the next section. These objects reach masses of $\sim 10^{15}$ $M_\odot$, generating potential wells that induce the member galaxies to reach dispersion velocities of ~ 1000 km/s.

The diffuse plasma, ICM, has on average a free electron density $n_e \sim 10^{-3}$ cm^{-3} and temperatures $T \sim 10^7 - 10^8$ K, therefore it emits in X-rays by thermal bremsstrahlung. Despite it is not associated with individual galaxies, the temperature of the ICM is consistent with the velocities of galaxies, implying that both galaxies and gas are nearly in equilibrium within a common gravitational potential well, which, we stress, includes also the dark matter contribution. This equilibrium is the basic idea of the β-model (Cavaliere & Fusco-Femiano, 1976), which remarkably describes the density radial profile of relaxed galaxy clusters, namely

$$\rho_{gas}(r) = \frac{\rho_0}{[1 + (r/r_c)^2]^{3\beta/2}}. \tag{2.1}$$

Here r_c is the core radius, while β is the ratio between the kinetic energy of galaxies defined by their one-dimensional velocity dispersion σ^2, and the thermal energy of the gas, namely $\beta = \mu m_p \sigma^2/(k_B T)$. The β-model is a flat profile in proximity of the centre and decreases towards the outskirt.

It must be noted that the assumption of equilibrium is fair only for relaxed galaxy clusters, or cool-core clusters. For clusters that underwent major mergers in the past Gyr, called non-cool-core, this assumption is not valid.

Given that the central regions in relaxed clusters are denser than the outskirt, cooling is more efficient and therefore the temperature is lower (e.g., Fabian, 1994). However spectroscopic observations with the Chandra and XMM-Newton satellites have shown that only a modest fraction of this gas cools down to low temperatures (e.g. Böhringer et al. 2001, Peterson et al. 2001). This conundrum can be solved by invoking the AGN feedback from the central dominant galaxy (e.g. Vernaleo & Reynolds, 2006).

Another important feature of galaxy clusters is the Navarro-Frenk-White profile (NFW; Navarro et al. 1997), obtained from N-body simulations. It describes the density profile of the dark matter haloes of clusters of any mass, indeed gravity has not privileged scales. Of course it is a mean profile, real clusters have different merger histories and could be not completely relaxed.

In particular the basic idea, in a hierarchical model, is that of a self-similar evolution of galaxy clusters: at any mass, clusters have the same properties. From this assumption descend important relations that link masses to more direct physical quantities, namely (see for instance Borgani, 2006)

$$T_X \propto M^{2/3}(1+z), \tag{2.2}$$

$$L_X \propto T^2(1+z)^{3/2}, \tag{2.3}$$

where T_X and L_X are, respectively, the temperature and the luminosity of the ICM from X-ray observations. However observations are in contrast with the relations (2.2) and (2.3), therefore with the self-similar growth of galaxy clusters. In particular the obtained observational relation is (e.g. Xue & Wu, 2000)

$$L_X \propto T^\alpha \qquad \text{with } \alpha \simeq 2.5 - 3, \tag{2.4}$$

flattening towards the self-similar scaling only for the very hot systems with $T_X > 10\,\mathrm{keV}$.

2.3 Detection and mass measurements

There are several methods to detect galaxy clusters and to determine their mass. Here we present the main methods to accomplish these tasks.

2.3.1 Gravitational lensing

According to general relativity, the mass of a galaxy cluster causes a distortion of the space-time geometry in the surroundings. In turn, the light rays passing near to the cluster follow a distorted path, in a phenomenon known as gravitational lensing. This can both magnify and distort the images of background sources. Specifically, when the images of background sources such as galaxies are distorted, the phenomenon is classified as weak lensing. Occasionally, if the background source is well aligned with the cluster along the line of sight, lensing can also lead to strong distortions and multiple images of individual sources, and in this case it is classified as strong lensing.

Gravitational lensing depends on the total mass of the system, and has the advantage to not rely on any assumption on the physical state of the cluster. Given a model for the surface density distribution, an estimate of the total mass is provided through the fit of the gravitational shear profile. A more detailed description of this process will be discussed in Chapter 4, in the description of the assessment of the observable-mass scaling relation for the AMICO KiDS-DR3 catalogue, exploited in this Thesis work.

2.3.2 X-ray observations

Most of the baryonic matter in the Universe is in the form of diffuse gas. In galaxy clusters, the deep potential well of the dark matter halo induces virial temperatures of $\sim 10^7 - 10^8\,\mathrm{K}$ for the diffuse ICM. The most abundant element in the Universe is hydrogen, therefore this gas is in a first approximation composed of free electrons and protons, and it emits in the X-ray through free-free interactions (bremsstrahlung). The other primary X-ray emission processes are free-bound (recombination) and bound-bound (line emissions). The emissivity in all the three cases is proportional to the square of the electron density, which ranges from $\sim 10^{-1}\,\mathrm{cm}^{-3}$ in the inner regions of bright cool core clusters to $\sim 10^{-5}\,\mathrm{cm}^{-3}$ in the outskirts, implying an optically thin regime and therefore a non-auto-absorbed emission.

Observing this emission in the X-rays allows in a first instance to detect galaxy clusters, but also to determine their mass. This is possible if one assumes

a spherically distributed ICM in hydrostatic equilibrium, namely

$$\frac{\mathrm{d}P_{gas}}{\mathrm{d}r} = -\rho_{gas}\frac{\mathrm{d}\phi}{\mathrm{d}r} = -\rho_{gas}\frac{GM(r)}{r^2} \ , \tag{2.5}$$

where P_{gas} and ρ_{gas} are, respectively, the pressure and density of the baryonic gas composing the ICM, while ϕ is the gravitational potential of the system. Therefore, assuming the equation of state of ideal gas, the total mass contained within the radius r, $M(r)$, can be expressed as

$$M(r) = -\frac{r}{G}\frac{kT}{\mu m_p}\left(\frac{\mathrm{d}\ln\rho_{gas}}{\mathrm{d}\ln r} + \frac{\mathrm{d}\ln T}{\mathrm{d}\ln r}\right), \tag{2.6}$$

where μ is the mean molecular weight ($\mu \simeq 0.59$ for primordial composition[1]), and m_p is the mass of the proton. In order to describe the density profile of the ICM usually is assumed a β-model, described in Section 2.2.

On the other hand, the temperature profile $T(r)$ is determined by performing X-ray observations at different distances from the centre of the cluster: the exponential cut-off of the bremsstrahlung spectrum, if the gas density is known, provides the value of T.

Having the temperature and density profiles, the Eq. 2.6 provides a measure of the total mass. The problem with this method, however, is that the estimated masses are $\sim 15-20\%$ lower than those obtained via lensing analyses. The reason is that in Eq. 2.6 are not included the contributions to the pressure from turbulence, magnetic fields and interactions with cosmic rays.

Lastly, as we already have seen in Section 2.2, the Eq. (2.4) provides a scaling relation between X-ray luminosity and temperature, from which it is possible to derive a mass-temperature relation, whose first calibration has been presented in Reiprich & Böhringer, 2002.

2.3.3 Optical and NIR observations

Through optical and near-infrared (NIR) observations of galaxies it is possible to identify clusters and determine their mass. Historically galaxy clusters were identified as overdensities of galaxies in optical images, and Abell (Abell, 1958) provided the first catalogue based on this method. However this technique is subject to projection effects, for which field galaxies along the line of sight could be mistakenly identified as members of a cluster.

A solution to this problem is to exploit the photometric properties characterizing the galaxies in a cluster. Galaxy clusters contain a well-defined, highly regular population of elliptical and lenticular galaxies, observed in optical and NIR bands. These member galaxies in a color-magnitude diagram (e.g. a (B-R)

[1]Note, however, that the ICM has not primordial composition due to supernova and AGN feedback from galaxies.

- R diagram) dispose along a sequence, called *red-sequence* (Bower et al. 1992). In particular it is a tight linear relationship between color and magnitude, showing that the redder galaxies are brighter. Therefore it plays a considerable role in the identification of galaxy clusters. An algorithm based on red-sequence is redMaPPer (Rykoff et al. 2014), widely used to build up cluster catalogues from SDSS surveys.

There are also other detection algorithms that do not rely on the red-sequence. For example the AMICO algorithm, that will be extensively described in Chapter 4, assumes a model for the density and luminosity profiles of galaxy clusters, and identify them by finding galaxy overdensities and matching them with the defined model. In particular, in this case each galaxy has an assigned probability to be a member of a cluster or to be part of the field.

The algorithms described above are based on photometric data and provide mass proxies as direct observables, allowing the calibration of a richness-mass scaling relation, where the richness is a measure of the number of member galaxies in a cluster. This is possible thanks to data from lensing, whose effects depend on the whole distribution of matter in a galaxy cluster. It has to be noted, however, that a richness-mass scaling relation is strictly related to the algorithm used and to the data, therefore the calibration must be carried out for each dataset.

Let us now turn to another method to estimate the mass of galaxy clusters, this time based on spectroscopic data. Given the redshift and the position in the cluster of a large number of member galaxies, under the assumption of virial equilibrium the mass is given by

$$M = \frac{\pi}{2}\frac{3\sigma_v^2 R_V}{G} \ , \tag{2.7}$$

where $\pi/2$ accounts for geometry projection, σ_v^2 is the velocity dispersion along the line of sight and R_V is the virialization radius. The latter is defined as

$$R_V = N^2 \left(\sum_{i>j} r_{ij}^{-1} \right)^{-1} \ , \tag{2.8}$$

where r_{ij} is the distance projected onto the sky between the i-th and j-th galaxy, and N is the number of member galaxies. This method, however, has the problem of the contribution from galaxies along the line of sight misidentified as members of the cluster. This in general leads to overestimations of M.

2.3.4 Sunyaev Zel'dovich effect

CMB photons passing through the ICM of a galaxy cluster undergo a shift in frequency due to inverse Compton with free electrons, known as Sunyaev-Zel'dovich effect (SZ; Sunyaev & Zel'dovich, 1972) or thermal SZ effect (tSZ). Therefore

the low-frequency photons gain energy and the result is a distortion of the black body spectrum of the CMB, consisting in a lower number of photons with frequency $\nu < \nu_0 \simeq 217\,\mathrm{GHz}$, and accordingly an higher number with frequency $\nu > \nu_0 \simeq 217\,\mathrm{GHz}$. In particular ν_0 is a characteristic frequency, in correspondence of which the spectrum is not distorted.

This effect is merely a spectral distortion and does not depend on redshift, indeed in the low frequency approximation it induces variations in the intensity I of the signal equal to

$$\frac{\partial I}{I} = \frac{\partial T}{T} = -2\frac{\sigma_T}{m_e c^2}\int P_e \,\mathrm{d}l, \tag{2.9}$$

where σ_T is the Thomson cross-section, m_e the electron mass, c the speed of light, P_e the thermal pressure of the free electrons integrated along the distance traveled by photons in the ICM. The typical signal variation is $\partial I/I \sim 10^{-4}$, therefore this effect is not negligible since the CMB shows variations of the order of $\sim 10^{-5}$.

As evidenced in Eq. 2.9, in contrast to X-ray and optical measurements, the SZ signal of a cluster does not undergo surface brightness dimming. As a consequence, SZ surveys are well-suited to search for massive clusters at high redshifts. Current measurements of tSZ are carried out with the South Pole Telescope (Vanderlinde et al. 2010), the Atacama Cosmology Telescope (Marriage et al. 2011) and also with the Planck satellite (Erler et al. 2018). Moreover, tSZ provides a reliable estimate of the thermal pressure by free electrons, therefore in combination with measurements of the temperature from X-ray observations it contributes to mass measurements (see for instance Grego et al. 2000).

Another effect on CMB spectrum from inverse Compton scattering in galaxy clusters is the kinetic SZ (kSZ; Carlstrom, Holder & Reese, 2002). This effect is due to Doppler effect of clusters with a non-zero peculiar velocity along the line of sight, i.e. a proper motion with respect to the Hubble flow. In this case, differently from tSZ, the shape of the spectrum does not undergo distortions but the bulk temperature of the CMB spectrum changes. Therefore the kSZ is a good tracer of the peculiar velocity field, despite it induces variations in temperature $|\partial T/T| \sim 10^{-5}$, an order of magnitude lower than those produced by tSZ.

Chapter 3

Galaxy cluster mass function

This Thesis work is based on the observed galaxy cluster mass function, defined as the number density of virialized haloes at a given redshift and in a range of masses. The mass function plays a crucial role in cosmology since it depends on fundamental cosmological parameters. Moreover, the specific mass regime of galaxy clusters is considered, because as already discussed in Chapter 2 these objects mark the transition between the linear and the non-linear regime of the gravitational perturbations, so that their formation and evolution can be theoretically described with good accuracy.

In particular the dark component of matter is dominant, therefore it is possible to model the mass function of galaxy clusters accounting only for the dark matter contribution, neglecting the non-linear effects related to the ordinary matter. For this reason, in the literature the theoretical mass functions are modeled as the number density of virialized dark matter haloes. Additionally, it is important to point out that many attempts have been made in order to consider the gas component in the models of galaxy clusters, but as we shall see the results obtained in different works do not converge yet.

3.1 Spherical collapse

Despite galaxy clusters do not reach the level of non-linearity that characterizes the physical scales of the galaxies, their formation and evolution can not be described properly within the linear regime. Numerical simulations are therefore necessary, since the non-linear regime can not be treated analytically.

However it is possible to make use of a simple and analytic approach for the collapse of an inhomogeneity, the *spherical collapse*, which leads to the Press-Schechter formalism for the mass function. The spherical collapse is based on the following assumptions:

- Initially spherical perturbation, so that it is possible to describe it as a closed universe;

- In order to be spherical the perturbation must be spatially small, otherwise it would be more likely to have asymmetric geometries;
- At the initial time t_i the density contrast δ_i is small, $0 < \delta_i \ll 1$;
- The perturbation expands with the background universe, therefore the initial peculiar velocity at the edge is null, with a Fourier mode $v_{k,i} = 0$;
- The background universe is described by an EdS model in the matter era, i.e. the initial time is greater than the time of the equivalence t_{eq}.

In a dust EdS universe the growing and decaying modes of a perturbation are described, respectively, by Eq. (1.135) and Eq. (1.136). Combining and parametrizing the contributions of these modes, the density contrast δ can be expressed in such a way

$$\delta = \delta_+(t_i) \left(\frac{t}{t_i}\right)^{2/3} + \delta_-(t_i) \left(\frac{t}{t_i}\right)^{-1}, \tag{3.1}$$

where the subscript $'+'$ denotes the growing mode, and $'-'$ the decaying one. Moreover, in the linear regime it is possible to derive the form of the continuity equation for the Fourier modes, in comoving coordinates, as

$$\dot{\delta_k} + i\,\frac{k_{com} v_k}{a} = 0, \tag{3.2}$$

from which

$$v_k = \frac{ia\dot{\delta_k}}{k_{com}}\ . \tag{3.3}$$

where k_{com} is the wavenumber in comoving coordinates. From Table 1.1 we know that $a \propto t^{2/3}$, and combining Eq. (3.1) with Eq. (3.3) we obtain, for $t = t_i$ and in turn $v_{k,i} = 0$,

$$\frac{2}{3}\delta_+(t_i) - \delta_-(t_i) = 0 \ \ \rightarrow \ \ \delta_-(t_i) = \frac{2}{3}\delta_+(t_i). \tag{3.4}$$

Therefore Eq. (3.1) for $t = t_i$ becomes

$$\delta_i = \delta_+(t_i) + \delta_-(t_i) = \frac{5}{3}\delta_+(t_i) \ \ \rightarrow \ \ \delta_+(t_i) = \frac{3}{5}\delta_i. \tag{3.5}$$

Then the remaining 2/5 of δ_i decays with time, tending to become negligible.

The collapse is described in terms of a closed universe, therefore the density parameter of the perturbation has to be $\Omega_p > 1$. In particular

$$\Omega_p(t_i) = \frac{\rho_p(t_i)}{\rho_c(t_i)} = \frac{\rho_b(t_i)(1+\delta_i)}{\rho_c(t_i)} = \Omega(t_i)(1+\delta_i), \tag{3.6}$$

where ρ_c is the critical density and ρ_b the background density, therefore $1+\delta_i = \Omega_p(t_i)/\Omega_b(t_i)$. Thus for a closed universe it is necessary that $(1+\delta_i) > 1/\Omega_b(t_i)$, and from the Eq. (1.95) describing the evolution of the density parameter in a Friedmann universe we obtain

$$\delta_+(t_i) = \frac{3}{5}\delta_i > \frac{3}{5}\frac{1-\Omega_{0,b}}{\Omega_{0,b}(1+z)} \quad . \tag{3.7}$$

Hence, if the background universe has $\Omega_{0,b} \geq 1$ then any positive density contrast leads to a gravitational collapse, while for open universes the expansion inhibits the collapse if δ_i is not enough greater than zero.

The Friedmann equation (1.66) in a closed universe has parametric solutions described by Equations (1.86) and (1.87), and for $\theta = \pi$ is defined the time t_{max} for which the perturbation reaches the maximum expansion. More in detail, the perturbation expands with the expansion of the background universe until it reaches the maximum physical scale R_{max} at the time t_{max}. After this time, the evolution of the perturbation undergoes a *turn-around* and the collapse takes place.

It is possible to obtain that the density of the perturbation in correspondence of the moment of maximum expansion is

$$\rho_p(t_{max}) = \frac{3\pi}{32Gt_{max}^2} \tag{3.8}$$

and, knowing the value for ρ_b from Table 1.1, the corresponding density contrast is

$$\delta_+(t_{max}) \simeq \frac{\rho_p(t_{max})}{\rho_b(t_{max})} - 1 = \left(\frac{3\pi}{4}\right)^2 - 1 \simeq 4.6. \tag{3.9}$$

Thus from the definition of non-linearity given in Section 1.11.1 we see that the perturbation is already in a non-linear regime before the collapse.

After the turn-around the physical scale of the perturbation decreases until the time $t_{coll} = 2t_{max}$, when the collapse is arrested by internal thermal motions.[1] Then the perturbation has oscillations around the scale reached at time t_{coll}, which will not change in later times and therefore is equal to the virialization scale R_{vir}. In particular from numerical simulations we know that the virialization is reached at a time $t_{vir} = 3t_{max}$.

From the virial theorem in scalar form, the total energy of the perturbation is

$$E_{tot}(t_{vir}) = -\frac{1}{2}\frac{3}{5}\frac{GM^2}{R_{vir}}, \tag{3.10}$$

and, in absence of mass and energy losses since the time t_{max}, we can set

$$E_{tot}(t_{max}) = E_{tot}(t_{vir}) \quad \rightarrow \quad -\frac{1}{2}\frac{3}{5}\frac{GM^2}{R_{vir}} = \frac{3}{5}\frac{GM^2}{R_{max}}, \tag{3.11}$$

[1] For the baryonic matter the pressure hinders the collapse. On the other hand, for a dark matter fluid this role is played by the velocity dispersion of the particles.

because at $t = t_{max}$ the only contribution to E_{tot} is given by the potential energy. Thus we obtain

$$R_{vir} = \frac{R_{max}}{2}, \tag{3.12}$$

Therefore the density at $t = t_{vir}$ is $\rho_p(t_{vir}) = 8\rho_p(t_{max})$. Then we obtain that

$$\delta_+(t_{coll}) \simeq \frac{8\rho_p(t_{max})}{\rho_b(t_{max})} \left(\frac{t_{coll}}{t_{max}}\right)^2 \simeq 180, \tag{3.13}$$

$$\delta_+(t_{vir}) \simeq \frac{8\rho_p(t_{max})}{\rho_b(t_{max})} \left(\frac{t_{vir}}{t_{max}}\right)^2 \simeq 400. \tag{3.14}$$

It is important to point out that these results depend on the background cosmology, which in this case is a matter-dominated EdS model. The extrapolation of the linear growth, for which $\delta_+ \propto t^{2/3}$, would give instead

$$\delta_+(t_{coll}) \simeq \frac{3}{5}\left(\frac{3\pi}{4}\right)^{2/3} \left(\frac{t_{coll}}{t_{max}}\right)^{2/3} \simeq 1.68, \tag{3.15}$$

$$\delta_+(t_{vir}) \simeq \frac{3}{5}\left(\frac{3\pi}{4}\right)^{2/3} \left(\frac{t_{vir}}{t_{max}}\right)^{2/3} \simeq 2.2\,. \tag{3.16}$$

3.2 Press-Schechter formalism

An analytic expression for the mass function, proposed by Press and Schechter (PS; Press & Schechter, 1974), derives from the model of spherical collapse. The basic idea is that the objects form in correspondence of matter overdensities, thus it is necessary to know their probability distribution. In the PS formalism is assumed a Gaussian probability distribution for the filtered density contrast δ_M defined in Eq. (1.150), namely

$$P(\delta_M) = \frac{1}{\sqrt{2\pi\sigma_M^2}} \exp\left(-\frac{\delta_M^2}{2\sigma_M^2}\right), \tag{3.17}$$

where σ_M^2 is the filtered mass variance.[2] As discussed in Section 1.11.1, the Gaussian form of $P(\delta_M)$ holds only in a linear regime. The evolution of perturbations and consequently the entrance in the non-linear regime cause a deviation from Gaussianity, manifested in a non-zero skewness of the probability distribution.

Coherently with this assumption for $P(\delta_M)$, the chosen threshold for the filtered density contrast describing collapsed structures is $\delta_c \simeq 1.68$, obtained

[2]The filtered density contrast is $\delta_M = \delta(x) * W(k, M)$, i.e. a convolution between the density contrast and the filter. The advantage of the convolution is that it does not affect the probability distribution, therefore if $\delta(x)$ has a Gaussian distribution the same will be valid for δ_M.

in Eq. (3.15) by extrapolating the linear theory in the spherical collapse approximation. Therefore we can define the probability that a fluctuation δ_M exceeds the critical value δ_c, namely

$$P_{>\delta_c}(M) = \int_{\delta_c}^{\infty} P(\delta_M)\,\mathrm{d}\delta_M, \tag{3.18}$$

which directly depends on the mass M defined by the filter and also on redshift, because σ_M is time-dependent. In particular in the PS formalism only the isolated collapsed structures are considered, i.e. those surrounded by underdense regions, characterized by the probability

$$P_{>\delta_c}(M) - P_{>\delta_c}(M + \mathrm{d}M). \tag{3.19}$$

In this way, however, is totally ignored the *cloud-in-cloud problem*, which takes into account the possibility that a given overdensity, initially isolated, can be contained within another object on a larger mass scale at a later time. Only the objects that have just collapsed are considered, i.e. those who have just reached the threshold δ_c. In this regard it is important to stress that the mass scale M is defined by the filter and affects the probability $P_{>\delta_c}(M)$.

Another problem related to the assumption contained in (3.19) is that the underdense regions are not treated. In turn an half of the mass is not considered, for symmetry of the Gaussian distribution. Therefore a factor 2 is introduced, representing the accretion from underdense regions onto the overdensities, so that

$$n(M)M\mathrm{d}M = 2\bar{\rho}_m \left[P_{>\delta_c}(M) - P_{>\delta_c}(M + \mathrm{d}M)\right] = \tag{3.20}$$

$$= 2\bar{\rho}_m \left|\frac{\mathrm{d}P_{>\delta_c}}{\mathrm{d}\sigma_M}\right| \left|\frac{\mathrm{d}\sigma_M}{\mathrm{d}M}\right| \mathrm{d}M, \tag{3.21}$$

therefore the expression of the PS mass function is

$$n(M)\mathrm{d}M = \sqrt{\frac{2}{\pi}} \frac{\bar{\rho}_m}{M^2} \frac{\delta_c}{\sigma_M} \left|\frac{\mathrm{d}\ln\sigma_M}{\mathrm{d}\ln M}\right| \exp\left(-\frac{\delta_c^2}{2\sigma_M^2}\right) \mathrm{d}M \tag{3.22}$$

To sum up, the PS formalism relies on strong and problematic assumptions: the spherical collapse and the factor 2. It is possible to show that, in the random walk theory, the factor 2 is merely an artifact of overcounting due to cloud-in-cloud effects (Bond et al. 1991). Therefore the main problem of the PS mass function is the spherical collapse. In this regard, Sheth and Tormen (Sheth & Tormen, 1999) generalized the geometric description introducing the triaxial collapse, calibrating the free parameters of the mass function through the use of numerical simulations.

Despite the problems residing in the Press-Schechter formalism, it produces results in good agreement with N-body simulations.

3.3 Mass function in literature

The modern theoretical mass functions in the mass regime of galaxy clusters, i.e. from $\sim 10^{13}$ to $\sim 10^{15}\,\mathrm{M}_{\odot}$, are derived from numerical simulations, given the absence of analytic methods that accurately describe N-body systems in a non-linear or weakly non-linear regime. A general approach to find collapsed objects in these simulations is based on the definition of a spherical overdensity, around density peaks, within which is estimated the value of the mass. Alternatively, the friends-of-friends (FoF) is another method that allows to find collapsed structures. In this case, given an halo, the algorithm looks for other haloes at a distance smaller than a certain fraction of the mean interparticle distance. This procedure is iterated for each object, and finally ensembles of haloes constitute big collapsed structures. However the relation between the FoF masses and observables is quite uncertain.

The general form of the mass function can be expressed as a differential volume density $\mathrm{d}n(M,z)$,

$$\frac{\mathrm{d}n(M,z)}{\mathrm{d}M} = f(\sigma_M, z)\frac{\bar{\rho}_m}{M}\frac{\mathrm{d}\ln\sigma_M^{-1}}{\mathrm{d}M}\,, \tag{3.23}$$

where $\bar{\rho}_m$ is the mean cosmic background density and $f(\sigma_M, z)$ is the multiplicity function. The latter has a different functional form on the basis of the different assumptions considered in the model. As a reference, for the PS formalism we have

$$f(\sigma_M, z) = \sqrt{\frac{2}{\pi}}\frac{\delta_c}{\sigma_M}\exp\left(-\frac{\delta_c^2}{2\sigma_M^2}\right). \tag{3.24}$$

We point out that the exponential contribution characterizes all the multiplicity functions in literature.

As shall be discussed in Chapter 5, the theoretical model employed in this Thesis work is the commonly used Tinker mass function (Tinker et al. 2008). In addition to this model, several new models have been developed (e.g. Watson et al. 2013; Despali et al. 2016) that use higher resolution simulations and better statistics. However, differences still remain between them.

Moreover, by considering the Tinker halo mass function, the modelling of gas physics and galaxy formation is neglected. The Tinker model indeed, as well as the great part of the mass functions in literature, only accounts for the masses of dark matter haloes. However baryons affect the collapse of dark matter haloes and then alter the mass function (Stanek et al. 2009), and this effect can be included in the models (e.g. Velliscig et al. 2014; Bocquet et al. 2016). Nevertheless, the contribution of the gas is still uncertain and varies between different simulations and codes.

3.4 Dependency on cosmological parameters

From the general form expressed in Eq. 3.23, it is evident that the mass function depends on fundamental cosmological parameters and redshift. In the following we will present the main features of the mass function, with a particular focus on the parameters that will be constrained through the exploitation of the AMICO KiDS-DR3 catalogue, as discussed in Chapter 5.

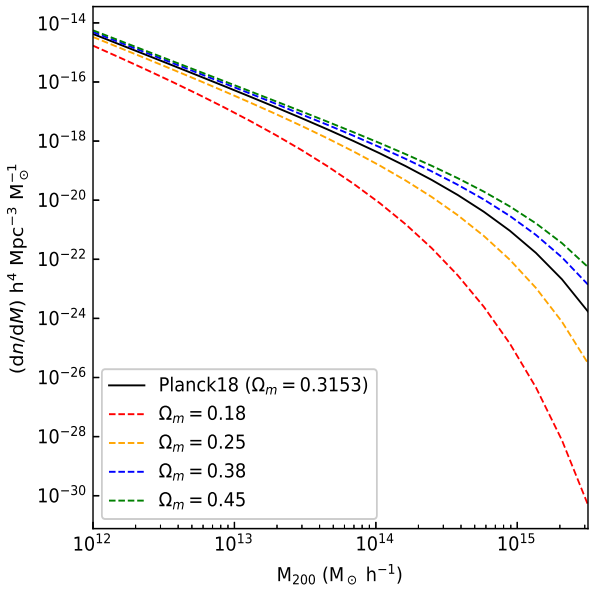

Figure 3.1: Mass function (Tinker et al. 2008) at $z = 0$ computed for the parameters obtained by the Planck satellite (Planck Collab. 2018, Paper VI: Table 2, TT,TE,EE+lowE+lensing, black solid line), and for different values of Ω_m (dotted lines) at fixed redshift. The value of Ω_m affects normalization of the mass function and the exponential cutoff.

In a first instance the presence of $\bar{\rho}_m$ implies a direct dependency on the density parameter Ω_m, which as discussed in Section 1.9 is one of the six fundamental parameters of the Universe.[3] Moreover Ω_m affects the mass function by means of the growth factor f:

$$f \equiv \frac{\mathrm{d}\ln\delta_+}{\mathrm{d}\ln a} \simeq \Omega_m^{0.55} + \frac{\Omega_\Lambda}{70}\left(1 + \frac{\Omega_m}{2}\right). \tag{3.25}$$

Indeed the mass function depends on the filtered mass variance σ_M^2, namely

$$\sigma_M^2 = \frac{1}{(2\pi)^3}\int \mathrm{d}^3\boldsymbol{k}\, P(\boldsymbol{k})\hat{W}^2(\boldsymbol{k}R), \tag{3.26}$$

[3]The importance of Ω_m and the other density parameters is that their sum is related to the geometry of the universe, and they define the evolution of $H(z)$ through Eq. (1.68).

which is, therefore, an integral of the power spectrum $P(k) = \delta_+^2 A k^n T^2(k)$.

In the expression of $P(k)$, δ_+ is the growing solution, that for a generic universe has the form of f, Eq. (3.25). Qualitatively, for higher values of Ω_m, going from $z = 0$ to higher redshifts we will have a lower number of objects at high masses. Additionally, in Fig. 3.1 we can see how different values of Ω_m affect the mass function at a fixed redshift: both the normalization and the exponential cutoff vary.

Turning to the specific case of σ_M^2, the quantities k^n, i.e. the power law of the primordial power spectrum, and $T^2(k)$, i.e. the transfer function that describes the physical processes occurred before the equivalence, are integrated and therefore they weakly affect the mass function. On the other hand the amplitude of the primordial power spectrum A and the growing mode δ_+ are constants in the integral, implying a strong dependency of the mass function on these parameters. Additionally we point out that A is another fundamental parameter of the standard cosmological model. In particular the amplitude can be parametrized by means of σ_8^2, the mass variance σ_M^2 computed on scales of 8 Mpc/h at redshift $z = 0$, where $\mathrm{h} = H_0/100$. The reason of this choice descends from the fact that in the local universe $\sigma_8 = 1$, therefore the objects on scales smaller than 8 Mpc/h are defined as in a non-linear regime. In Fig. 3.2 are shown several mass functions with different values of σ_8, while in Fig. 3.3 is given the mass function at different redshifts.

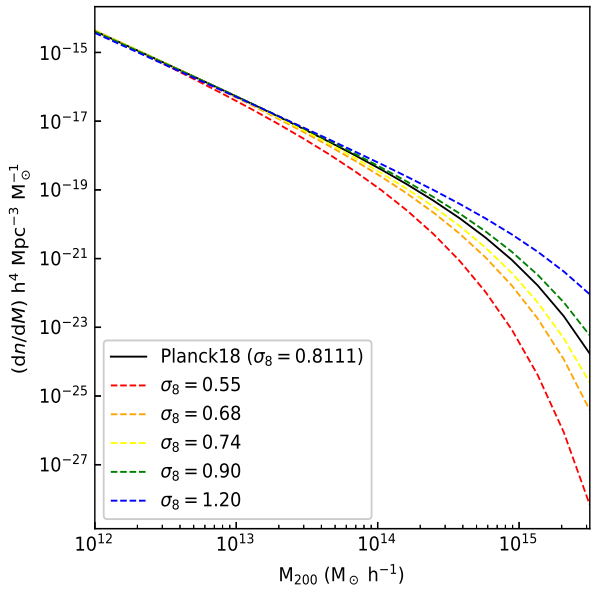

Figure 3.2: Mass function (Tinker et al. 2008) at $z = 0$ computed for the parameters from the Planck satellite (Planck Collab. 2018, Paper VI: Table 2, TT,TE,EE+lowE+lensing, black solid line), and for different values of σ_8 (dotted lines), at fixed redshift. As for the case of Ω_m, lower values of σ_8 imply a lower normalization of the mass function and also affect the exponential cutoff.

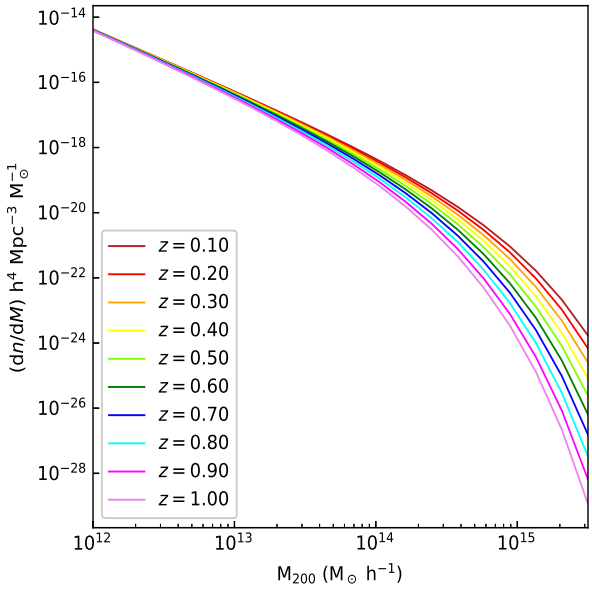

Figure 3.3: Mass function computed at different redshifts, in the range $z \in [0.1, 1]$. The number density of virialized haloes regularly decreases with increasing z.

The parameters Ω_m and σ_8 will be the main focus of the analysis described in Chapter 5, and are related to each other by means of a degeneracy expressed, in general, as

$$\sigma_8 = c\,\Omega_m^{-\gamma}, \tag{3.27}$$

where c and γ are positive parameters, and depend on the direction of the degeneracy along the confidence regions in the parameter space defined by Ω_m and σ_8.

Another fundamental parameter that affects the mass function is w_{DE}, which characterizes the dark energy equation of state expressed as

$$w_{DE} = \frac{p_\Lambda}{\rho_\Lambda c^2}. \tag{3.28}$$

This equation represents the general form of a perfect fluid equation of state, as already discussed in Section 1.8.3. In the ΛCDM model $w_{DE} = -1 = \text{const}$, and this value derives from the definition of the cosmological constant within the energy momentum-tensor (see Section 1.8.2). A famous alternative to the ΛCDM value of w_{DE} is the Chevallier-Polarski-Linder parameterization (CPL, Chevallier & Polarski, 2001; Linder, 2003), for which the parameter of the equation of state depends on redshift:

$$w_{DE}(z) = w_0 + w_a \frac{z}{1+z}. \tag{3.29}$$

Here w_0 is the value of w_{DE} at the present cosmic time, while w_a accounts for the first derivative of w_{DE} with respect to redshift. In literature, these models

in which the equation of state of dark energy changes with cosmic time are also called *quintessence models*.

In the ΛCDM model the energy density of dark energy is a constant, as evidenced by the expression of the density ρ_Λ (see Section 1.8.3):

$$\rho_\Lambda = \rho_{0,\Lambda}(1+z)^{3(1+w_{DE})}. \tag{3.30}$$

On the other hand, allowing w_{DE} to vary with time implies a variation of the energy density itself, and this affects the growth of the perturbations. A value $-1 < w_{DE} < -1/3$ implies that ρ_Λ grows with redshift, while for $w_{DE} < -1$ the density decreases. An increase of ρ_Λ could imply an increase of Ω_Λ, and therefore in a flat universe, for which $\Omega_{tot} = 1$, we would have a delay of the structure growth as we can see in Eq (3.25). However the increase of Ω_Λ is not assured because it also depends on the critical density, which in turn depends on the Hubble parameter $H(z)$. More specifically, considering the Friedmann equation in the form (1.68) we have, for a general model of universe,

$$H^2(z) = H_0^2\left[\left(1-\sum_i \Omega_{0,w_i}\right) + \Omega_{0,r}(1+z)^4 + \Omega_{0,m}(1+z)^3 + \right.$$
$$\left. + \Omega_{0,\Lambda}(1+z)^{3(1+w_0+w_a)}e^{-3w_a[z/(1+z)]}\right]. \tag{3.31}$$

If $w_{DE}(z)$ is such that the Hubble parameter increases, then the critical density increases. This would compete with the increase of ρ_Λ for the final value of Ω_Λ.

Moreover if $H(z)$ increases then the cosmic distances decrease and, in turn, the number of galaxy clusters at a given redshift changes. In this sense we can say that there is a degeneracy between Ω_m and w_{DE}, given that Ω_r at the present day is negligible. Another degeneracy between w_{DE} and Ω_m manifests itself in the flat universes because of the direct dependency of the mass function on ρ_m, which decreases for higher values of Ω_Λ.

As we shall see in Chapter 5, constraining both w_0 and w_a along with the fundamental parameters Ω_m and σ_8 is unfeasible, because of the huge amount of degeneracies at stake. In addition, w_0 and w_a slightly affect the shape of the mass function, as shown in Fig. 3.4 and 3.5, and in particular the effect of w_a is almost negligible. As a consequence, current observations have not the required accuracy to measure w_0 and w_a separately, so that the only reliable measurements of the equation of state of the dark energy are on w_0 assuming $w_a = 0$. The danger with this assumption is, however, that if the true w_a would strongly deviate from zero then the estimated w_0 would be biased correspondingly.

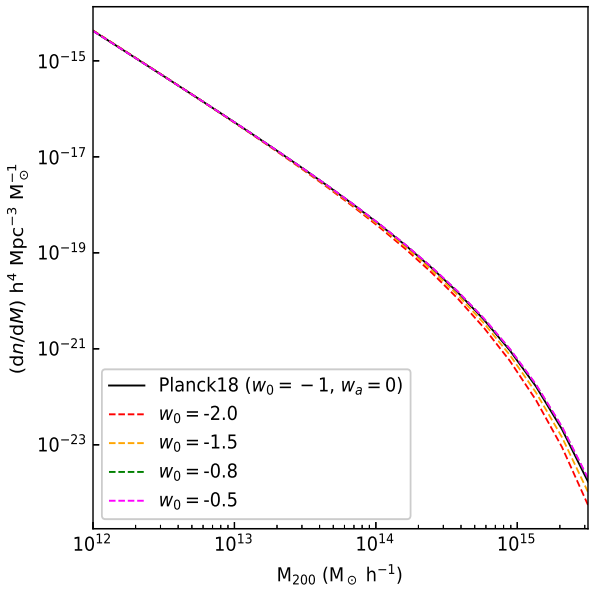

Figure 3.4: Mass function (Tinker et al. 2008) computed for the parameters from the Planck satellite (Planck Collab. 2018, Paper VI: Table 2, TT,TE,EE+lowE+lensing, solid line), and for different values of w_0 (dashed lines), at fixed redshift. We stress that in order to consider the dark energy as related to a repulsive force, w_0 (or w_{DE}) must be $< -1/3$. The impact of this parameter on the mass function is much lower with respect to the effects caused by Ω_m and σ_8.

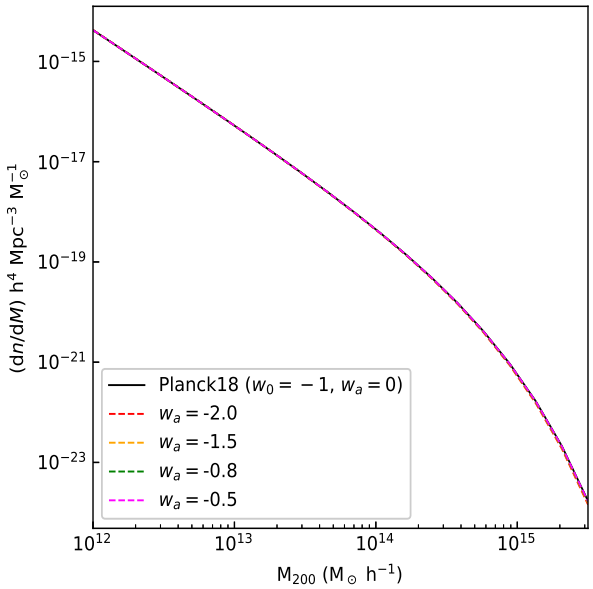

Figure 3.5: A case similar to that in the previous figure, but with fixed w_0 and varying w_a, for a fixed redshift. The impact of the parameter w_a on the mass function is negligible.

Chapter 4

The cluster sample

The goal of this Thesis work is to constrain the fundamental cosmological parameters through the observed mass function of galaxy clusters at different redshifts. The catalogue of galaxy clusters, named AMICO KiDS-DR3, is based on the third data release of the Kilo Degree Survey (KiDS), a photometric dataset of galaxies. Galaxy clusters have been identified through the use of the AMICO algorithm, described in this chapter.

The catalogue is very rich and covers a wide range of redshift, compared to the ones previously used for cosmological analyses on galaxy clusters, e.g. the works by Costanzi et al. (2018) on SDSS, and by Pacaud et al. (2018) on X-ray selected clusters. Even more importantly, the dataset in general allows a high precision analysis, thanks to the availability of a model-independent selection function.

4.1 AMICO: the detection algorithm

AMICO, *Adaptive Matched Identifier of Clustered Objects* (Bellagamba et al. 2017), is a detection algorithm aimed at identifying galaxy clusters given a photometric dataset of galaxies. In particular, through the use of AMICO it has been possible to build up the catalogue of galaxy clusters used in this Thesis work (Maturi et al. 2018).

4.1.1 Description of the algorithm

AMICO is an algorithm based on Optimal Filtering, a technique that allows to extract a signal from a noisy background maximizing the signal-to-noise ratio (S/N). In particular, in Bellagamba et al. (2011) is shown that in the case of photometric detections, under the assumption of a homogeneous background, the Optimal Filter is actually corresponding to a Matched Filter. Through a Matched Filter the signal is identified by a correlation between a template and the signal itself.

The basic assumption of the AMICO algorithm is, indeed, that the background of field galaxies is uniform. Then the general approach of the algorithm is that of a Matched Filter: given a model, the clusters in the field are identified as the regions with the maximum likelihood, which is computed accounting for the data and the model itself.

The formalism of Optimal Filtering is highly generic and allows to consider or neglect any galaxy property in the model. The algorithm, indeed, finds the most reliable properties to accomplish the detections in a given dataset, assigning the appropriate weights to the galaxies in the catalogue. Thanks to this flexibility, optical data can be combined with other observables such as weak gravitational lensing, Sunyaev-Zel'dovich effect, X-rays observations.

The basic assumption of Optimal Filtering is that a dataset D can be expressed as the sum of a signal component, described by a model M with a normalization A, and a noise component N. In the framework of cluster detections, the data are expressed as the galaxy density $D(\boldsymbol{\theta}, \boldsymbol{m}, z)$, which is a function of the angular position $\boldsymbol{\theta}$, the magnitudes $\boldsymbol{m}$ and the redshift z:

$$D(\boldsymbol{\theta}, \boldsymbol{m}, z) = A(\boldsymbol{\theta_c}, z_c)\, M_c(\boldsymbol{\theta} - \boldsymbol{\theta_c}, \boldsymbol{m}, z) + N(\boldsymbol{m}, z). \tag{4.1}$$

Aside from the magnitudes, the array $\boldsymbol{m}$ may include any other property of the observed galaxies, such as morphological type or ellipticity. The model $M_c(\boldsymbol{\theta} - \boldsymbol{\theta_c}, \boldsymbol{m}, z)$ describes the distribution of galaxies in a given cluster centered in $(\boldsymbol{\theta_c}, z_c)$, while $A(\boldsymbol{\theta_c}, z_c)$ is the normalization of the galaxy distribution of a detection, also called *amplitude*, and $N(\boldsymbol{m}, z)$ is the noise component associated to the distribution of the field galaxies.

In line with the theory of Optimal Filtering, the amplitude A is obtained by filtering the data D with an optimal filter Ψ_c

$$A(\boldsymbol{\theta_c}, z_c) = \alpha^{-1}(z_c) \int \Psi_c(\boldsymbol{\theta} - \boldsymbol{\theta_c}, \boldsymbol{m}, z) D(\boldsymbol{\theta}, \boldsymbol{m}, z)\, d^2\theta\, d^n m\, dz - B(z_c), \tag{4.2}$$

where α is a normalization constant, B is the background component and n is the number of dimensions of the array $\boldsymbol{m}$. Under the assumption that the noise is uniform and is produced by random Poissonian counts of galaxies, the filter Ψ_c is the ratio between model and noise:

$$\Psi_c(\boldsymbol{\theta} - \boldsymbol{\theta_c}, \boldsymbol{m}, z) = \frac{M_c(\boldsymbol{\theta} - \boldsymbol{\theta_c}, \boldsymbol{m}, z)}{N(\boldsymbol{m}, z_c)}. \tag{4.3}$$

Given a value of the amplitude A for each angular position and redshift, the first galaxy cluster candidate lies in the location with the largest likelihood and positive amplitude:

$$\mathcal{L}(\boldsymbol{\theta_c}, z_c) = \mathcal{L}_0 + A^2(\boldsymbol{\theta_c}, z_c)\, \alpha(z_c), \tag{4.4}$$

where $\mathcal{L}_0$ is a constant of no relevance. Maxima of the amplitude are also maxima of the likelihood at a given redshift, because when the cluster model

is centered in correspondence of a massive cluster, the likelihood has a bigger improvement compared to the case of a faint galaxy cluster.

Given the detection of a cluster j, the membership probability $P_i(j)$ of the i-th galaxy in the region is:

$$P_i(j) = P_{f,i} \frac{A_j M_j(\boldsymbol{\theta}_i - \boldsymbol{\theta}_j, \boldsymbol{m}_i)\, p_i(z_j)}{A_j M_j(\boldsymbol{\theta}_i - \boldsymbol{\theta}_j, \boldsymbol{m}_i)\, p_i(z_j) + N(\boldsymbol{m}_i, z_j)}. \tag{4.5}$$

$P_{f,i}$ is the probability of the galaxy to belong to the field, defined as

$$P_{f,i} \equiv 1 - \sum_j P_i(j). \tag{4.6}$$

This definition takes into account the fact that galaxies may be associated to different clusters, due to superimposition of detections along the line of sight.

After the evaluation of these probabilities for all the galaxies considered, in order to identify a new galaxy cluster the contribution of the last detection is removed from the amplitude map, and the likelihood is computed again. This removal is based on the membership probabilities $P_i(j)$, and is fundamental to retrieve objects blended with those with larger amplitudes.

4.1.2 The cluster model

The model M_c describes the expected galaxy distribution in a galaxy cluster. It is a function of the distance from the centre, $r = |\boldsymbol{\theta}_i - \boldsymbol{\theta}_c|$, and the magnitude $\boldsymbol{m}$ in the r band, given the redshift z_c. In particular, the model in this framework is defined as

$$M_c(r, \boldsymbol{m}) = \sum_i \Psi_i(r)\Phi_i(\boldsymbol{m}), \tag{4.7}$$

where the index i is referred to the member galaxies, Φ is a luminosity function and Ψ a radial profile.

The luminosity function considered here follows the Schechter profile (Schechter, 1976):

$$\Phi(m) = 10^{-0.4\,(m-m^*)\,(\beta+1)} \exp\left[-10^{-0.4\,(m-m^*)}\right]. \tag{4.8}$$

Only the functional form of the distribution is considered, because the normalization is absorbed by the constants during the filter construction. The quantity m^* is the typical magnitude, a function of redshift, derived from a stellar population evolutionary model with a faint-end slope β. The central galaxies are modelled instead by a Gaussian distribution in magnitude.

For the radial profile, a Navarro-Frenk-White profile is assumed (NFW; Navarro et al. 1997)

$$\Psi(r) = \frac{C_0}{r/r_s\,(1 + r/r_s)^2}, \tag{4.9}$$

where C_0 is a normalization parameter. The scale radius r_s is defined as

$$r_s \equiv R_{200}/c_{200}, \tag{4.10}$$

where c is the concentration parameter and R_{200} corresponds to a cluster mass $M_{200} = 10^{14}\, M_\odot/h$.

4.2 The AMICO KiDS-DR3 catalogue

The measured galaxy cluster mass function considered in this study is based on a real catalogue of galaxy clusters (M. Maturi et al. 2018) built up through the use of the AMICO algorithm.

As described in Section 4.1, AMICO is based on the Optimal Filtering technique applied on photometric data, in order to detect the overdensities in a distribution of galaxies and identify galaxy clusters. In particular, the detection process adopted for this study relies solely on spatial coordinates, magnitude and photo-z of galaxies. The use of the colors and, in turn, of the red-sequence has been avoided in order to make this work consistent with the future surveys beyond $z = 1$, such as the Euclid mission (Laureijs et al. 2011). At high redshifts, indeed, the knowledge of the appearance of galaxy clusters is limited, along with the knowledge of their physical properties. Therefore it is better to avoid the detection algorithms based on the red-sequence, in view of the future surveys.

The galaxy catalogue this work is based on comes from the Kilo Degree Survey Data Release 3 (KiDS-DR3; de Jong et al. 2017), therefore the catalogue of galaxy clusters is also referred as AMICO KiDS-DR3 catalogue. These galaxies have been detected with the OmegaCAM wide-field imager (Kuijken, 2011) mounted at the VLT Survey Telescope, a 2.6 m telescope sited at the Paranal Observatory (Capaccioli & Schipani, 2011). OmegaCAM offers a field of view of 1 deg^2 with a resolution of 0.21 arcsec/pixel, counting a total of 32 science CCDs. In particular are provided the 2 arcsec aperture photometry in u, g, r, i bands and photometric redshifts for all galaxies down to the 5σ limiting magnitudes of 24.3, 25.1, 24.9 and 23.8 for the four bands, respectively. For the final galaxy cluster catalogue, only the galaxies with magnitude $r < 24$ have been selected, for a total of 32 million objects.

The survey covers an area of 438 deg^2 but all the galaxies falling in regions affected by image artifacts, or falling in the masks used for the weak lensing analysis (described in Section 4.2.2), have been rejected. This yields a final effective area of 377 deg^2, the 86% of the total area of the survey. The final catalogue of galaxy clusters contains all the detections with a signal-to-noise ratio $S/N > 3.5$, for a total of 7988 candidate galaxy clusters in the redshift range $z \in [0.1, 0.8]$.

In particular, the photo-z of the galaxies has been obtained through a Bayesian template-fitting method, which yields a posterior probability exploited by AMICO

to determine the cluster redshifts. In Fig. 4.1 is shown the distribution of the objects of the final catalogue, and in particular the redshifts in the figure, as all the redshifts used in the analysis, have been corrected by a value $0.02\,(1+z)$:

$$z_{corrected} = z - 0.02\,(1+z). \tag{4.11}$$

The whole redshift interval, indeed, shows a constant relative scatter in redshift that amounts to $\Delta z/(1+z) \sim 0.02$, corresponding to what was found by de Jong et al. (2017) when comparing KiDS photo-zs with GAMA spec-z (Driver et al. 2009, 2011; Liske et al. 2015). In Fig. 4.2 is also shown the difference in the galaxy cluster distribution with and without the redshift correction. Moreover, there is a drop in the number of detections at $z \simeq 0.38$ due to problems related to the shape of the g and r filters, which imply a not optimal covering of the 4000 Å break at that redshift.

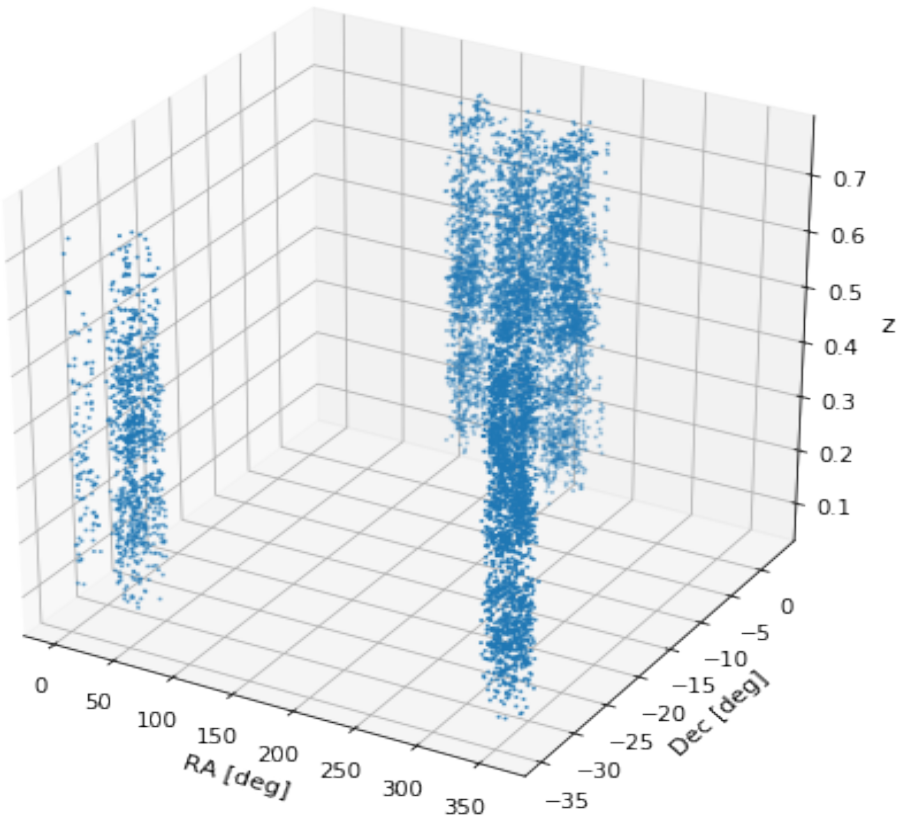

Figure 4.1: RA, Dec, z distribution of the galaxy clusters of the catalogue. The redshifts are corrected for the relative scatter $\Delta z/(1+z) \sim 0.02$.

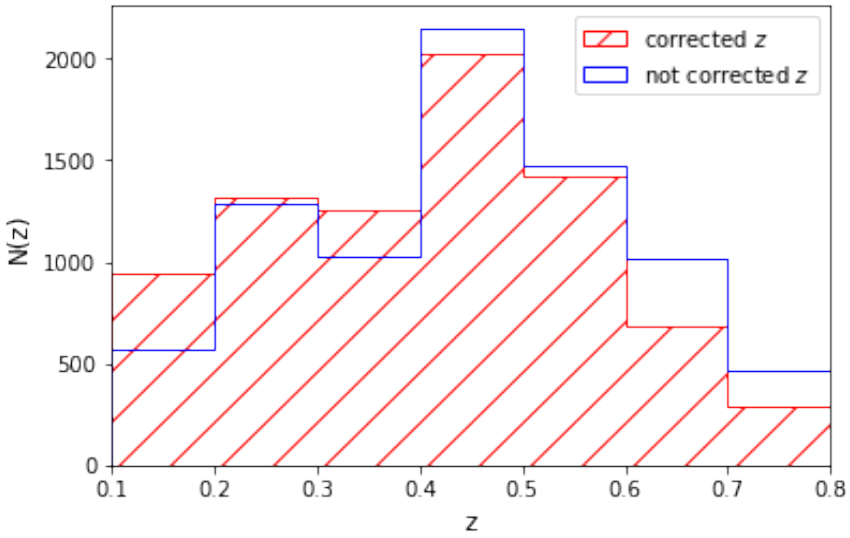

Figure 4.2: Distribution of the objects as a function of redshift. In particular are shown the cases of not corrected redshifts, and redshifts corrected for the constant relative scatter $\Delta z/(1+z) \sim 0.02$.

4.2.1 Mass proxies

In order to undertake a study based on the observed galaxy cluster mass function, it is necessary to have suitable proxies to obtain the values of the masses. Given the mass proxies described in this section, the masses have been obtained via a stacked weak lensing analysis presented in F. Bellagamba et al. 2019.

AMICO provides a natural mass proxy, the signal amplitude A defined in Eq. (4.2), which is also the first observable of the algorithm. It is a measure of the galaxy content in a detected cluster in units of the input model.

A second mass proxy is the intrinsic richness λ^*:

$$\lambda_j^* = \sum_{i=1}^{N_{gal}} P_i(j) \quad \text{with} \quad \begin{cases} m_i < m^*(z_j) + 1.5 \\ R_i(j) < R_{200}(z_j) \end{cases} \tag{4.12}$$

The radius R_{200} and the magnitude m^*, as discussed below in Section 4.1.2, are two parameters of the model adopted for the clusters, while z_j is the redshift of the detected cluster (labeled as j). $P_i(j)$ is the probability, assigned by AMICO, that the i-th galaxy is a member of a given detection j, Eq. (4.5). The intrinsic richness represents the sum of the membership probabilities, i.e. the number of visible galaxies belonging to a detection, under the shown conditions.

The sum of the membership probabilities, indeed, is a good expression of the total number of member galaxies, as described in F. Bellagamba et al. 2017, (see Fig. 8 in the reference). In particular, by running AMICO on mock catalogues, it has been shown that if the cluster model is a good representation of the mean

properties of the data, there is a tight relation between the probabilistic association of member galaxies and the fraction of members that actually belong to the identified cluster.

Furthermore we can define the more general apparent richness λ

$$\lambda_j = \sum_{i=1}^{N_{gal}} P_i(j). \tag{4.13}$$

However this quantity has a severe dependence on redshift, and for this reason it can not be exploited as a mass proxy. As the redshift increases, indeed, the faintest member galaxies will overcome the limiting magnitude of the survey. This is not the case for λ^*, given that the threshold $m^* + 1.5$ is below the magnitude limit for the galaxies in the sample, for the whole redshift range considered in this analysis. Therefore λ^* is nearly redshift independent and for this reason it is a suitable mass proxy.

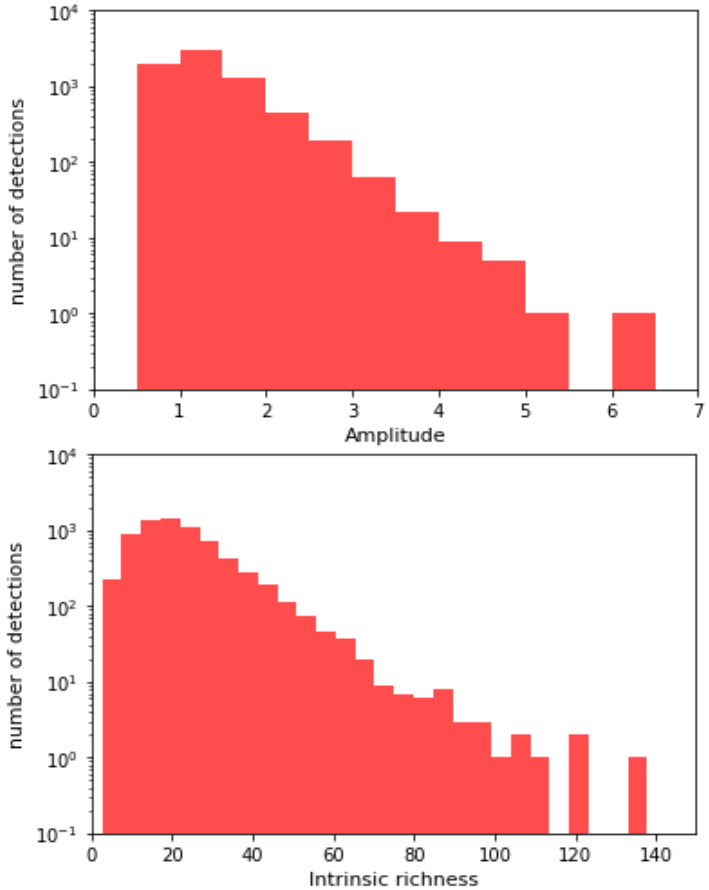

Figure 4.3: Amplitude and intrinsic richness distributions for the clusters selected to carry out the weak lensing analysis. The redshift range is $0.1 \leq z < 0.6$, for a total of 6962 objects.

In Fig. 4.3 are shown the distributions of A and λ^*, in the redshift range $0.1 \leq z < 0.6$, for the clusters selected for the weak lensing analysis. As the selection is performed with a S/N threshold, the amplitude and intrinsic richness thresholds are not constant in redshift. This produces the increase in cluster counts from the first bins to the subsequent ones.

In Fig. 4.4 is instead shown the correlation between amplitude and intrinsic richness.

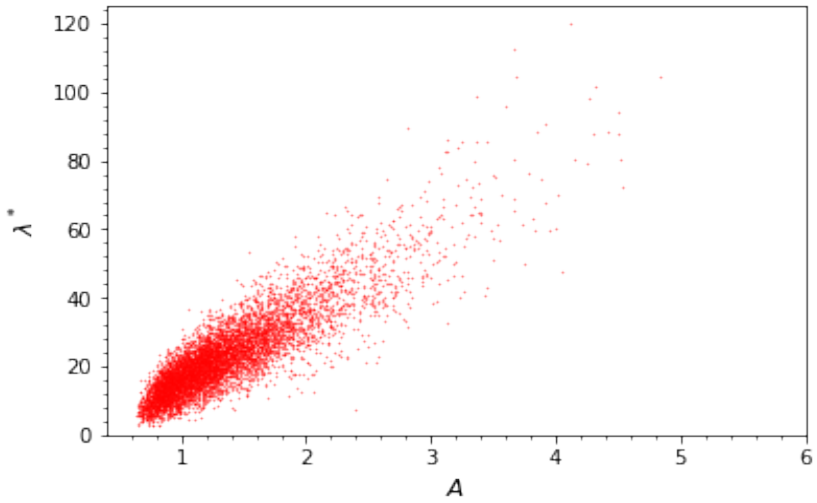

Figure 4.4: Correlation between amplitude A and intrinsic richness λ^* in the redshift range $0.1 \leq z < 0.6$.

4.2.2 Weak-lensing mass calibration

Weak gravitational lensing in photometric datasets is a crucial tool to estimate the masses of galaxy clusters. Through the distortion of the images of background sources, gravitational lensing provides a measure of the total matter distribution in the cluster. Moreover, the mass estimated through this method is independent of any assumption on the physical state of the cluster, differently from methods dependent on the gas properties such as X-ray observations and Sunyaev-Zel'dovich effect on the CMB.

As explained in F. Bellagamba et al. 2019, the analysis is based on the study of the shear profile of background sources. A flat ΛCDM cosmology is considered, with $H_0 = 70\,\mathrm{km/s/Mpc}$ and $\Omega_m = 0.3$.

In a first instance, it is necessary to avoid the contributions of foreground sources and galaxies belonging to the clusters that could be considered as background. Those contributions, indeed, would produce a dilution of the signal.

In order to retrieve only the lensing signal from the background sources, first of all has been carried out a photo-z selection. Only the galaxies with $z_s > z_l + \Delta z$

have been considered, where z_s is the photometric redshift of the galaxy, z_l is the redshift of the lens and Δz is set to 0.05, similar to the typical error on photometric redshifts in the galaxy catalogue. With this approach have been excluded all the galaxies with non-negligible probability to have a redshift equal or lower to the one of the lens.

A second criterion is the color selection, aimed to recover part of the population of galaxies behind the clusters excluded through the previous method. The photo-z selection, indeed, excludes a large part of background candidates. In particular the effectuated cut follows the selection performed by Medezinski et al. (2017):

$$(g - r < 0.3) \vee (r - i > 1.3) \vee (r - i > g - r). \tag{4.14}$$

At the conclusion of this selection, it is obtained the shear signal in the tangential direction with respect to the center of the cluster. In particular the shear γ is not an observable, indeed what is measured is the reduced shear $g = \gamma/(1-k)$, where k is the convergence defined as

$$k = \frac{\Sigma}{\Sigma_{crit}}. \tag{4.15}$$

Σ is the surface density of the lens, while Σ_{crit} is the critical density:

$$\Sigma_{crit} = \frac{c^2}{4\pi G}\frac{D_s}{D_l D_{ls}}\ , \tag{4.16}$$

where D_s, D_l and D_{ls} are, respectively, the angular diameter distance between observer and source, observer and lens, and lens and source. In the case of $\Sigma > \Sigma_{crit}$, we face the case of gravitational lensing. In the case of this study, however, the regime is that of the weak-lensing[1], and this implies $k << 1$, which allows to estimate the shear from g because $\gamma \sim g$.

Consequently it can be constructed the observed differential surface profile of the lens $\Delta\Sigma$

$$\Delta\Sigma(R) = \Sigma_{crit}\gamma_+, \tag{4.17}$$

where γ_+ is the tangential component of the shear. However, for the greater part of the clusters the signal-to-noise ratio of the lensing data is low, so the density profile is constrained through a stacking procedure. It consists of an estimate of the mean lens mass of objects grouped in bins, according to their amplitude A or intrinsic richness λ^*, and their redshifts. In particular the redshift bins considered in the analysis are $0.1 \leq z < 0.3$, $0.3 \leq z < 0.45$, $0.45 \leq z < 0.6$. Objects with $z \geq 0.6$ have been discarded because the density of background galaxies does not allow a robust lensing analysis.

[1]Strong gravitational lensing requires very specific alignment conditions.

Extracting the stacked shear profile from each bin can be derived an estimate of the mass, by assuming for the lens a smoothly-truncated NFW model plus a 2-halo term, taking into account uncertainties related to concentration and miscentering.

The obtained mass-observable relation is then:

$$\log \frac{M_{200}}{10^{14} M_{\odot}/h} = \alpha + \beta \log \frac{O}{O_{piv}} + \gamma \log \frac{E(z)}{E(z_{piv})} \ , \tag{4.18}$$

where $E(z) = H(z)/H_0$ and the term $\gamma \log E(z)$ accounts for the redshift evolution. The quantities O_{piv} and z_{piv} represent the typical values of observable and redshift of the total sample, respectively. As we shall see, the only mass proxy of interest in the analysis carried out in this Thesis work is the intrinsic richness, λ^*, therefore we provide the parameters of the scaling relation for this case:

$$\begin{cases} \alpha = 0.004 \pm 0.038 \\ \beta = 1.71 \pm 0.08 \\ \gamma = -1.33 \pm 0.64 \\ \lambda^*_{piv} = 30 \\ z_{piv} = 0.35 \end{cases} \tag{4.19}$$

It is important to stress that the mass-observable scaling relation is calibrated only for the redshift ranges $0.1 \leq z < 0.3$, $0.3 \leq z < 0.45$, $0.45 \leq z < 0.6$, while for $0.6 \leq z < 0.8$ this relation is extrapolated. In the analysis described in Chapter 5, the cosmological parameters will be constrained by neglecting this last redshift bin.

4.3 The mock catalogue

In addition to the high number of objects in the galaxy cluster catalogue and the wide redshift range, the strength of the dataset used in this work lies in the availability of a model-independent selection function, obtained through the realization of a catalogue of mock clusters based on the properties of the KiDS-DR3 data itself (M. Maturi et al. 2018). Moreover, this mock catalogue allows to estimate the uncertainties of the main quantities characterizing the detected clusters.

Basing the construction of the mock clusters on the original galaxy dataset, all the properties of the survey are taken into account, such as absorption, photo-z uncertainties and clustering of the galaxies, and in addition in this way are minimized the assumptions necessary to build up the mock catalogue.

4.3.1 Description

The method used to build up the mock catalogue exploits the probabilities of the galaxies of being associated to the field $P_{f,i}$, Eq (4.6), or being members of a cluster $P_i(j)$, Eq. (4.5), computed by AMICO.

The subsequent step is a Monte Carlo extraction of the mock field galaxies, based on their probability of being member of the field, $P_{f,i}$. In particular, a uniform Monte Carlo extraction of a number n_i between 0 and 1 is performed, and then the i-th galaxy is assigned to the field if $n_i < P_{f,i}$.

To retrieve the mock clusters, in a first instance have been defined bins of apparent richness λ, which is the number of visible galaxies for a given cluster, and redshift z, in order to collect the galaxies with membership probability $P_i(j) > 0$. Those galaxies with a probability to belong to more than one cluster have been attributed to more than one bin accordingly. Then every bin of λ and z contains all the potential member galaxies associated to the bin itself. Mock clusters are then generated through a Monte Carlo extraction of galaxies in the corresponding bins via a Monte Carlo sampling, based on their probability $P_i(j)$ and accounting for the presence of masked areas in the actual survey.

The mock clusters are then placed into the field with the same angular positions, λ and z of the detected clusters with $S/N \geq 3.0$ found in the original catalogue. This preserves the correlation of clusters with clusters and of clusters with the Large Scale Structure, and also allows to take into account missing data, absorption, blending and photometric uncertainties. In addition, the difference between the signal-to-noise ratio considered here and the one considered for the final cluster catalogue, $S/N > 3.5$, is essential to derive reliable statistical properties for the sample.

The final mock catalogue contains 9018 mock clusters, over a total area of $189\,\mathrm{deg}^2$. In order to derive the selection function and the uncertainties of the dataset, the AMICO code has been run on the mock catalogue. The uncertainties on the detection properties are already considered in the final galaxy cluster catalogue used for this study.

In general the richness (λ and λ^*) is unbiased at all redshifts, as well as the redshift assignation carried out by AMICO. Of a particular relevance, instead, is the bias on the amplitude at $z < 0.3$ shown in Fig. 4.5. As a consequence, we will base the analysis discussed in Chapter 5 only on the intrinsic richness λ^*, which covers the range $\lambda^* \in [2.78, 136.73]$.

The other fundamental output of this procedure based on mock clusters is the evaluation of the selection function, i.e. the completeness and the purity of the dataset. The computation and application of completeness and purity will be detailed in Chapter 5.

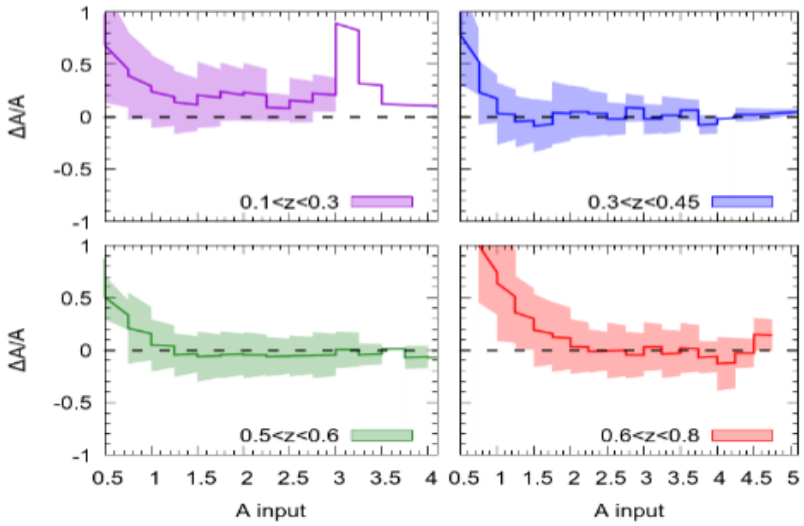

Figure 4.5: Relative 1σ errors on the amplitude A. A clear bias shows up in the first redshift bin.

Chapter 5

Cosmological constraints from the number counts of the AMICO KiDS-DR3 catalogue

In this chapter we will present the analysis employed to derive constraints on the cosmological parameters Ω_m, σ_8 and S_8, from cluster counts in the AMICO KiDS-DR3 catalogue. We will focus in a first instance on the computational tools and the theory at the basis of this work. Then we will present the methods used to apply the selection function to the sample. Subsequently, we will present the two cosmological pipelines developed in order to derive constraints on the cosmological parameters, finally focusing on the effects of the super sample covariance on our results.

5.1 General approach

The whole analysis carried out in this Thesis work can be summarized as follows. The starting point is the set of observed values of redshift, z, and intrinsic richness, λ^*, namely $\{z_{obs,i}, \lambda^*_{obs,i}\}$, provided by the AMICO KiDS-DR3 galaxy cluster catalogue. We will present two different pipelines through which we will derive constraints on the cosmological parameters Ω_m, σ_8 and S_8, by performing the analysis on cluster counts in the aforementioned catalogue.

In the first pipeline, *Pipeline I*, from the set of data we compute the mass, M, of each galaxy cluster, through the proxy-mass scaling relation (Eq. 4.18) which is calibrated on the observed values of z and λ^*. The uncertainties on the scaling relation are parametrized in terms of the uncertainties in the parameters α, β and γ, and are considered in the analysis by means of Monte Carlo extractions. The uncertainties on photometric redshifts and intrinsic richnesses have to be considered as well, by extracting random values from the probability distributions retrieved in the catalogue of mock clusters described in Section 4.3. Finally, the

selection function of the sample is taken into account by assigning the appropriate weights w to the objects. The final set of data includes the redshift values obtained from the relative probability distributions, along with the masses and the weights: $\{z_i, M_i, w_i\}$.

The second pipeline, *Pipeline II*, consists in accounting for the uncertainties on the data by weighting appropriately the assumed theoretical model. This becomes possible by including in the model the uncertainty on the scaling relation and on the photometric redshifts, by means of Gaussian probability distributions. Therefore in this case the final set of data comprises the observed redshifts and richnesses, along with the weights: $\{z_{obs,i}, \lambda^*_{obs,i}, w_i\}$. In turn, we avoid Monte Carlo extractions and we improve the reliability of the analysis, since we do not assume any cosmological model in order to obtain the values of the masses.

The first cosmological analysis we perform on the data concerns the computation and modelling of the number counts as a function of M, namely $N(M)$, and as a function of λ^*, that is $N(\lambda^*)$, for different redshift bins. Additionally, we consider the whole dataset simultaneously, modelling $N(z, M)$ and $N(z, \lambda^*)$. In this way we obtain constraints on the matter density parameter Ω_m, the power spectrum normalization σ_8, and the derived parameter $S_8 \equiv \sigma_8(\Omega_m/0.3)^{0.5}$.

In presenting our results, we take as a reference the constraints on Ω_m, σ_8 and S_8 obtained by:

- Planck Collab. (2018) (Table 2, TT,TE,EE+lowE+lensing), the most reliable parametrization of our Universe, based on the observations of the cosmic microwave radiation (CMB) carried out with the Planck satellite;
- Hinshaw et al. (2013) (Table 3, WMAP-only Nine-year), the results based on the observations of the CMB with the WMAP probe;
- Costanzi et al. (2018), a recent work on galaxy cluster counts in a photometric catalogue based on data from the Sloan Digital Sky Survey.

We will recall these references, respectively, as Planck18, WMAP9 and Costanzi18, both in the figures and in the text, for the sake of brevity. In the first two cases, the constraints are nearly statistically independent from those retrieved in this Thesis work. Indeed they are based on observations of the cosmic microwave background, the radiation coming from the primordial Universe. On the other hand, we account also for the work carried out by Costanzi18 in order to have a comparison with a similar analysis on counts of galaxy clusters.

5.2 Models and computational tools

In this section we outline the fundamental steps of the cosmological analysis undertaken in this Thesis work. The used models and computational tools are implemented in the CosmoBolognaLib (Marulli et al. 2016), a large set of C++/Python libraries, that provide an efficient numerical environment for cosmological investigations of the large-scale structure of the Universe. In particular, we developed methods to manage the selection function (Section 5.3), and we implemented the model for the expectation values of the counts described in Section 5.2.1, along with the codes used to account for the super sample covariance at the likelihood level (Section 5.10).

5.2.1 The model for cluster number counts

The theoretical mass function model at the base of this analysis is the Tinker halo mass function (Tinker et al. 2008), which can be expressed in the general form given in Eq. (3.23), with multiplicity function $f(\sigma_M, z)$ having the following functional form:

$$f(\sigma_M, z) = A \left[\left(\frac{\sigma_M}{b} \right)^{-a} + 1 \right] e^{-c/\sigma_M^2}, \tag{5.1}$$

where σ_M^2 is the filtered mass variance, Eq. (1.152). The quantity A is the overall amplitude of the mass function, a and b set the slope and the amplitude of the low-mass power law, respectively, while c determines the cut-off scale where the abundance of haloes exponentially decreases. These parameters, along with σ_M, contain also the dependence on redshift.

The Tinker mass function is accurate to better than 5% for the cosmologies close to the ΛCDM model and for the mass and redshift range of interest in this study. Moreover, the advantage of this choice lies in the wide use of this theoretical mass function in the literature. This allows a more consistent comparison of our results with those obtained in other works on the observed galaxy cluster mass function.

In particular, according to the assumptions in the lensing analysis described in the previous chapter, M_{200} halo masses are considered in the computation of the mass function models. These values are referred to the mass enclosed in a radius r_{200}, where the mean density is 200 times the critical density of the Universe at the corresponding redshift. A further consideration, valid for the entire cosmological investigation carried out in this Thesis, is that we developed an analysis based on number counts instead of mass function. In fact, working with the mass function implies the assumption of a cosmological model on the data itself, because of the normalization to mass and volume (see Eq. 3.23). Additionally, dealing with the observed counts of galaxy clusters we need to consider a range of redshift, and

consequently the mass function must be integrated on this quantity. Then the final functional form of the model is:

$$N(\Delta M, \Delta z_{obs}) = \Omega_{eff} \int_{\Delta M} \int_{\Delta z_{obs}} \frac{\mathrm{d}n(M, z_{obs})}{\mathrm{d}M} \frac{\mathrm{d}^2 V}{\mathrm{d}z_{obs}\mathrm{d}\Omega}(z_{obs}) \; \mathrm{d}M\mathrm{d}z_{obs}, \tag{5.2}$$

where Δz_{obs} is the observed redshift range, $\mathrm{d}^2V/(\mathrm{d}z\mathrm{d}\Omega)$ is the comoving volume element per unit redshift and solid angle, and Ω_{eff} is the effective area of the survey. To compute the power spectrum $P(k)$, and thus the mass variance σ_M, the algorithm provided by Eisenstein and Hu has been used for the mass function.[1]

5.2.2 The likelihood function

Given the mass function model (Eq. 5.2) and the assumption of a base cosmology, the cornerstone of our analysis is the Bayesian approach. In particular, given the model with a set of free parameters $\boldsymbol{\theta} = (\theta_1, \ldots, \theta_p)$, the aim is to obtain the marginalized posterior of these parameters.

Specifically, in a first instance we set the priors for the free parameters of the model, that is Ω_m and σ_8 in our case. Then a functional form for the likelihood $\mathcal{L}$ is chosen, which in this kind of this studies is in general a Poissonian likelihood, here expressed as a logarithm:

$$\ln \mathcal{L}(x_1, \ldots, x_n \,|\, \mu_1, \ldots, \mu_n) = \sum_{i=1}^{n} \ln(\mu_i)\, x_i - \sum_{i=1}^{n} \mu_i - \sum_{i} \ln(x_i!), \tag{5.3}$$

where x_i represents the datapoints, while μ_i is the model computed in correspondence of the bins in which the data are collected. The free parameters $(\theta_1, \ldots, \theta_p)$ are implicitly contained in the model.

In two dimensions, as for the case of $N(M)$, the Poissonian log-likelihood is the following:

$$\begin{aligned} \ln \mathcal{L}(x_{11}, \ldots, x_{mn} \,|\, \mu_{11}, \ldots, \mu_{mn}) = &\sum_{j=1}^{m} \sum_{i=1}^{n} \ln(\mu_{ij})\, x_{ij} - \sum_{j=1}^{m} \sum_{i=1}^{n} \mu_{ij} - \\ &- \sum_{j=1}^{m} \sum_{i=1}^{n} \ln(x_{ij}!). \end{aligned} \tag{5.4}$$

As we shall see, we will make use also of the Gaussian likelihood, expressed in general as the natural logarithm of a multivariate Gaussian. Moreover we will also exploit a convolution of Poissonian and Gaussian. Given the expression for $\mathcal{L}$, the analysis proceeds with the sampling of the posterior, via a Markov chain Monte Carlo (MCMC) algorithm.

[1] http://background.uchicago.edu/~whu/transfer/transferpage.html

5.2.3 Markov chain Monte Carlo

The MCMC has a central role in cosmology and astrophysics. It is indeed fundamental when the physical model has several free parameters and the posterior does not have an analytic expression.

Given the $\boldsymbol{\theta}$ free parameters of the model, the general goal of MCMC algorithms is to draw a given number n of samples $\{\theta_i\}$, with $i = 1, \ldots, n$, from the posterior probability density $P(\boldsymbol{\theta} \,|\, D)$, which is expressed as follows:

$$P(\boldsymbol{\theta} \,|\, D) = \frac{1}{P(D)} P(D \,|\, \boldsymbol{\theta}) P(\boldsymbol{\theta}). \tag{5.5}$$

This equation represents the most common notation used for the Bayes' theorem. Here $P(D \,|\, \boldsymbol{\theta})$ represents the likelihood and $P(\boldsymbol{\theta})$ is the prior, while $P(D)$ is the *evidence*, which can be neglected once the form of the generative model is chosen.

After obtaining the samples, the mean parameter values, $\bar{\boldsymbol{\theta}}$, of the posterior, along with their uncertainties, can be retrieved from the histogram of the samples projected onto the relative parameter subspace. In Fig. 5.1 we show a typical output of the MCMC for this analysis: both the confidence contours and the histograms of the marginalized posteriors are fundamental tools for the evaluation of the results.

There are different algorithms that can be implemented to compute the chains. The general idea is that of generating random walks in the parameter space that, over time, draw a representative set of samples from the distribution of the posterior. Each point in the chain $X(t_i) = \theta_i$ depends only on the position of the previous step $X(t_{i-1})$. The analysis carried out in this work exploits the *stretch move* sampling algorithm (Goodman & Weare, 2010).

In our procedure the chains are initialized, in the parameter space, in volumes of a given radius around the posterior best-fit parameter values, i.e. the values obtained from the posterior maximization. This implies a shorter time for the convergence of the algorithm. Furthermore, we assume flat priors for the free parameters in order to not privilege any value. These priors are $\Omega_m \in [0.5, 1]$ and $\sigma_8 \in [0.1, 2]$.

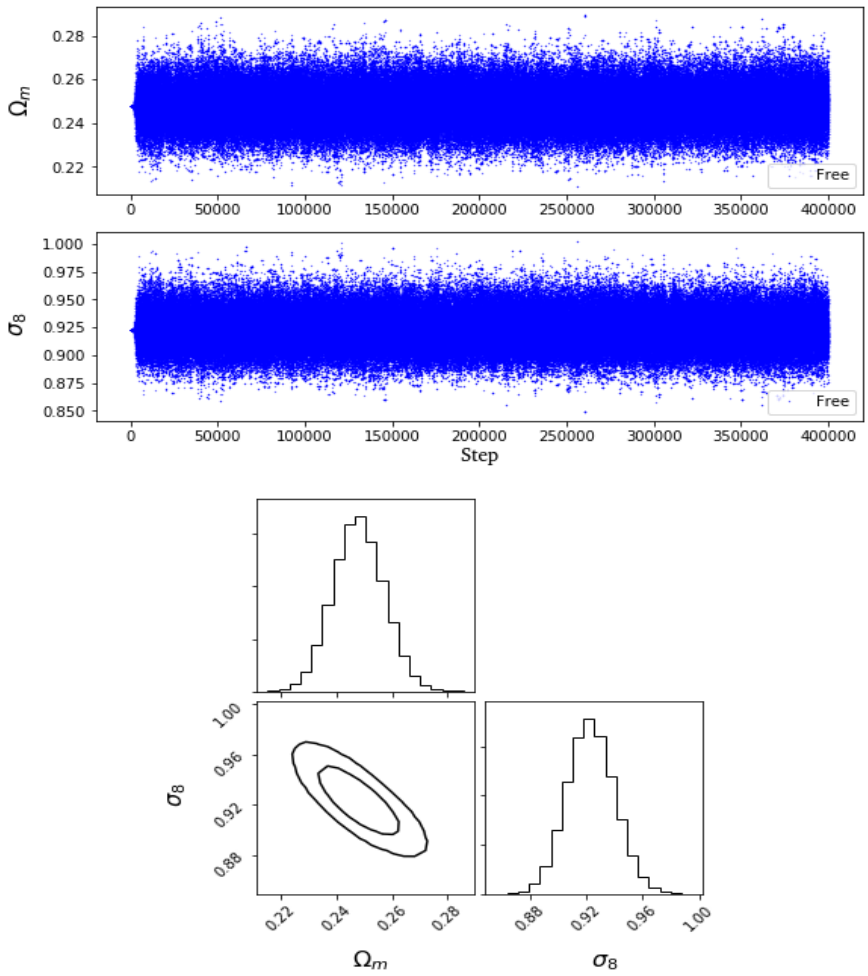

Figure 5.1: Visualization of a typical output of the MCMC algorithm. The steps of the process are shown in the top panel, referred to the free values of the model (in this case, Ω_m and σ_8). It is very important that the chains do not get stuck in correspondence of the extreme values of the priors, thus a good choice of these extreme values is mandatory. The histograms of the marginalized values of the parameters are shown in the bottom panel, along with the confidence contours at 68% and 95%. If the chains do not show problems, as in the case in this figure, the histograms show a single mode, allowing the computation of mean and percentiles of the distribution obtained from the sampling.

5.3 Completeness and purity

The completeness and purity of the dataset define the *selection function*, an essential tool in mass function studies. Knowing how many objects are lost in the detection procedure, and how many are mistakenly identified as clusters, is indeed critically important. In our analysis these two quantities are computed by comparing the clusters detected with the AMICO code, run on the mock catalogue, to the mock clusters originally injected into the field. As discussed in Chapter 4, the mass proxy considered in the analysis is the intrinsic richness λ^*. The completeness and purity are based on this quantity. Specifically, the completeness is defined as the number of detections correctly identified as clusters over the total number of mock clusters, in a given bin of redshift and intrinsic richness. In other words, it provides a measure of how many objects are lost in the detection procedure. On the other hand, the purity is a measure of the contamination level of the cluster sample. It is defined as the fraction of detections that match with the mock clusters over the total number of detections, in a given bin of redshift and intrinsic richness.

To obtain a suitable binning for purity and completeness, we exploited the results of AMICO relative to the mock clusters, obtained by Maturi et al. (2018). In particular, the computation of purity and completeness relied on two datasets, one containing the properties of the mock clusters injected into the field and those of the detected ones, such as their redshifts, the values of intrinsic richness, their signal-to-noise, while the other dataset contains the properties of detected mock clusters and the relative match with the injected clusters, if any. From the former file we obtain the completeness, while from the latter the purity.

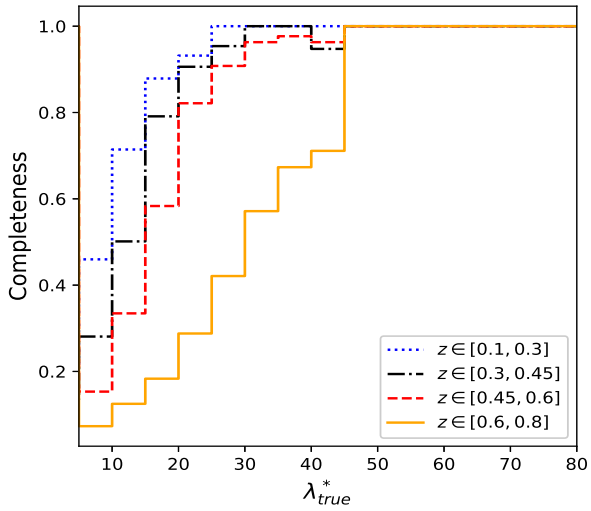

Figure 5.2: Completeness of the AMICO KiDS-DR3 cluster catalogue as a function of the redshift, z, and the intrinsic richness, λ^*.

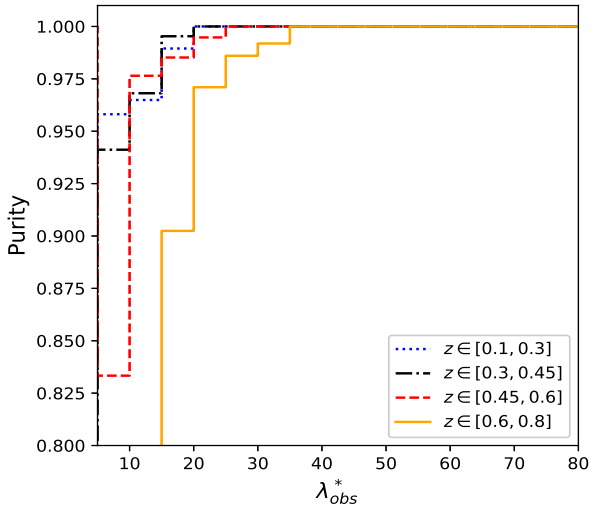

Figure 5.3: Purity of the AMICO KiDS-DR3 cluster catalogue as a function of the redshift, z, and the intrinsic richness λ^*.

Fig. 5.2 and 5.3 show the AMICO KiDS-DR3 completeness and purity, respectively, as functions of λ^* for different redshift ranges. It turns out that the catalogue is highly pure, with a purity approaching 90% over the whole redshift range. It is important to point out that both completeness and purity are computed as a function of the true redshift, as will be detailed in Section 5.6.

Since the completeness is a function of the true intrinsic richness, λ^*_{tr}, it is required to implement a method that assigns a value of completeness to an observed value of intrinsic richness.[2] For this purpose, two alternative methods have been developed, based on the observed and true values of λ^* of the mock clusters: the first method is based on cumulative probability distributions, while the second relies on a Gaussian fitting of the data for each bin of λ^*.

The method based on the cumulative probability distributions consists of the following steps:

- Among the results related to the mock clusters, only the detections with $S/N > 3.5$ are regarded, being this the threshold applied in the real dataset.

- Then we construct a matrix for which the rows are referred to the observed values of intrinsic richnesses, while the columns are related to their true values. In particular, rows and columns are relative to the central value of each bin, and a linear binning is considered. The bins for observed and true values are equal in number and spacing.

[2]Here, the term "observed" indicates the values relative to the detections accomplished by AMICO. It may refer to mock or real clusters. Differently, the term "true" is only referred to the observables of the mock clusters injected into the field.

- Each detection has a value of observed intrinsic richness λ^*_{obs}, which designates the row of the matrix, while the true λ^*_{true} of the corresponding mock cluster designates the column.

- In this way, for each bin of the observed intrinsic richness, different bins for the true values are filled.

- It is then necessary to normalize each bin in a row to the total number of objects in the row itself. This provides a cumulative probability distribution, that allows the assignation of a true bin to an observed one. In turn it is assigned a completeness value to each observed intrinsic richness.

With this matrix at hand, we consider the values of intrinsic richness of the real catalogue. Given the value of the observable for a real cluster, it is assigned to the relative bin, or row, in the matrix. Then we perform an extraction of a uniform random number, n, between 0 and 1. If the extracted random number n is greater than the probability value assigned to the first bin, i.e. the first column relative to the row, then the probability of the first and second columns are added up, and so on. The iterations stop when n is lower than the cumulative probability, computed for example from the first to the i-th bin. Then the observed value λ^*_{obs} will be assigned to the completeness value relative to the bin labeled as i. In turn, the relative object of the catalogue will be weighted in accordance with the value of completeness in that bin.

The second method, instead, is based on Gaussian probability distributions, retrieved also in this case from the mock catalogues. It follows the same steps of the previous one, from the setting of the threshold on the S/N to the construction of the matrix. However in this case, for each bin of observed values of intrinsic richness, the distribution of the true values is described through an appropriate Gaussian function. In particular, in a first instance a value of λ^*_{obs} in the real catalogue is assigned to the relative bin. Then a random Gaussian extraction is performed, based on the mean and standard deviation values of the Gaussian that describes the distribution of the true values in that bin. Fig. 5.4 shows a typical Gaussian probability distribution retrieved from the mock catalogue. It turns out that the two methods used to assign the values of completeness are statistically equivalent, producing results on the final number of counts consistent within $1\,\sigma$.

On the other hand, the purity is a function of the observed intrinsic richness, λ^*_{obs}, being strictly related to the quality of the observations. We assign each object in the real catalogue to a bin of observed intrinsic richness. Subsequently, we extract a uniform random number between 0 and 1, and if it is lower than the purity corresponding to the aforementioned bin, the object is considered in the analysis. Otherwise, it is rejected. In this way, the final sample will take into account the effects of impurities.

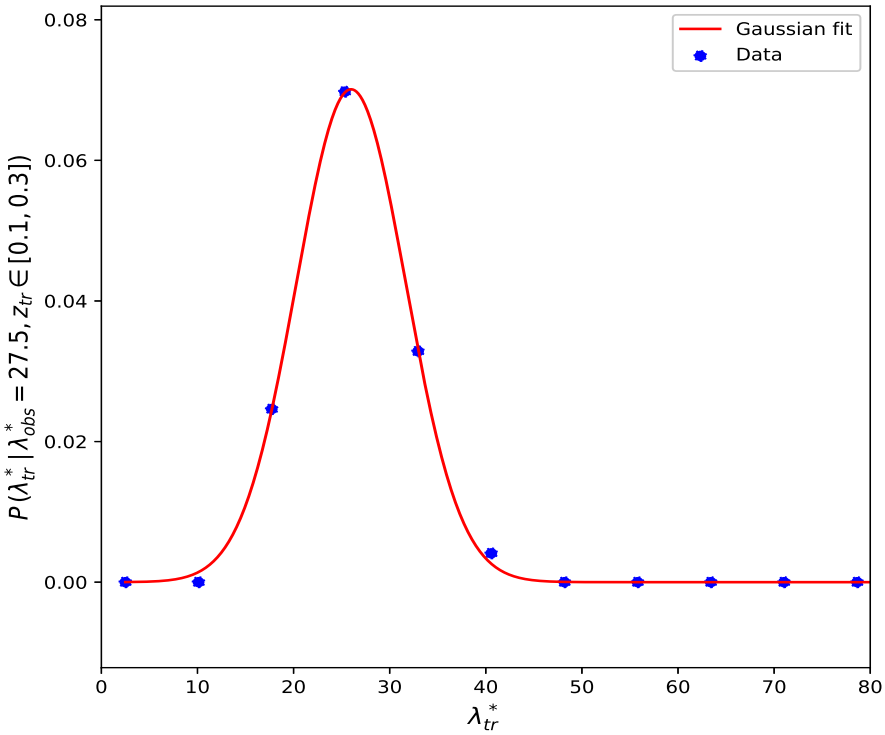

Figure 5.4: Probability distribution $P(\lambda^*_{tr}|\lambda^*_{obs}, z_{tr})$, in the case of a bin with a central value of the observed intrinsic richness equal to $\lambda^*_{obs} = 27.5$ and a true value of redshift in the range $0.1 \leq z_{tr} < 0.3$.

In Fig. 5.5 we show the number counts of AMICO KiDS-DR3 clusters, with and without weighting for purity and completeness. It is important to point out that the application of the selection function requires a preliminar treatment of the redshift uncertainties, as we shall detail in Section 5.6. We can appreciate how for low masses, about 10^{14} $M_\odot$ h^{-1}, the selection function weighting helps to improve the agreement with Planck18 predictions. At lower masses, however, the effects of the Malmquist bias, not included in our weighting corrections, introduce a systematic bias in the counts. As we shall see in the following, we will exclude this small mass range from our analysis, considering only the masses from $\sim 5{\cdot}10^{13}$ $M_\odot$ h^{-1} to $\sim 10^{15}$ $M_\odot$ h^{-1}.

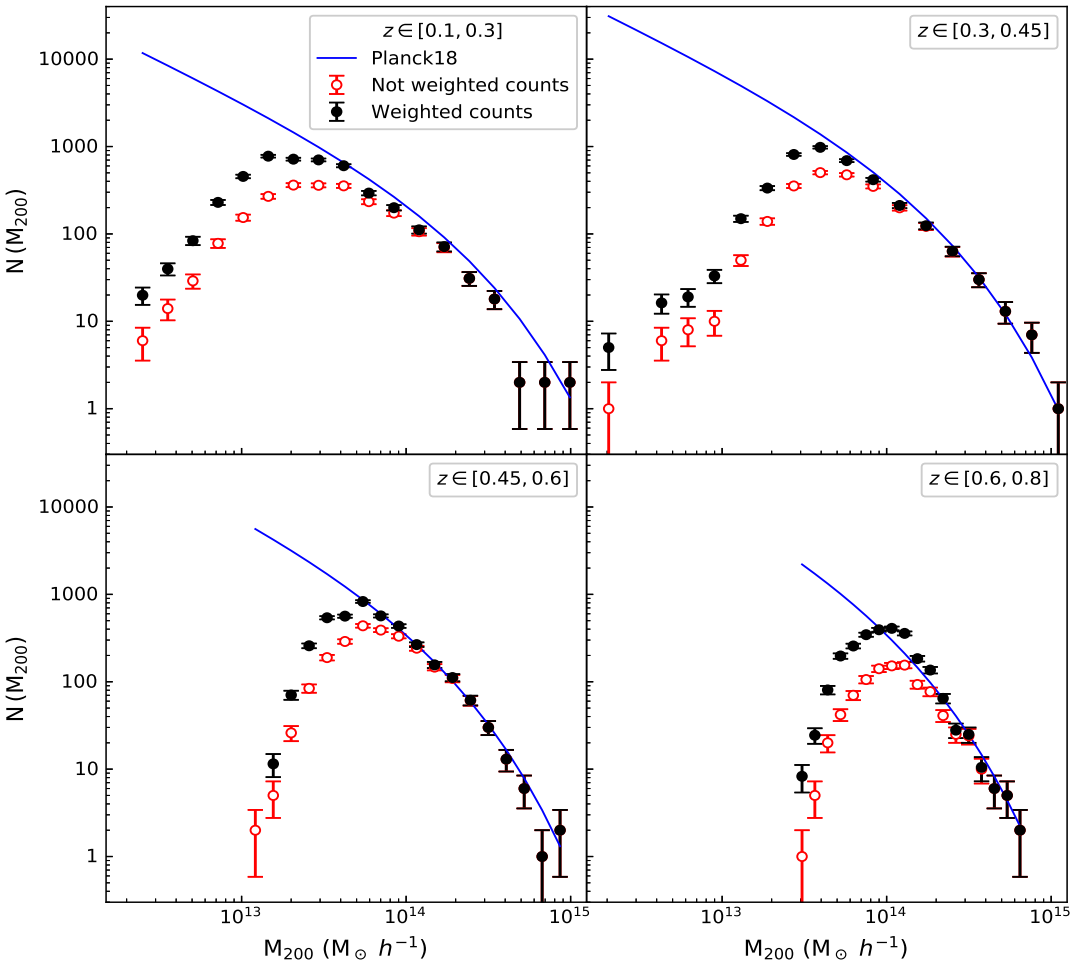

Figure 5.5: Effects of the selection function on the binned counts. The open red dots represent the counts directly retrieved from the AMICO KiDS-DR3 catalogue, while the black dots show the counts weighted for the completeness and statistically corrected for the impurity. The error bars represent the Poissonian error. As a reference, the number counts predicted in the ΛCDM model with parameters from Planck18 is shown (blue solid line), computed assuming the mass function Tinker et al. (2008).

5.4 Redshift selection

The AMICO KiDS-DR3 catalogue provides a large set of galaxy clusters over a large range of redshift, $z \in [0.1, 0.8]$, which allows us to retrieve constraints on cosmological parameters from a wide spectrum of epochs in the history of the Universe. Nevertheless, as discussed in Section 4, the observable-mass scaling relation is not calibrated in the redshift bin $z \in [0.6, 0.8]$. Therefore we exclude this part of the dataset from the analysis. This is not a dramatic loss in terms of the number of objects, since only the high mass regime can be considered in this redshift range, for a total of almost 100 objects. Indeed, as we can see in

Fig. 5.5, the selection function appears to be overestimated in the low mass range, assuming Planck18 expectations. Therefore the cosmological parameters derived by introducing these data in the modelling are critically biased.

Furthermore, as shown in Fig. 5.3, the detections in this redshift range are severely affected by impurity. Given all these considerations, we will base our analysis on the redshift ranges $z \in [0.1, 0.3]$, $[0.3, 0.45]$, $[0.45, 0.6]$.

5.5 Cosmological pipelines

In the analysis carried out in this Thesis, the treatment of the uncertainties plays a crucial role. Apart from the Poissonian errors assigned to the binned counts, the uncertainties on redshifts and on the observable-mass scaling relation must be taken into account. We developed two alternative pipelines in order to evaluate their effects. In the following sections we will focus on the first pipeline, while the second will be discussed in Section 5.8. As we shall see, aside from the evaluation of the uncertainties, the second pipeline differs from the first one also because it is based on counts as a function of the observable λ^*, instead of masses.

The first pipeline, which we will refer to as *Pipeline I*, exploits the model described in Section 5.2.1, i.e. the number counts as a function of the mass M (Eq. 5.2). In particular, the uncertainties on photometric redshifts and on the observable-mass scaling relation, are considered by means of Monte Carlo extractions, as we shall discuss in the following section.

5.6 Treatment of uncertainties in *Pipeline I*

In this section we will detail the methods used to account for the uncertainties in *Pipeline I*. As in the case of the selection function described in Section 5.3, the uncertainties on the data are evaluated through Monte Carlo extractions. In particular, we extract each quantity of every object in the catalogue n times, thus obtaining n realizations of every single galaxy cluster. Therefore we deal with a larger dataset, in which a weight $1/n$ is assigned to each object.

The first considered property is the cluster mass M. This value is retrieved from the observable-mass scaling relation which is calibrated, as already mentioned in Section 5.1, on the observed values of z and λ^*, and the uncertainties are parametrized in terms of the errors on the three parameters α, β, γ. For this reason, a Gaussian Monte Carlo extraction is performed for each of these parameters, with mean equal to the given value of α, β or γ, and standard deviation equal to the error in the parameters. Both the mean values and the uncertainties on these three parameters, along with the pivot values for redshift and intrinsic richness, are listed in Eq. (4.19). It is important to outline that in order to obtain a mass value, it is necessary to assume a cosmological model, because the scaling

relation depends on cosmology. However, as we shall discuss in Section 5.8, we will overcome the limit of the assumption of a cosmology a priori.

The evaluation of uncertainties is necessary also for the redshifts z. In addition, we point out that all the redshifts are previously corrected for the bias described in Chapter 4. Also in this case, the procedure is based on Monte Carlo extractions from Gaussian probability distributions, obtained from the mock cluster catalogue. These Gaussian distributions, in particular, describe the probability to obtain a true value of redshift given an observed one, namely $P(z_{tr}|z_{obs})$. We outline that when we perform such extractions, we account for the dispersion of the distribution $P(z_{tr}|z_{obs})$, obtaining a proxy value z of the true redshift. For the sake of clarity, from now on we will refer to the distribution $P(z_{tr}|z_{obs})$ as $P(z|z_{obs})$. In the left panel of Fig. 5.6, we show a typical case of these probability distributions, while in the right panel the values of the standard deviations of such distributions are represented as a function of the redshift z. As for the case of the completeness, each value of redshift in the catalogue is assigned to the relative bin, then the true values are randomly extracted from the Gaussian probability distributions relative to each bin.

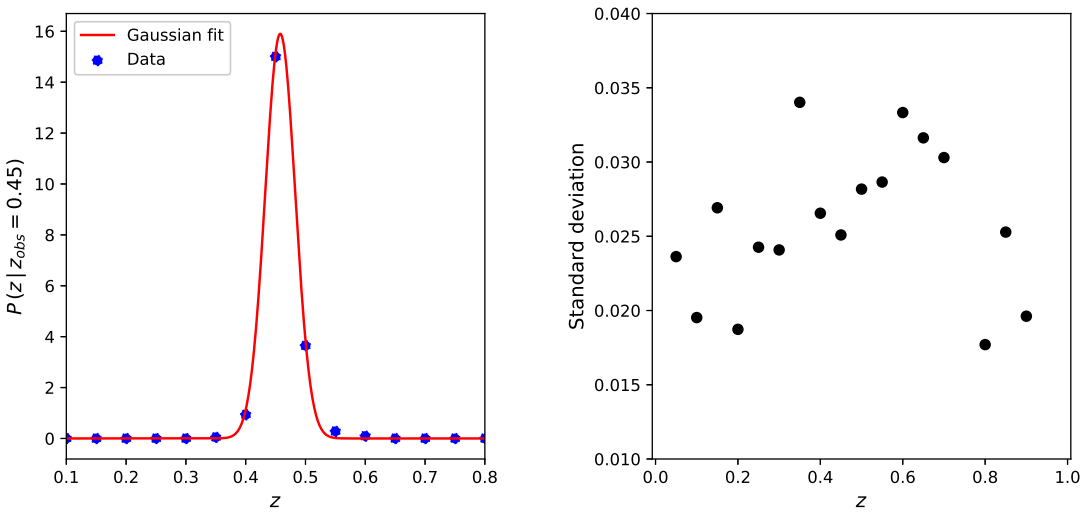

Figure 5.6: In the left panel, probability distribution $P(z|z_{obs})$ for the case of a bin with a central value of the observed redshift equal to $z_{obs} = 0.45$. On the right, the values of the standard deviation of the probability distributions $P(z|z_{obs})$ retrieved from the mock catalogue.

At this level of the analysis, a proxy value z of the true redshift z_{tr} is associated to each object of the catalogue, along with a value of mass M. Having an estimate of the proxy value of redshift we can apply the selection function, which is indeed dependent on z, as we detailed in Section 5.3. In this way we assign a weight w to every galaxy cluster in the catalogue. Therefore each object, labeled as i, is completely defined, for the purposes of our analysis, by the triplet $\{z_i, M_i, w_i\}$, namely by a proxy value of redshift, a mass and a weight.

As already mentioned, we exclude the redshift bin $z \in [0.6, 0.8]$ after these Monte Carlo extractions. In this way we avoid any significant loss of objects due to bin changes. In Fig. 5.7 we show the results obtained by the extractions of the redshift and of the scaling relation, considered separately and neglecting the selection function. It turns out that the Gaussian extractions relative to the scaling relation provide results consistent within 1σ with respect to the original catalogue. On the other hand, the redshift extractions are significant. The standard deviation of the probability distributions $P(z|z_{obs})$, as shown in the right panel of Fig. 5.6, ranges from ~ 0.017 to ~ 0.035, then the changes of redshift bins are abundant. Indeed, the scatter of the redshift values is not negligible with respect to the width of the redshift bins considered. However, it turns out that these fluctuations are not so relevant in our analysis. In Fig. 5.8 we can see the differences in the counts between the cases with and without extractions, for each redshift bin. The largest variations manifest themselves at very low masses, and we point out that this low mass regime, below $M_{200} \sim 5 \cdot 10^{13}\ \mathrm{M}_\odot\, h^{-1}$, will not be considered in the analysis due to its severe incompleteness, as we discussed in Section 5.3.

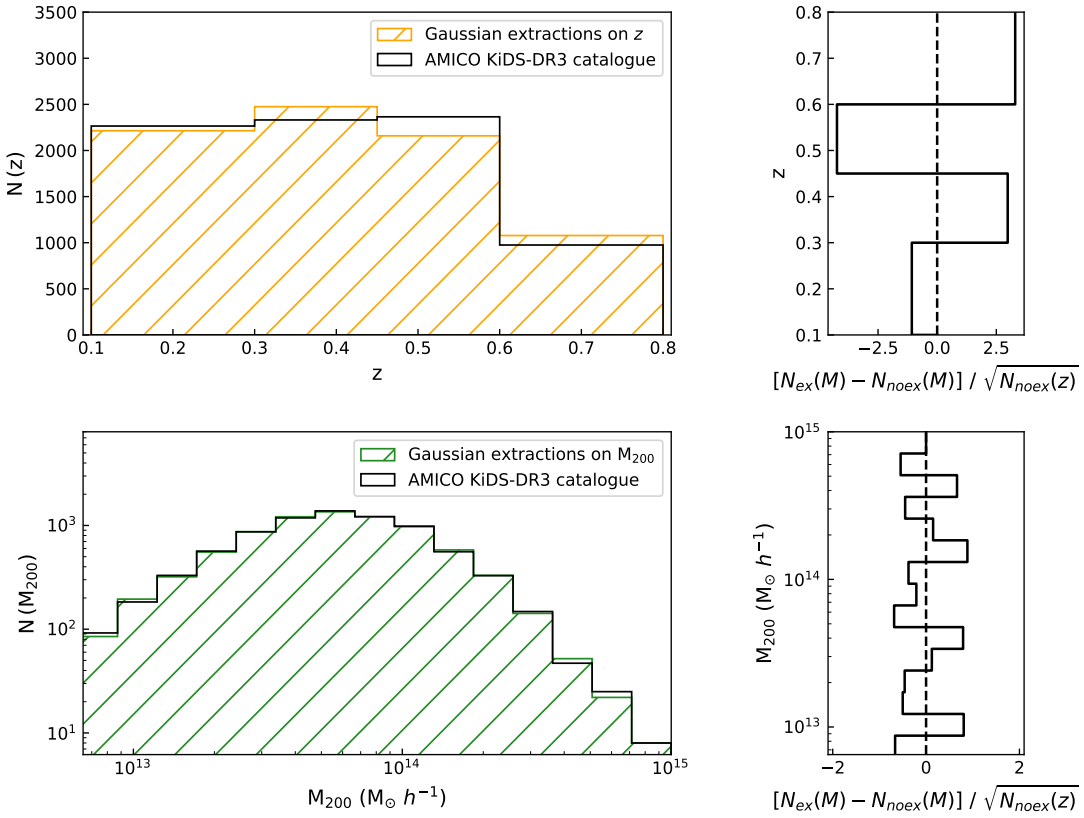

Figure 5.7: The AMICO KiDS-DR3 cluster counts with and without the Monte Carlo extractions of redshift and masses, not correcting for the selection function. The left top panel shows the number of objects as a function of the redshift (black histogram), and after Gaussian extractions of the values of the proxies of the true redshift (barred histogram). On the bottom left panel we show the number of objects as a function of the mass, from the catalogue (black histogram) and as a result of Gaussian Monte Carlo extractions of the scaling relation parameters (barred histogram). The values of the masses in the catalogue have been obtained by neglecting the uncertainties on the scaling relation, and assuming $H_0 = 70$ km/s/Mpc and $\Omega_m = 0.3$. In the right panels, N_{noex} and N_{ex} represent the counts obtained from the original catalogue and from Gaussian extractions, respectively. These panels show the ratio of the difference $(N_{ex} - N_{noex})$ over the Poissonian error relative to N_{noex}. Significant differences with respect to the original catalogue are present only in the case of redshift extractions.

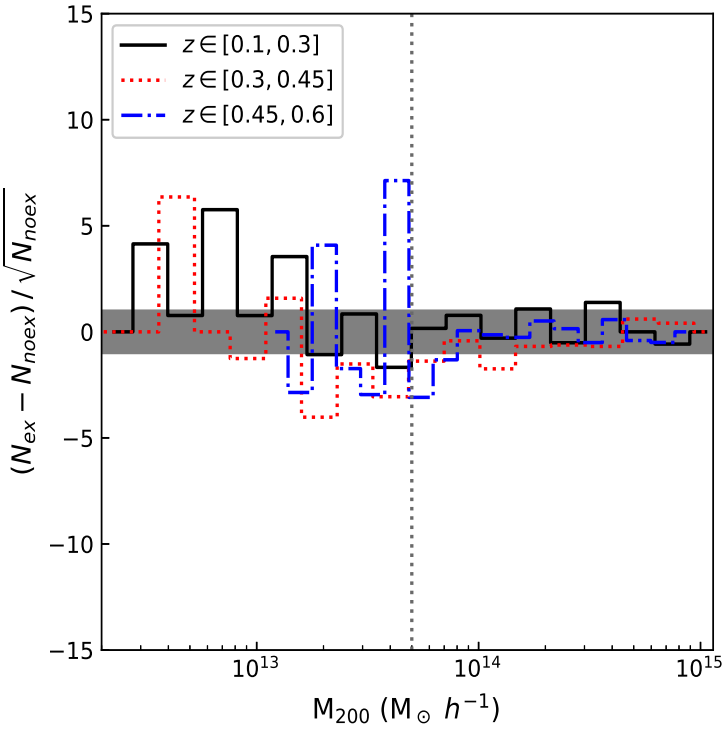

Figure 5.8: Ratio of the difference $(N_{ex} - N_{noex})$ over the Poissonian error relative to N_{noex}, where N indicates the counts as a function of the mass, in the redshift bins $z \in [0.1, 0.3]$, $[0.3, 0.45]$, $[0.45, 0.6]$. The counts weighted for the selection function are considered, and Monte Carlo extractions of redshift and scaling relation are performed. The vertical dotted line marks the threshold at $5 \cdot 10^{13}$ $M_\odot$ h^{-1} between the objects considered in the analysis, on the right, and the discarded ones. The horizontal grey bar indicates the interval $[-1; 1]$.

5.7 *Pipeline I* for a flat ΛCDM Universe

As a general approach in this work, we perform a cosmological analysis of cluster number counts based on the assumption of a flat ΛCDM model (see Section 1.9). The aim is to constrain in a first instance the matter density parameter Ω_m, defined as $\Omega_m \equiv \rho_m / \rho_c$, and σ_8, defined as the square root of the mass variance σ_M (Eq. 1.152) computed at $z = 0$ on scales of 8 Mpc/h. Therefore we set them as free parameters of the model, which in the framework of *Pipeline I* is defined by Eq. (5.2). We outline that the values of both Ω_m and σ_8 are at redshift $z = 0$, and we avoid the notation $\Omega_{0,m}$ for compactness. In particular, given an observation of cluster counts at a given redshift z^*, in the modelling procedure the values of Ω_m and σ_8 are set at $z = 0$, and their values at z^* are retrieved by considering their evolution.

The other fundamental parameters are fixed to the Planck values. We consider the values obtained by Planck Collaboration 2018, Paper VI (Table 2,

TT,TE,EE+lowE+lensing), which in particular are the baryon density parameter $\Omega_b = 0.0486$, the parametrization of the Hubble constant $h = 0.6736$ and the spectral index $n_s = 0.9649$. Furthermore, in this baseline cosmological model we assume three neutrino species, approximated as two massless states and a single massive neutrino of mass $m_\nu = 0.06$ eV.

In our analysis we will also constrain the value of the *cluster normalization condition parameter* S_8, defined as

$$S_8 \equiv \sigma_8 \left(\frac{\Omega_m}{0.3} \right)^{0.5} . \tag{5.6}$$

The significance of this parameter is rooted in the degeneracy between σ_8 and Ω_m. In particular, S_8 is defined along the $\sigma_8 - \Omega_m$ confidence regions. Since the number of massive clusters increases with both σ_8 and Ω_m, in order to hold the cluster abundance fixed at its observed value, any increase in σ_8 must be compensated by a decrease in Ω_m, implying that S_8 is held fixed.

5.7.1 Modelling $N(M)$ in different bins of redshift

In the following we take the case without extractions as the reference. In fact, we compare the results obtained with the *Pipeline I* with those retrieved by considering the objects in the original catalogue, on which we only apply the corrections for the completeness and the purity.[3] Furthermore, in the case without extractions the masses of the clusters are derived by assuming $h = 0.70$ and $\Omega_m = 0.30$ in the scaling relation, Eq. 4.18. The counts in the two cases, that is without extractions and with *Pipeline I*, are shown in Fig. 5.9. We can appreciate the overall agreement with both Planck18 and WMAP9.

Turning to the analysis, the first step we perform in all the redshift bins consists in considering first only the high mass regime, within which the completeness and the purity of the sample are $\simeq 1$. In particular the minimum masses that define the regime with purity and completeness $\simeq 1$ are, from the first to the last redshift bin, $1.4 \cdot 10^{14}$ $M_\odot$ h^{-1}, $1.45 \cdot 10^{14}$ $M_\odot$ h^{-1}, $1.78 \cdot 10^{14}$ $M_\odot$ h^{-1}. Consequently, we gradually consider lower minimum masses M_{min}. In Fig. 5.10 we show the results on Ω_m and σ_8 for the two cases considered, with and without extractions, for different values of M_{min}. In particular, given a redshift bin we select the same M_{min} for the two cases.

The best-fit values of Ω_m and σ_8 retrieved by assuming different cuts in minimum mass are in agreement in a given redshift bin, both by considering the case without extractions and *Pipeline I*. Furthermore, the obtained values of Ω_m

[3] In order to apply the correction for the completeness, it is always necessary to perform extractions. If we would not act in this way, indeed, we would introduce a guaranteed bias on the data.

and σ_8 remain consistent by assuming different minimum masses. The only remarkable difference between extractions and no extractions appears for a high minimum mass in the redshift bin $z \in [0.45, 0, 6]$ for the case without extractions (lower panels in Fig. 5.10). This is a typical behavior emerging for some choices of mass ranges, especially if only a few bins of mass are considered for the fit. Indeed, when we consider lower values of M_{min}, the results become consistent with those obtained in *Pipeline I* and additionally with Planck18.

Focusing on the case of *Pipeline I*, another interesting feature of the results shown in Fig. 5.10 is that, in the first and last redshift bins, the constraints on Ω_m and σ_8 are consistent with Planck18 and WMAP9 almost in all cases. On the other hand, in the redshift bin $z \in [0.3, 0.45]$ our results are in agreement with Costanzi18.

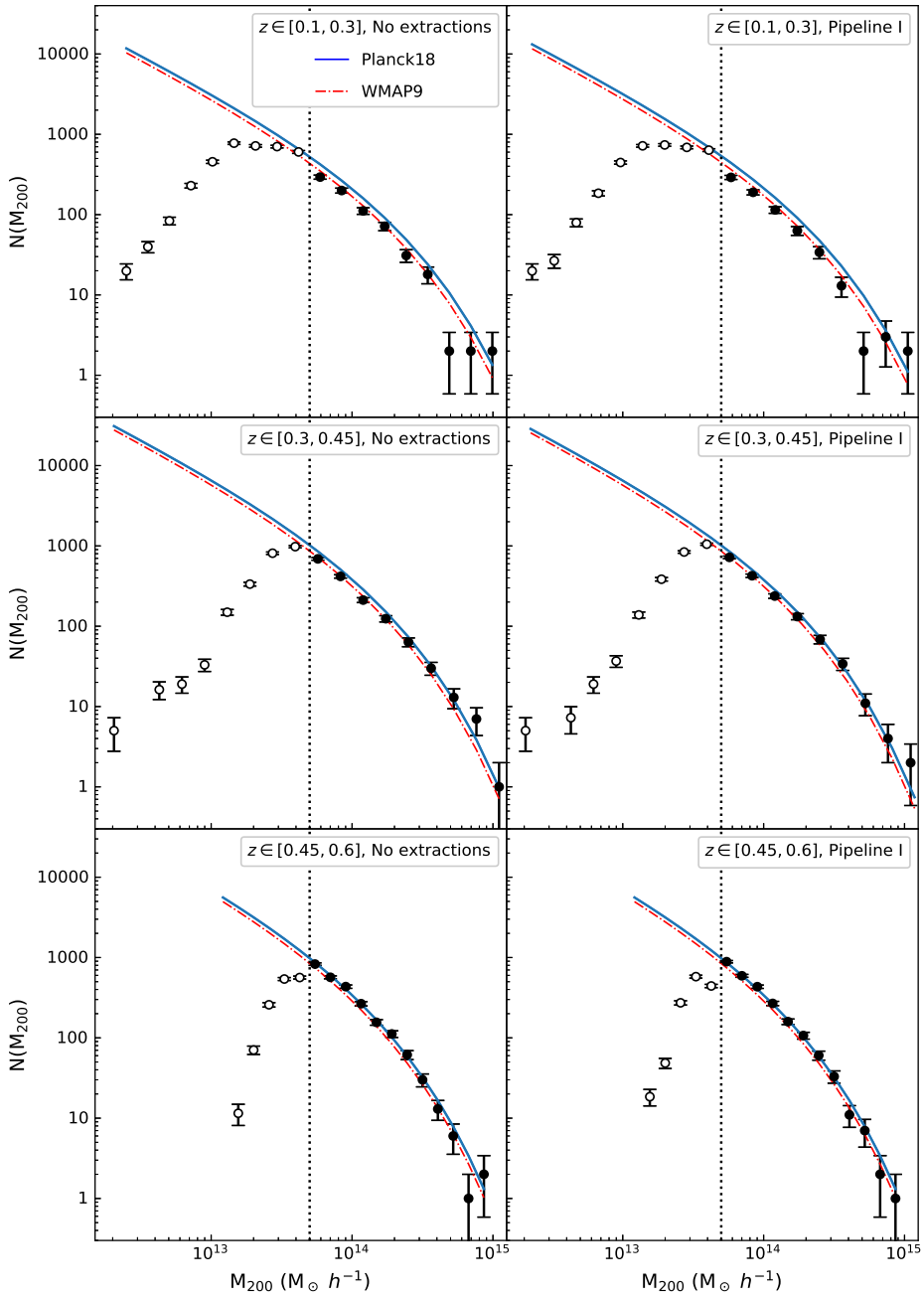

Figure 5.9: Counts of the galaxy clusters in the AMICO KiDS-DR3 catalogue as a function of the mass, weighted for the selection function, in the redshift bins $z \in [0.1, 0.3]$, $[0.3, 0.45]$, $[0.45, 0.6]$. The cases without extractions of the uncertainties on the data are shown in the left panels, while the cases with extractions (*Pipeline I*) are shown on the right side. The filled black dots represent the counts considered in the analysis. The error bars are referred to the Poissonian uncertainties relative to the weighted counts. The vertical black dotted line represents the minimum cut in mass considered in our pipelines. The blue solid lines show the Planck18 prediction, while the dashed red lines are referred to WMAP9.

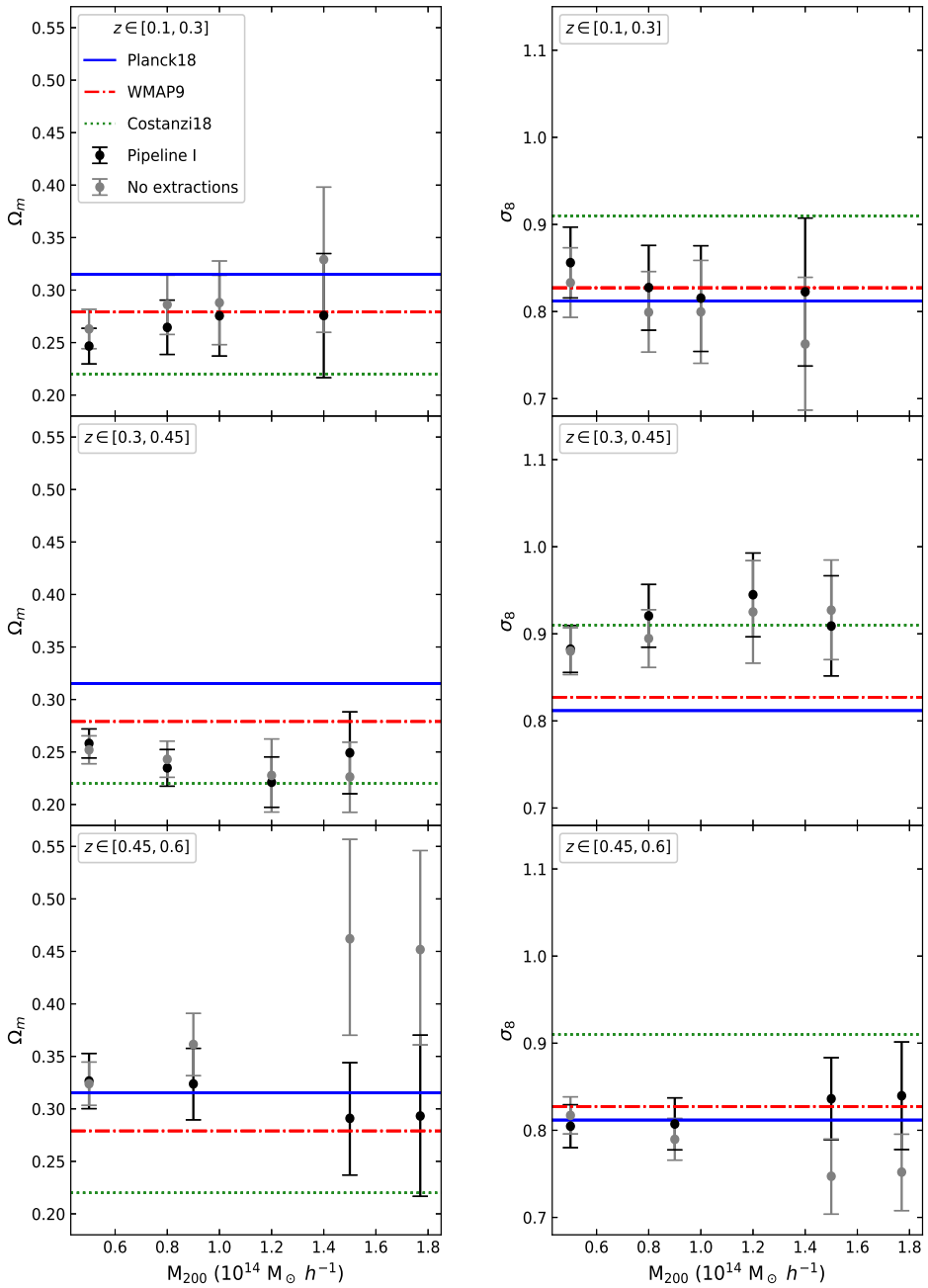

Figure 5.10: In the left panels, the best-fit values of Ω_m obtained as the median values of the marginalized posterior, as a function of the minimum mass M_{min} considered in the analysis. On the right, the values of σ_8 as a function of M_{min}. Both the parameters are computed in the three redshift bins of interest, both in the case without extractions (grey dots) and with *Pipeline I* (black dots). The blue solid lines represent the values of Planck18, the red dashed lines represent WMAP9, while the green dotted lines provide the values obtained by Costanzi18.

Furthermore, it is important to consider also the 2D confidence contours in the posterior, in order to have a complete view of the results, and to assess the degeneracy between Ω_m and σ_8. As we can see in Fig. 5.11, we find that the constraints on the cosmological parameters obtained in different redshift bins are in good agreement for the case of extractions, i.e. *Pipeline I*, and within the high mass regime, where the counts have weights ~ 1 (first and third right panels). The confidence contours in the other cases are not consistent simultaneously in the three redshift bins, despite they show agreement with the constraints provided by Planck18, WMAP9 and Costanzi18. Furthermore, we can notice the tendency of the confidence contours to become tighter when we consider lower values of M_{min} (the panels labeled as *Minimum cut in mass* in the figure), a behavior also evidenced in the error bars in Fig. 5.10. This is due to the nature of the Poissonian error, associated to the cluster counts: the relative error decreases when the counts become larger, that is at low masses. In turn, the consideration of the low masses critically affects the outcome of our analysis. Despite we show only the extreme cases of the cuts in mass, i.e. the minimum and the maximum M_{min}, the same behavior holds for the other cuts in minimum mass.

Subsequently, we proceed by taking into consideration the marginalized posterior distributions of σ_8, Ω_m and S_8. We show these results in the Figures 5.12, 5.13, 5.14.

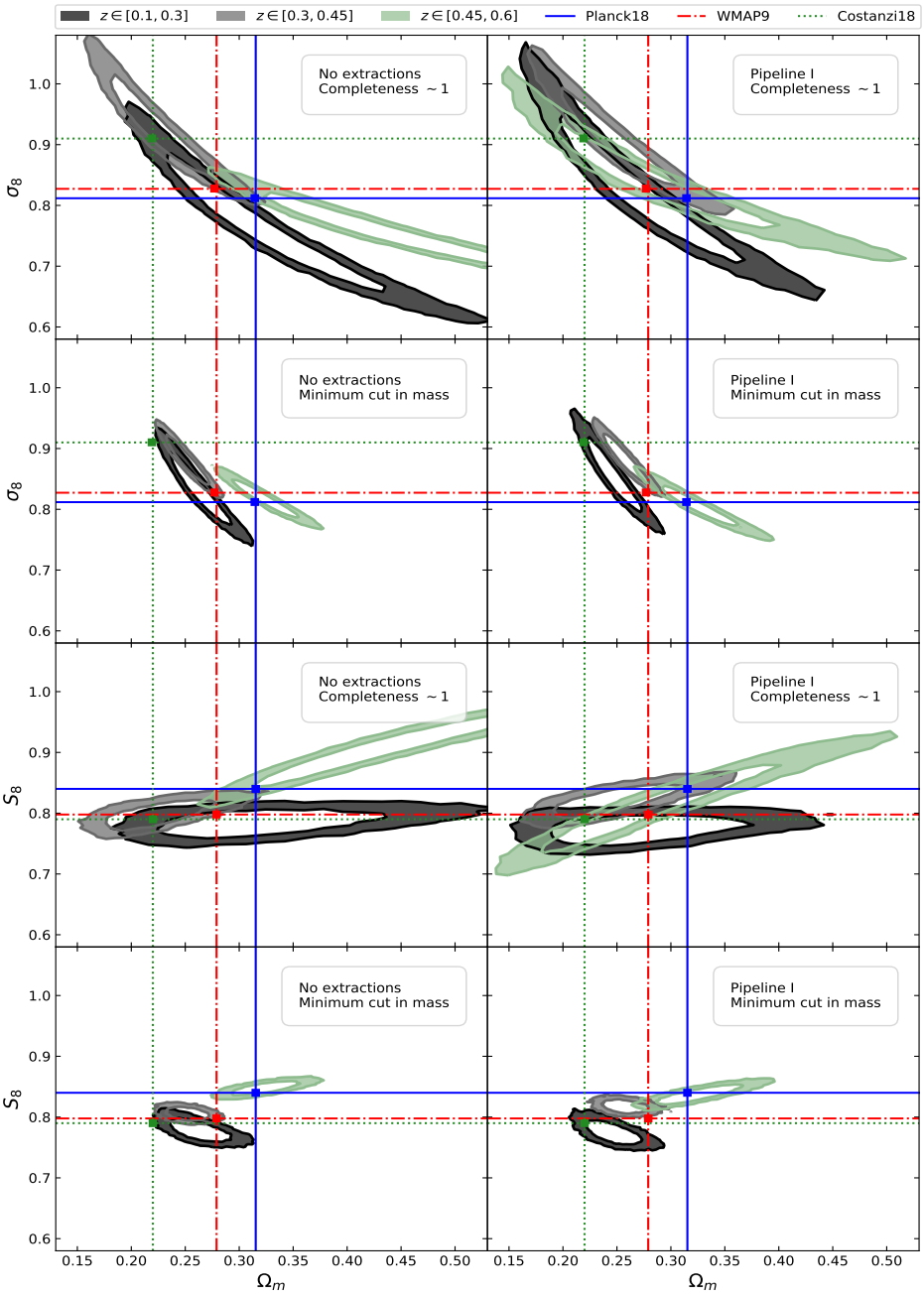

Figure 5.11: Confidence contours at 68% and 95% in the parameter spaces defined by $\Omega_m - \sigma_8$ (top four panels) and by $\Omega_m - S_8$ (bottom four panels), for the cases of completeness and purity $\simeq 1$ and minimum $M_{min} = 5 \cdot 10^{13}$ $M_\odot$ h^{-1}. The cases without extractions are shown on the left, while on the right we have the results from *Pipeline I*. The black, grey and green bands define the interval between the 68% and 95% confidence levels, respectively, for $z \in [0.1, 0.3]$, $[0.3, 0.45]$, $[0.45, 0.6]$. The blue solid lines represent the values of Planck18, the red dashed lines represent WMAP9 values, while the green dotted lines provide the values obtained by Costanzi18.

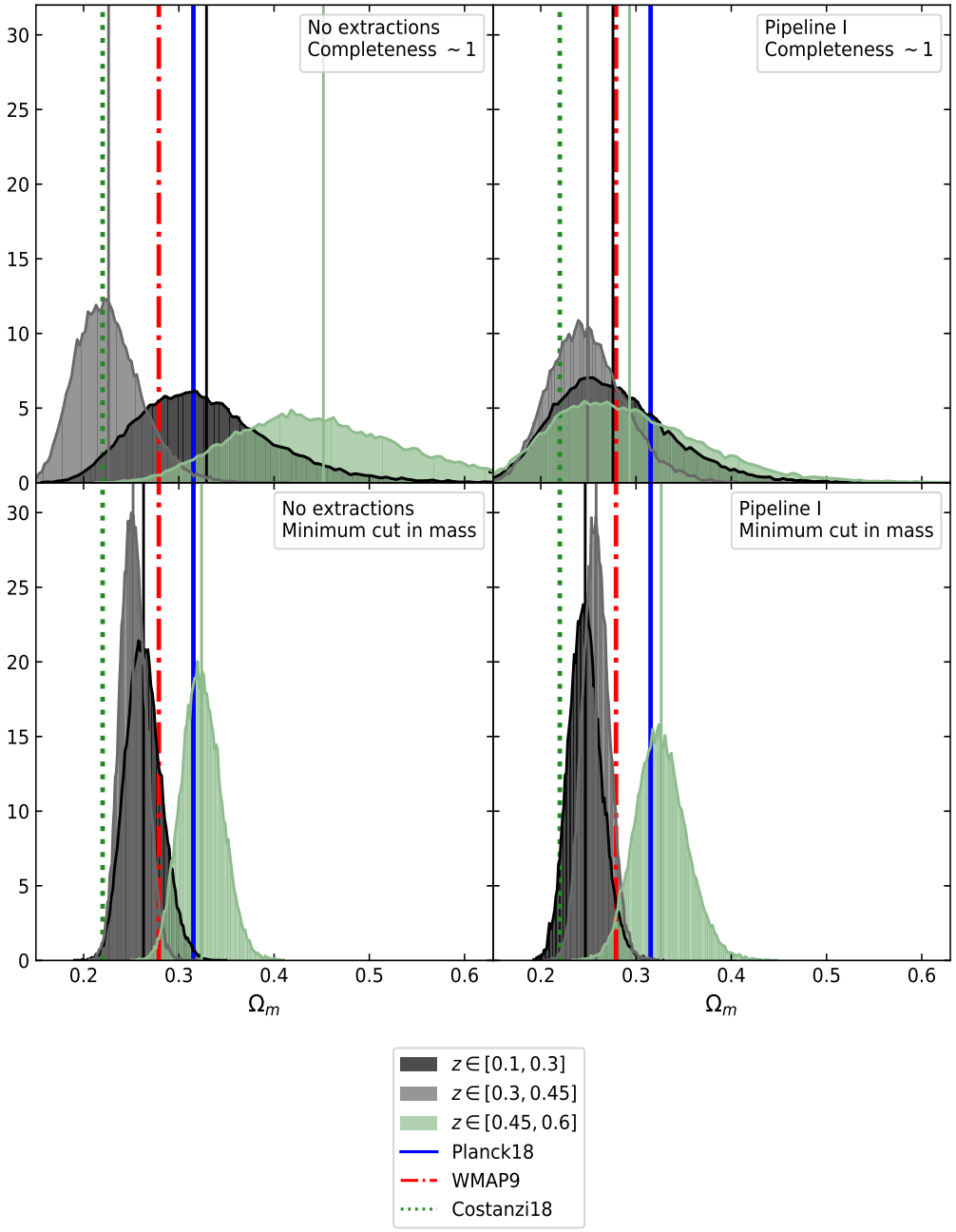

Figure 5.12: Marginalized posteriors for Ω_m in the case without extractions (left panels) and *Pipeline I* (right panels). The top panels show the cases in a complete regime, while the bottom panels present the case of the lowest cut in mass considered in the analysis, namely $M_{min} = 5 \cdot 10^{13}$ M$_\odot$ h^{-1}. The black, grey and green histograms represent the marginalized histograms in the redshift ranges $z \in [0.1, 0.3]$, $[0.3, 0.45]$, $[0.45, 0.6]$, respectively. The means of these distributions are represented by vertical lines with the same colors of the correspondent histograms. The blue solid lines represent the values of Planck18, the red dashed lines represent WMAP9 values, while the green dotted lines provide the values obtained by Costanzi18.

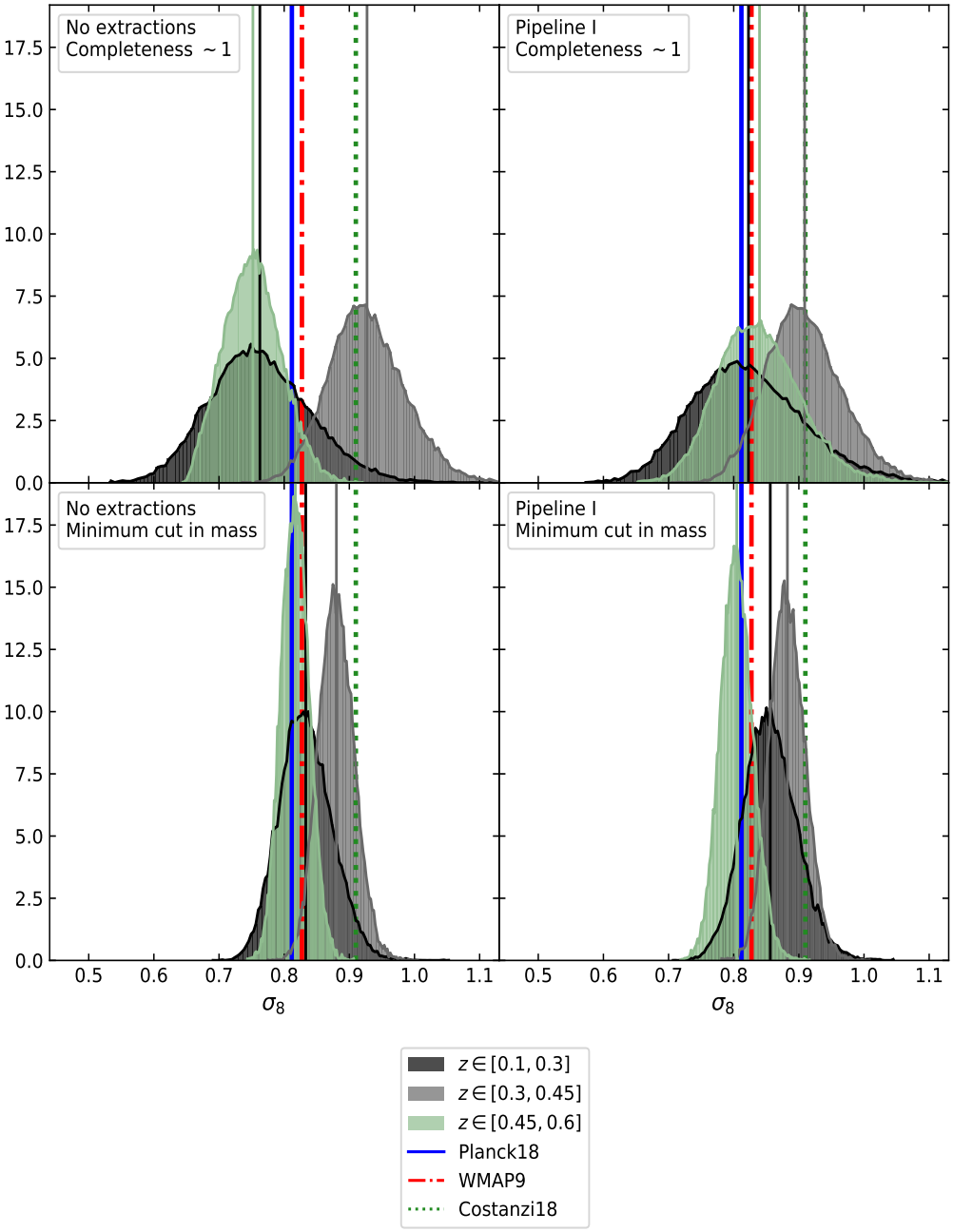

Figure 5.13: Marginalized posteriors for σ_8 in the case without extractions (left panels) and *Pipeline I* (right panels). The symbols are the same as in Fig. 5.12.

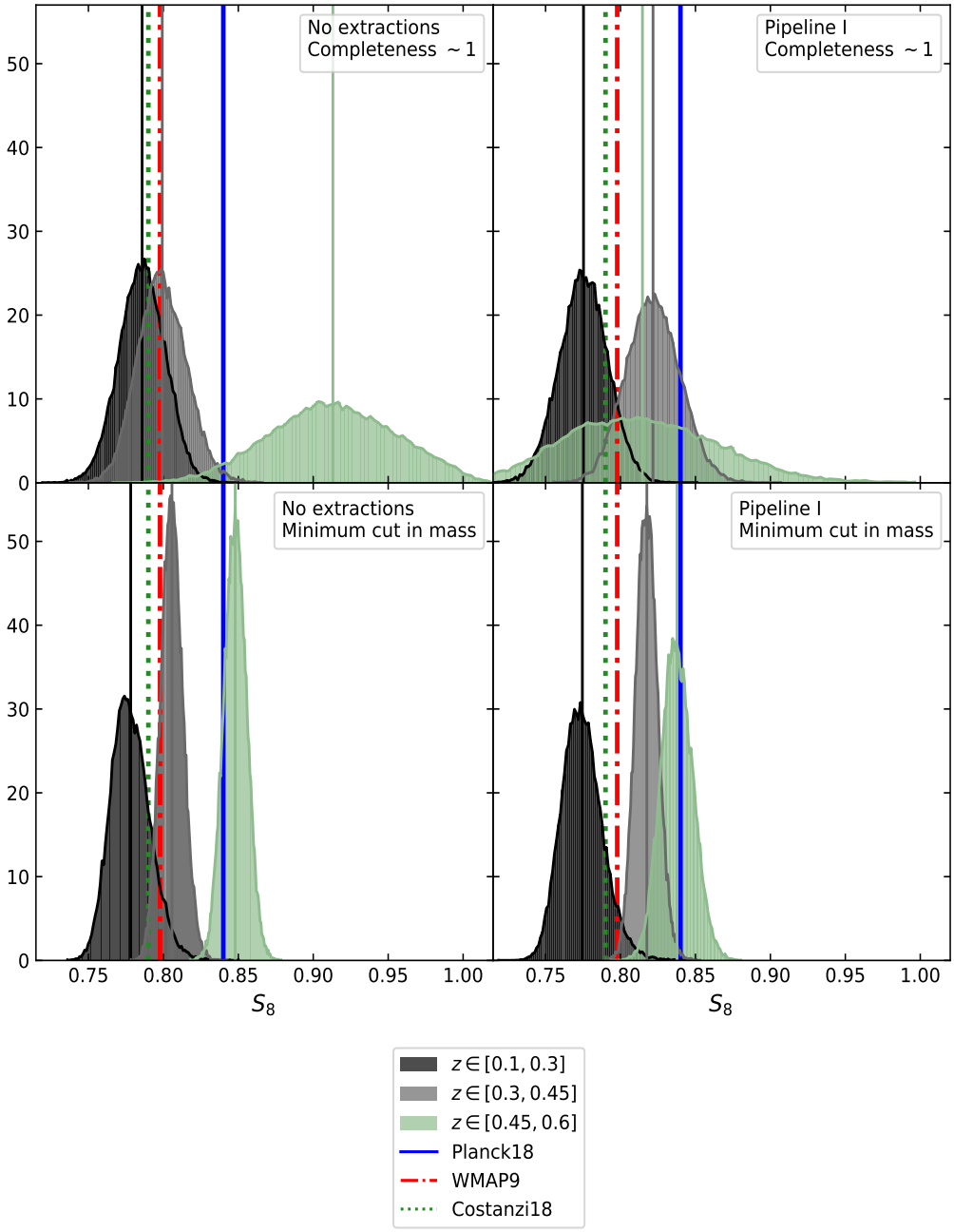

Figure 5.14: Marginalized posteriors for S_8 in the case without extractions (left panels) and *Pipeline I* (right panels). The symbols are the same as in Fig. 5.12.

The posteriors obtained in the different redshift bins can be combined, being these conditionally independent parts of the dataset. Given the good agreement between the results in the three redshift bins for the case of Pipeline I and complete regime of the counts, shown in the Figures 5.12, 5.13, 5.14, we proceed with the product of the posteriors for our three parameters in this case, as shown in Fig. 5.15. We derive the following constraints:

$$\begin{cases} \Omega_m = 0.25^{+0.03}_{-0.03} \\ \sigma_8 = 0.86^{+0.04}_{-0.04} \\ S_8 = 0.80^{+0.01}_{-0.01} \end{cases} \tag{5.7}$$

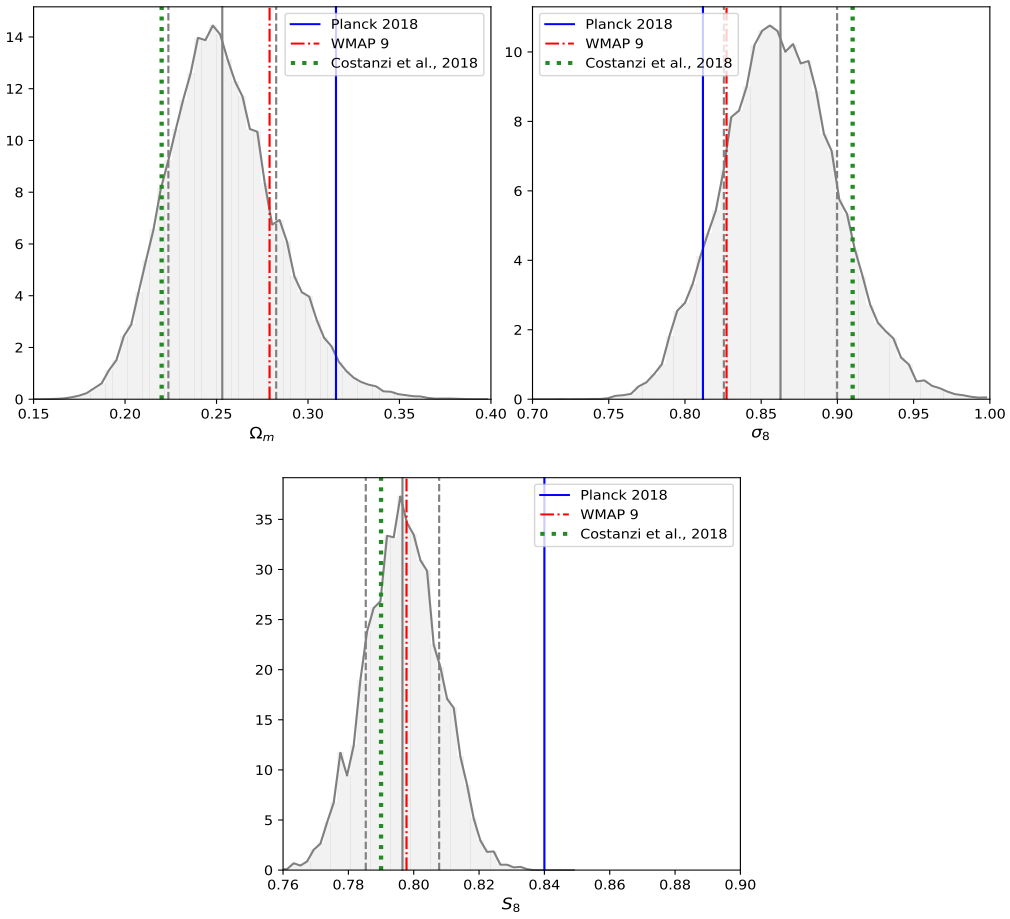

Figure 5.15: Combined marginalized posteriors for Ω_m, σ_8 and S_8 from the three bins of redshift considered in the analysis, within the case of *Pipeline I* and considering the regime of high masses. The vertical dashed lines over the marginalized histograms show the 16-th, 50-th and 84-th percentiles.

5.7.2 Considerations on $N(M)$

So far we have dealt with counts of galaxy clusters as a function of the mass M, in a given redshift bin. What we found is a general inconsistency between the results in different redshift bins, for a fixed minimum mass M_{min}, apart for the case of Monte Carlo extractions, in *Pipeline I*, within the complete regime. Of course we are neglecting several sources of error at the likelihood level, in the covariance matrix that defines our likelihood function. Indeed, by means of Monte Carlo extractions we scatter the data but we do not enhance the freedom of the fitting procedure.

Adding additional sources of error in the likelihood, however, is everything but trivial. The reason is that in order to include in our analysis the most reliable part of the dataset, the high masses, we need to assume a Poissonian likelihood, due to the low counts in this regime. This assumption is highly limiting since a Poissonian distribution is completely defined by the diagonal of its covariance matrix. Then we would need an appropriate convolution of the Poissonian likelihood with at least another distribution, in general a Gaussian, one for each additional source of error. We will introduce one of these convolutions, in Section 5.10, in order to account for the most interesting among the additional sources of error: the super sample covariance. As we shall see, this additional contribution to the uncertainties does not rectify the inconsistency between the results in different redshift ranges, albeit it implies very interesting effects when we consider the whole dataset at the same time in the modelling.

With regard to the rest of the sources of uncertainties to be considered at the likelihood level we are neglecting, for example: the error on the selection function, on photometric redshift, on the scaling relation, and the intrinsic scatter of the scaling relation. Apart from the latter, all these contributions require simulations, and we will perform them in the near future.

5.7.3 Modelling the whole dataset

After the considerations on $N(M)$, we take into account all the bins of redshift $z \in [0.1, 0.3]$, $[0.3, 0.45]$, $[0.45, 0.6]$ simultaneously in the modelling, along with the bins of mass previously considered, by modelling $N(z, M)$. In this way, we aim at evaluating if there is any substantial difference, with respect to the case of $N(M)$, in the confidence contours.

The answer is immediate by looking at Fig. 5.16, in which we show the confidence contours in the parameter spaces defined by the couple $\Omega_m - \sigma_8$, $\Omega_m - S_8$. In particular we show the 68% and 95% confidence levels retrieved in each bin of redshift separately, and those obtained considering the whole dataset at once. Therefore, as we can see, the modelling of $N(z, M)$ provides the combination of the posteriors of the parameters, retrieved separately in the three bins of redshift. Of course, despite in Fig. 5.16 it might seem that the product should return zero,

we point out that we show only the 68% and 95% confidence levels. The rest of the parameter space, indeed, is not empty.

Let us then visualize more in detail, in Fig. 5.17 and Fig. 5.18, the results that the whole dataset taken into consideration provides us, within the framework of *Pipeline I*. In Fig. 5.17 we show the case of the confidence contours retrieved from the modelling of $N(z, M)$, by considering the three redshift bins and the high mass regime, that is the mass domain in which purity and completeness are $\simeq 1$. There is a general agreement with the external datasets, and we outline the fact that for the cases of Planck18, WMAP9 and Costanzi et al. (2018) we are just showing the mean values of the marginalized posteriors of the parameters. We retrieve, from this case of $N(z, M)$ in the regime of high purity and completeness, the following constraints on the cosmological parameters:

$$\begin{cases} \Omega_m = 0.27^{+0.02}_{-0.02} \\ \sigma_8 = 0.86^{+0.02}_{-0.02} \\ S_8 = 0.81^{+0.01}_{-0.01} \end{cases} \tag{5.8}$$

By considering the case of the lowest cut in minimum mass, $M_{min} = 5 \cdot 10^{13}$ $M_\odot$ h^{-1}, shown in Fig. 5.18, we can see how the tightness of the confidence contours inhibits the agreement with the external datasets. We have in this case the following, restrictive, constraints on Ω_m, σ_8 and S_8:

$$\begin{cases} \Omega_m = 0.258^{+0.007}_{-0.007} \\ \sigma_8 = 0.875^{+0.013}_{-0.013} \\ S_8 = 0.811^{+0.004}_{-0.004} \end{cases} \tag{5.9}$$

However, as we can see in Fig. 5.19, we have a majestic agreement between the case of $N(z, M)$ modelled by considering only the high mass regime, and the case with the lowest cut in minimum mass. We can conclude that the constraints on Ω_m, σ_8 and S_8 are broadly defined by the high mass regime, while the consideration of lower minimum masses restricts the uncertainties.

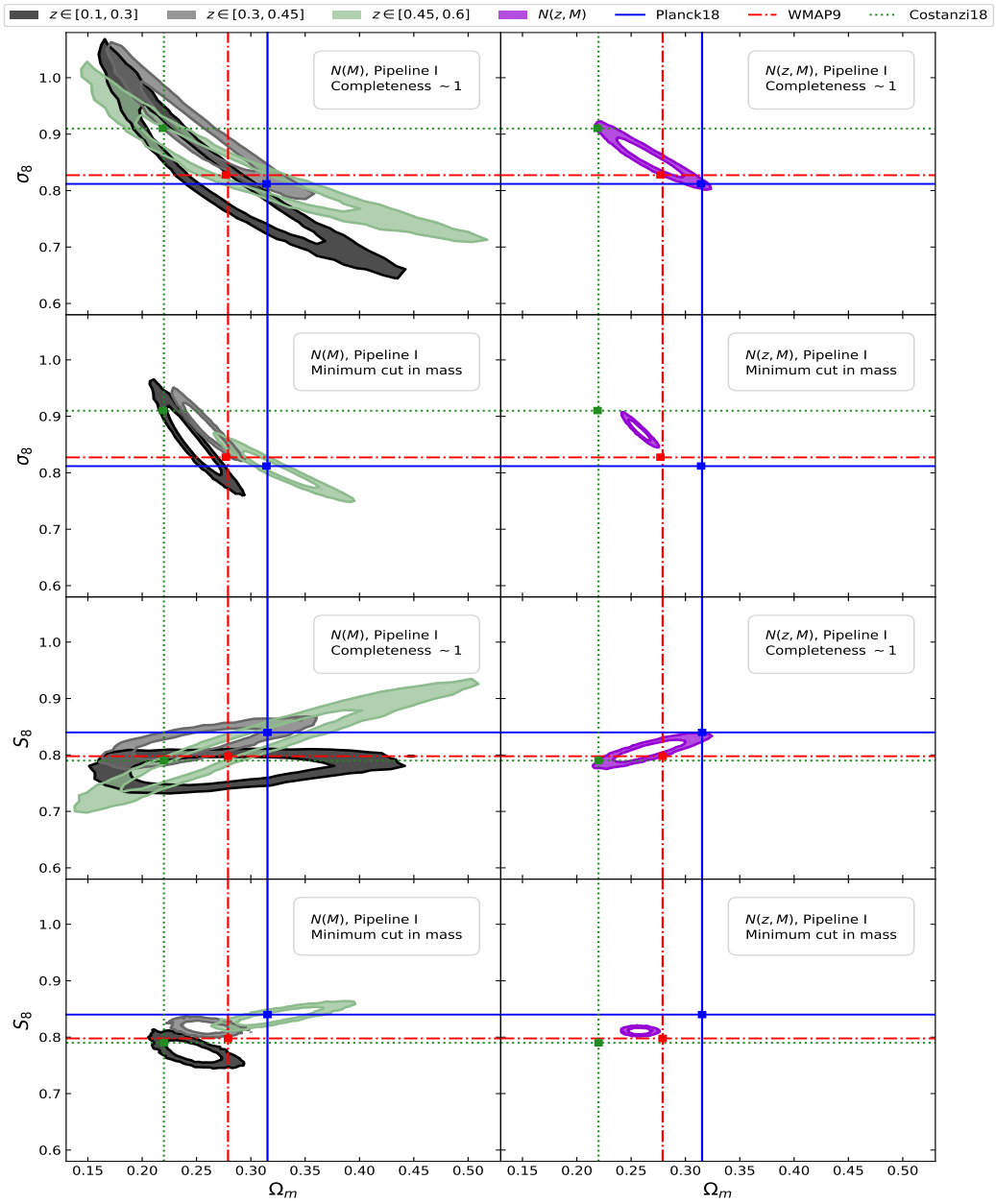

Figure 5.16: Case of Pipeline I. Confidence contours at 68% and 95% in the parameter spaces defined by $\Omega_m - \sigma_8$ (top four panels) and by $\Omega_m - S_8$ (bottom four panels), for the cases of completeness and purity $\simeq 1$ and minimum $M_{min} = 5 \cdot 10^{13}$ $M_\odot$ h^{-1}. The case of $N(M)$ is shown in the left panels, while the case of $N(z, M)$ is shown on the right. The black, grey and green bands define the interval between the 68% and 95% confidence levels respectively for $z \in [0.1, 0.3]$, $[0.3, 0.45]$, $[0.45, 0.6]$, for the case of $N(M)$. The magenta bands define the interval between 68% and 95% confidence levels for the case of $N(z, M)$. The blue solid line represents the values of Planck18, the red dashed line represents WMAP9, while the green dotted line provides the values obtained by Costanzi et al. (2018).

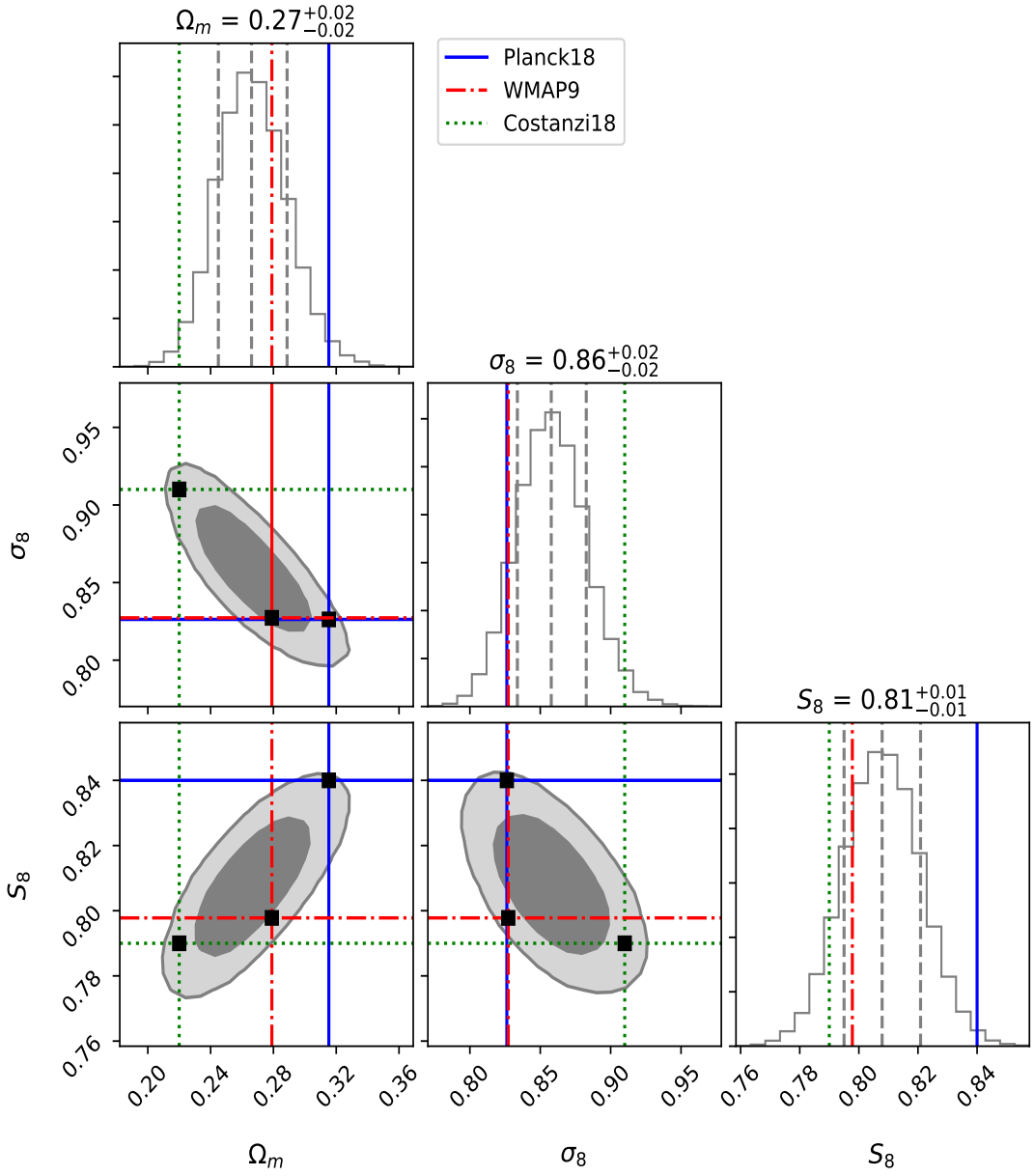

Figure 5.17: Complete visualization of the constraints obtained by modelling $N(z, M)$ in Pipeline I, considering the redshift bins $z \in [0.1, 0.3]$, $[0.3, 0.45]$, $[0.45, 0.6]$ and the high mass regime. We show the confidence contours at 68% and 95% in the parameter spaces defined by $\Omega_m - \sigma_8$, $\Omega_m - S_8$ and $\sigma_8 - S_8$, along with the marginalized histograms. The vertical dashed lines over the marginalized histograms show the 16-th, 50-th and 84-th percentiles. The blue solid line represents the values of Planck18, the red dashed line represents WMAP9, while the green dotted line provides the values obtained by Costanzi et al. (2018).

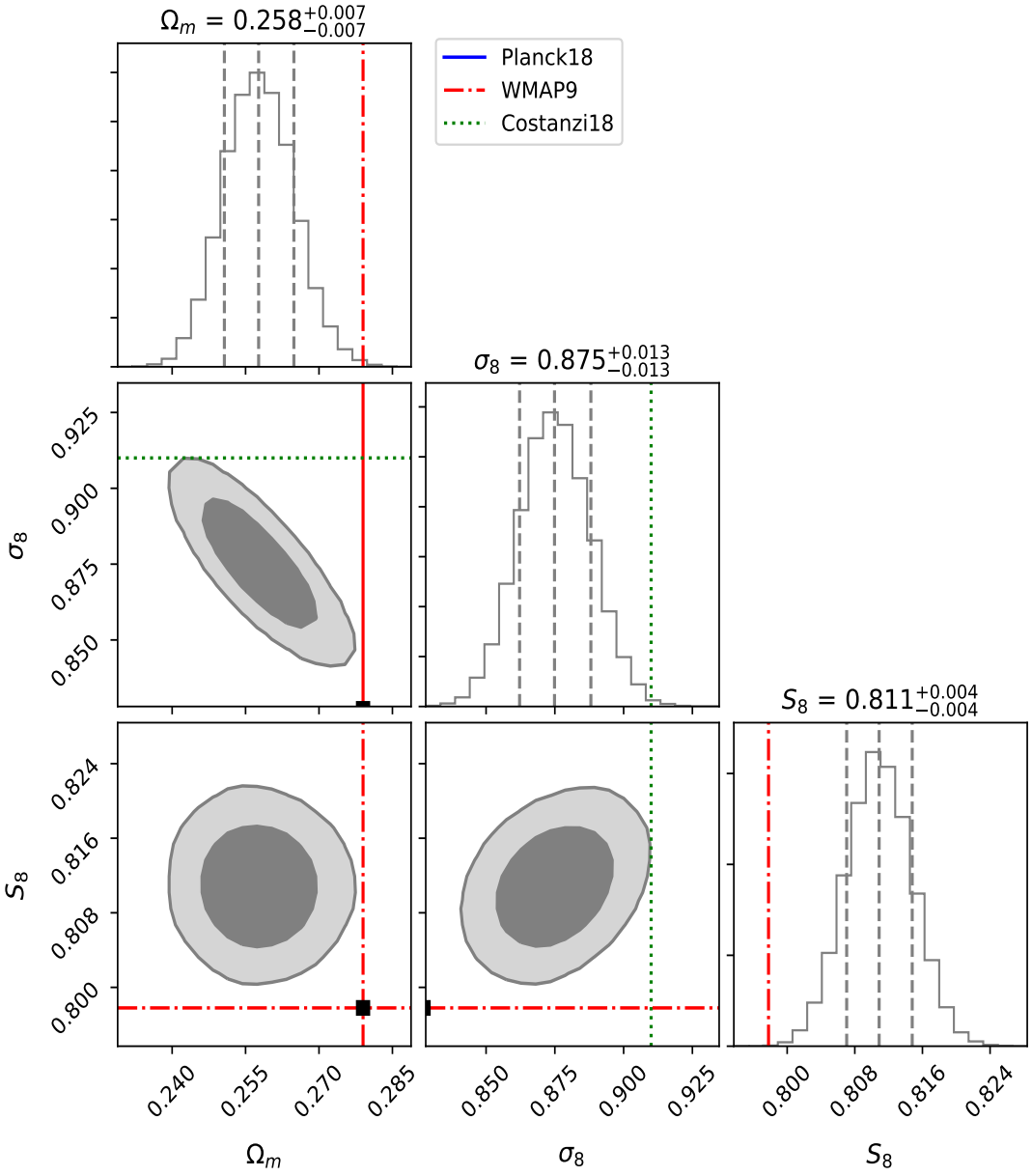

Figure 5.18: Complete visualization of the constraints obtained by modelling $N(z, M)$ in Pipeline I, considering the redshift bins $z \in [0.1, 0.3]$, $[0.3, 0.45]$, $[0.45, 0.6]$ and the minimum cut in mass, $M_{min} = 5 \cdot 10^{13}$ $M_\odot$ h^{-1}. We show the confidence contours at 68% and 95% in the parameter spaces defined by $\Omega_m - \sigma_8$, $\Omega_m - S_8$ and $\sigma_8 - S_8$, along with the marginalized histograms. The vertical dashed lines over the marginalized histograms show the 16-th, 50-th and 84-th percentiles. The blue solid line represents the values of Planck18, the red dashed line represents WMAP9, while the green dotted line provides the values obtained by Costanzi et al. (2018).

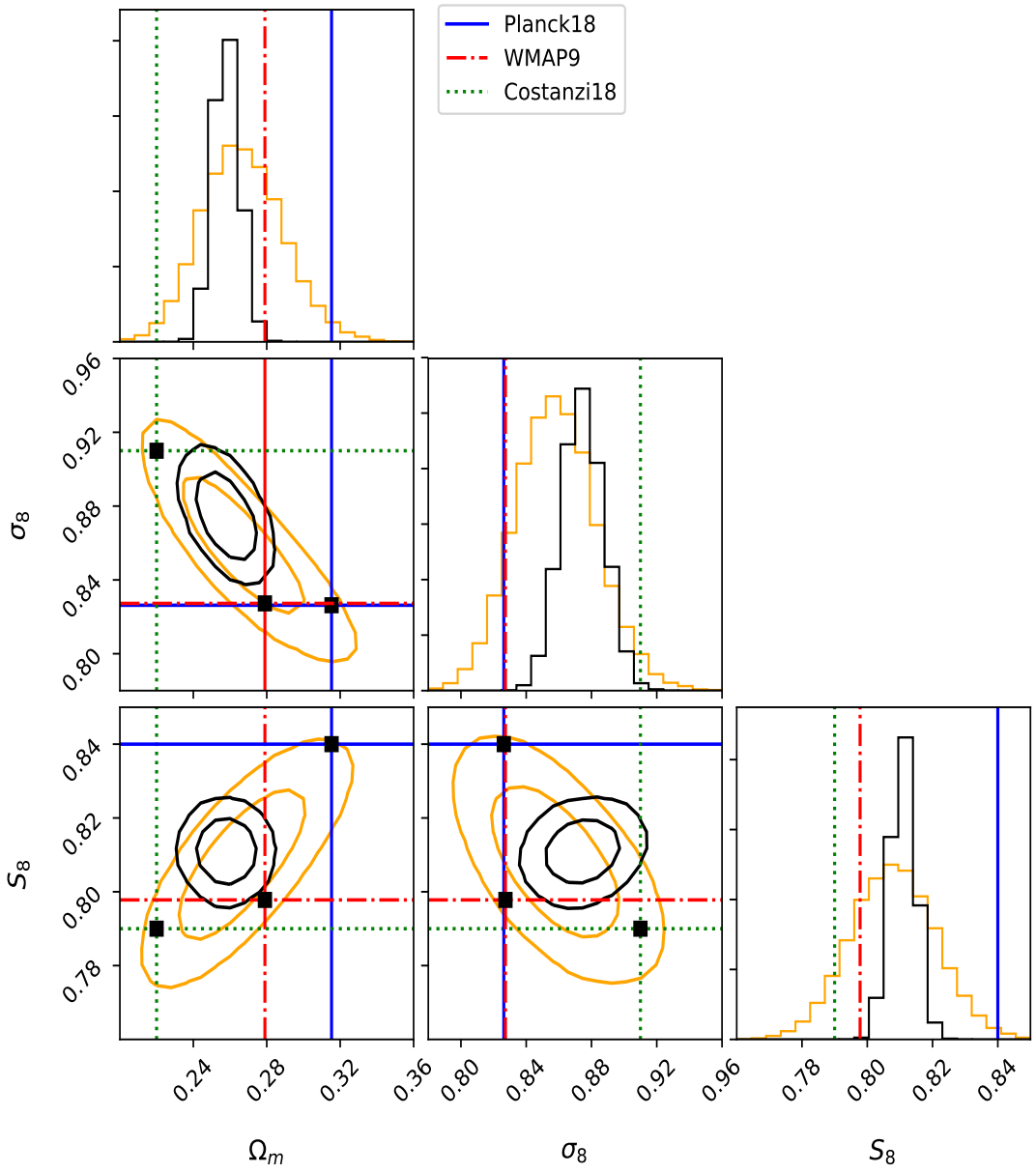

Figure 5.19: Visualization of the consistency between the confidence contours obtained by modelling $N(z, M)$ in Pipeline I, by considering the results obtained with the assumption of the minimum cut in mass $M_{min} = 5 \cdot 10^{13}$ $M_\odot$ h^{-1} (black plots), and the high mass regime (orange plots). We show the confidence contours at 68% and 95% in the parameter spaces defined by $\Omega_m - \sigma_8$, $\Omega_m - S_8$ and $\sigma_8 - S_8$, along with the marginalized histograms. The blue solid line represents the values of Planck18, the red dashed line represents WMAP9, while the green dotted line provides the values obtained by Costanzi et al. (2018).

5.8 Improving the analysis: *Pipeline II*

So far we have considered the case of counts as a function of the mass, M. However this approach has a drawback, since the mass is not an observable quantity. Moreover, we need to assume a cosmological model a priori in order to retrieve the mass for each object, since the scaling relation described in Eq. (4.18) depends on cosmology. In particular, to obtain the masses in this Thesis work we assume $h = 0.7$ and $\Omega_m = 0.30$.

To address this issue, we develop an alternative likelihood model for cluster number counts. We consider a widely-used approach adopted in literature works on cluster counts (e.g., Costanzi et al. 2018, Rozo et al. 2009), and introduce a new model that replaces the one described in Eq. (5.2), used in *Pipeline I*. This model has the following functional form:

$$\langle N(\Delta\lambda^*_{obs,i}, \Delta z_{obs,j})\rangle = \int_0^\infty \mathrm{d}z\ \Omega \frac{\mathrm{d}V}{\mathrm{d}z\mathrm{d}\Omega} \int_0^\infty \mathrm{d}M\ n(M,z)\ \cdot$$
$$\cdot \int_{\Delta\lambda^*_{obs,i},\,\Delta z_{obs,j}} \mathrm{d}\lambda^*_{obs}\mathrm{d}z_{obs}\ P(z_{obs}|z,\Delta\lambda^*_{obs,i})P(\lambda^*_{obs}|M,z_{obs})\,, \qquad (5.10)$$

where V is the volume, Ω is the effective survey area (377 deg^2 in our case), and $n(M,z)$ is the mass function, for which we assume the model by Tinker et al. (2008), as for the case of the model described in Section 5.2.1. This model depends on the observed values of intrinsic richnesses and redshifts, provided in the AMICO KiDS-DR3 catalogue, and it is integrated in the ranges $\Delta\lambda^*_{obs,i}$ and $\Delta z_{obs,j}$. In this case we do not perform Monte Carlo extractions, since we model directly the cluster counts as a function of the observed values of intrinsic richnesses and redshifts. The treatment of the errors on redshifts and scaling relation is accounted in the likelihood model, by means of the probability distributions $P(z_{obs}|z,\Delta\lambda^*_{obs,i})$ and $P(\lambda^*_{obs}|M,z_{obs})$. These distributions are assumed to be Gaussian in our case, and act as weights of the mass function within the integral.

The probability distribution $P(z_{obs}|z,\Delta\lambda^*_{obs,i})$ is retrieved from the mock catalogue developed by Maturi et al. (2018) (see Section 4.3). With this distribution in Eq. (5.10), we account for the redshift uncertainties. To compute the mean and the standard deviation of this distribution, we consider a grid of redshifts and intrinsic richnesses. However, the mock catalogue has been developed over the same effective area covered by the original catalogue, which is quite limited. It turns out that we do not have enough statistics in the bins if we consider both bins in intrinsic richness and redshift. We thus decide to consider $P(z_{obs}|z)$. This means that we neglect any dependence of the uncertainty on z_{obs} on the intrinsic richness. The probability distribution $P(z_{obs}|z)$ is then retrieved similarly to $P(z|z_{obs})$, used in *Pipeline I* to randomly extract the values of redshift.

With respect to the mean of $P(z_{obs}|z)$, we assume that it is equal to the value

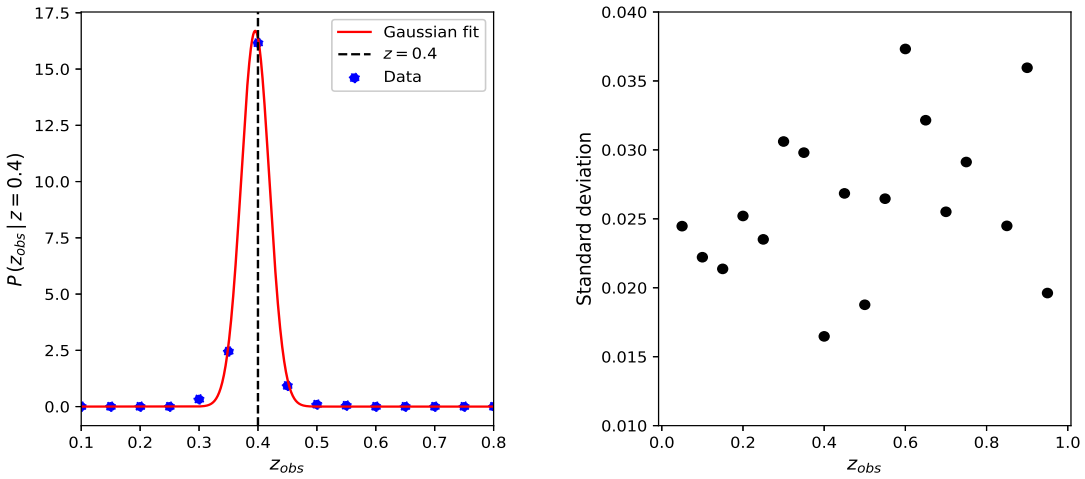

Figure 5.20: *Left panel:* probability distribution $P(z_{obs}|z)$ for the case of a bin central value of redshift equal to $z = 0.4$, retrieved from the mock catalogue. *Right panel:* values of the standard deviation of the probability distributions $P(z_{obs}|z)$.

of redshift z considered. This approximation is justified, as we can see in the left panel of Fig. 5.20. On the other hand, we have to take into account that the standard deviation of $P(z_{obs}|z)$ depends on redshift, as we can see in the right panel of Fig. 5.20. Therefore we perform a polynomial fit that describes the standard deviation as a function of z_{obs}.

On the other hand, $P(\lambda^*_{obs}|M, z_{obs})$ in Eq. (5.10) is a Gaussian that weights the theoretical prediction of the counts in accordance with the uncertainty on the observable-mass scaling relation. In order to retrieve a function to be integrated in the model, we need a functional form for the mean and the standard deviation of this distribution. Then we invert the scaling relation, Eq. (4.18), expliciting the observed intrinsic richness λ^*_{obs}. Firstly, we consider triplets of values of mass, M, observed redshift, z_{obs}, and Ω_m, namely $\{M_i, z_{obs,i}, \Omega_{m,i}\}$, on which we base the derivation of several distributions $P(\lambda^*_{obs,i}|M_i, z_{obs,i})$. Secondly, we scatter the values of the parameters α, β, γ in the scaling relation, through the use of Gaussian Monte Carlo extractions. Given the values $\{M_i, z_{obs,i}, \Omega_{m,i}\}$, and the new set of parameters $\{\alpha_k, \beta_k, \gamma_k\}$, we derive a value of intrinsic richness $\lambda^*_{obs,k}$ from the inverted scaling relation. Iterating the scatter of the parameters for a fixed set $\{M_i, z_{obs,i}, \Omega_{m,i}\}$, we obtain a distribution for $\lambda^*_{obs,i}$, with a given mean and standard deviation. Realizing several distributions, one for each set $\{M_i, z_{obs,i}, \Omega_{m,i}\}$, we perform a polynomial fit for the standard deviation as a function of the mass, the observed redshift and Ω_m. Conversely, given that we assessed the absence of relevant systematics, we set the mean of these distributions equal to the value of λ^*_{obs} derived by neglecting the uncertainty on the scaling relation.[4]

[4]The described procedure is a first attempt to derive the shape of the distribu-

We outline the importance of the dependency of the standard deviation on Ω_m. Indeed, this implies a direct relation between the error on the scaling relation and the cosmology assumed for the model. In this way, $P(\lambda^*_{obs}|M, z_{obs})$ changes at each step of the MCMC that we compute to derive the constraints on Ω_m, σ_8 and S_8.

5.9 Modelling $N(\lambda^*_{obs})$ in a ΛCDM Universe

Similarly to the case of the cluster counts as a function of the mass, we begin the analysis in the framework of *Pipeline II* by considering the counts in a given redshift bin, namely $N(\lambda^*_{obs})$. We show in Fig. 5.21 the cluster counts as a function of the observed intrinsic richness, λ^*_{obs}, with a common threshold $\lambda^*_{obs} = 23$, chosen in order to avoid the regime affected by Malmquist bias. As for the case of $N(M)$ described in Section 5.7.1, we can see an overall agreement with Planck18 and WMAP9.

Since the model defined in Eq. (5.10) depends on the observed redshifts and intrinsic richnesses, the *Pipeline II* does not require any Monte Carlo extraction. As a consequence, we can compare the constraints on Ω_m, σ_8 and S_8 retrieved in *Pipeline II* with those obtained assuming the model for $N(M)$, Eq. (5.2), in the case without extractions. This allows us to evaluate any remarkable difference in the results obtained by assuming the two models considered in this work. We point out that it is not possible to relate a secure value of mass M to a value of λ^*_{obs}, in a first instance because the scaling relation has an uncertainty, and in addition because the value of M provided by the scaling relation depends on the redshift. Therefore, to a value of λ^*_{obs} correspond diverse values of mass in a redshift bin. Nevertheless, we can fine-tune the choice of the minimum masses corresponding to the designated minimum intrinsic richnesses by making some assumptions. From the redshift distribution of the objects in the original catalogue within a given redshift bin, we consider the mean value of redshift. Then, neglecting the uncertainties on the scaling relation, we derive the value of M_{min}, for a given $\lambda^*_{obs,min}$ and a mean value of redshift. In Fig. 5.22 we can see that, both for the case of *Pipeline II* and the case of $N(M)$ without extractions, the posteriors on Ω_m, σ_8 and S_8 obtained in different bins of redshift show the same inconsistencies. Then we conclude that, considering the approximations applied to the probability distributions $P(z_{obs}|z, \Delta\lambda^*_{obs,i})$ and $P(\lambda^*_{obs}|M, z_{obs})$, the

tion $P(\lambda^*_{obs}|M, z_{obs})$. Indeed, we are assuming $P(\lambda^*_{obs}|M, z_{obs}) = P(M|\lambda^*_{obs}, z_{obs})$, where $P(M|\lambda^*_{obs}, z_{obs})$ is the scaling relation. Conversely, we should base ourselves on the Bayes' theorem, considering the scaling relation as the posterior. In turn, we should consider the prior on the intrinsic richness, $P(\lambda^*_{obs})$, and the evidence, which in this case is the mass function. Furthermore, it is necessary to account for the covariance between the parameters of the scaling relation, α, β, γ. This can be retrieved from the fit of the scaling relation. We will derive the improved functional form of $P(\lambda^*_{obs}|M, z_{obs})$ in the near future.

model for the counts on which the *Pipeline II* is based, Eq. (5.10), and the model as a function of the mass, Eq. (5.2), provide results that are in agreement on the cosmological parameters Ω_m, σ_8 and S_8.

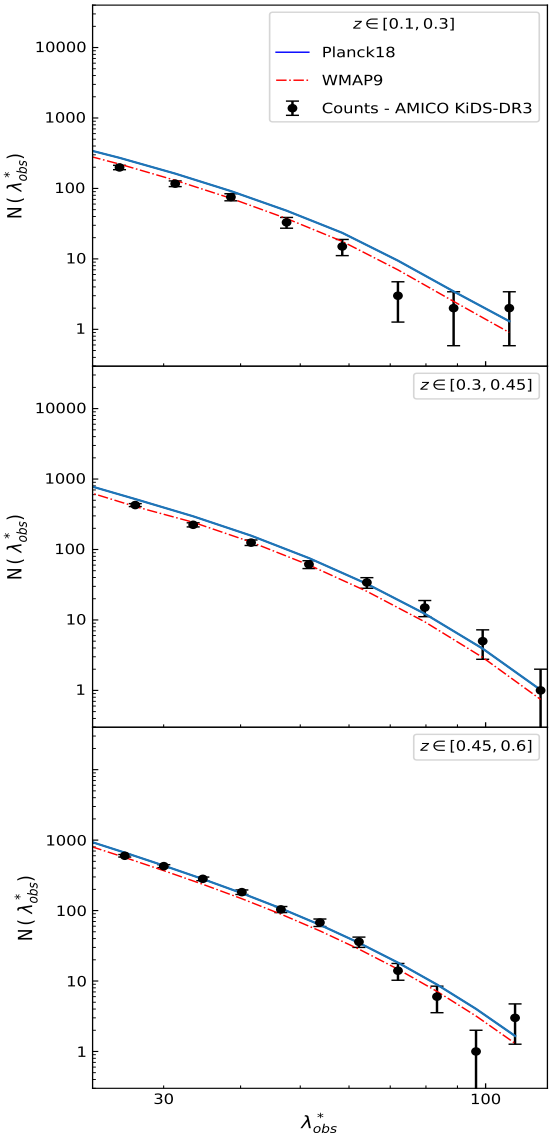

Figure 5.21: Counts of the galaxy clusters in the AMICO KiDS-DR3 catalogue as a function of the observed intrinsic richness, λ^*_{obs}, weighted for the selection function, in the redshift bins $z \in [0.1, 0.3]$, $[0.3, 0.45]$, $[0.45, 0.6]$. The common threshold in minimum intrinsic richness $\lambda^*_{obs,min} = 23$ is applied to all the redshift bins. The black dots represent the counts considered in the analysis. The error bars are referred to the Poissonian uncertainties relative to the weighted counts. The blue solid lines show the Planck18 prediction, while the dashed red lines are referred to WMAP9.

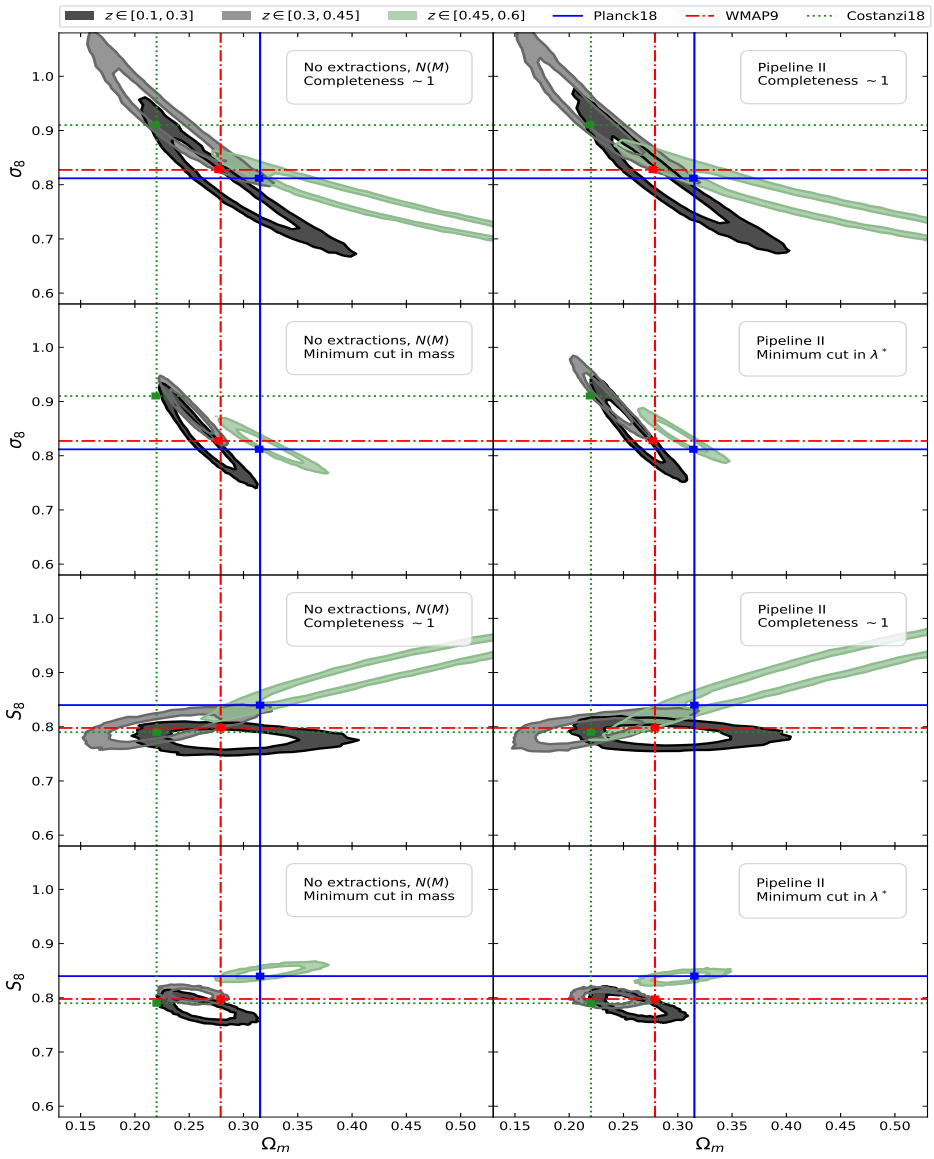

Figure 5.22: Confidence contours at 68% and 95% in the parameter spaces defined by $\Omega_m - \sigma_8$ (top four panels) and by $\Omega_m - S_8$ (bottom four panels), for the cases of completeness and purity $\simeq 1$ and minimum $M_{min} = 5 \cdot 10^{13}$ $M_\odot$ h^{-1}. The cases without extractions in the framework of $N(M)$ are shown on the left, while on the right we have the results from *Pipeline II*. The black, grey and green bands define the interval between the 68% and 95% confidence levels, respectively, for $z \in [0.1, 0.3]$, $[0.3, 0.45]$, $[0.45, 0.6]$. The blue solid lines represent the values of Planck18, the red dashed lines represent WMAP9 values, while the green dotted lines provide the values obtained by Costanzi18.

In Fig. 5.23 we show the values of σ_8 and Ω_m obtained in *Pipeline II*, for different values of minimum intrinsic richness. As we can see, the same arguments expressed in Section 5.7.1 with regard to the case of $N(M)$, hold also in this case: we find an agreement with the Planck18 and WMAP9 predictions in the redshift bins $z \in [0.1, 0.3]$, $z \in [0.45, 0.6]$, while in $z \in [0.3, 0.45]$ the values of σ_8 and Ω_m are consistent with Costanzi18. Furthermore, in the redshift bin $z \in [0.45, 0.6]$ we find the same behavior described in Fig. 5.10. The results on σ_8 and Ω_m, in this case, diverge from the predictions by Planck18, WMAP9 and Costanzi18 due to the low number of bins of λ^*_{obs} considered for the modelling.

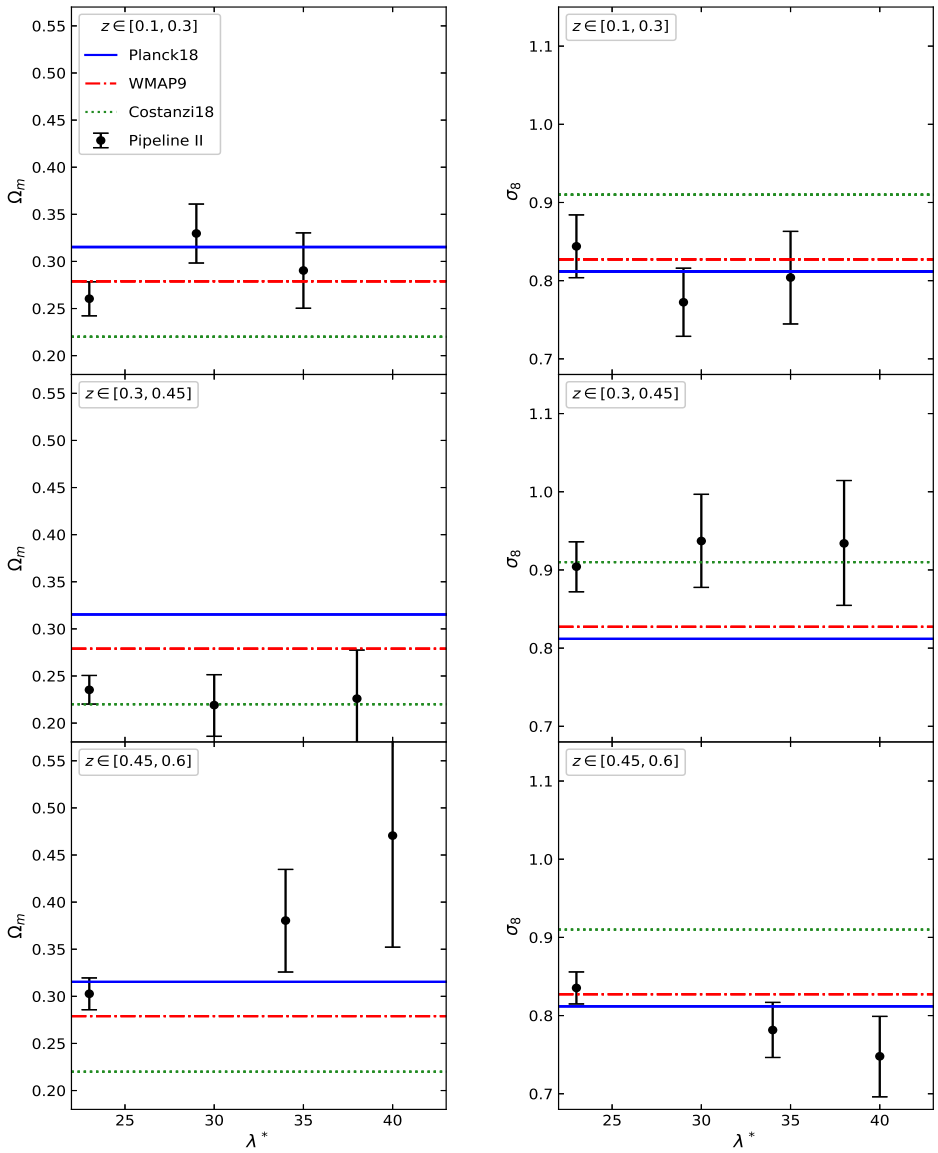

Figure 5.23: In the left panels, the best-fit values, provided in *Pipeline II*, of Ω_m obtained as the median values of the marginalized posterior, as a function of the minimum observed intrinsic richness $\lambda^*_{obs,min}$ considered in the analysis. On the right, the values of σ_8 as a function of $\lambda^*_{obs,min}$. The blue solid lines represent the values of Planck18, the red dashed lines represent WMAP9 values, while the green dotted lines provide the values obtained by Costanzi18.

5.9.1 Modelling the whole dataset in a ΛCDM Universe

Once we have considered the one-dimensional analysis in terms of $N(\lambda^*_{obs})$, we proceed with the modelling of $N(z_{obs}, \lambda^*_{obs})$. In Fig. 5.24 we can see that, similarly to the case of $N(z, M)$ described in Section 5.7.3, the confidence contours obtained by considering only the regime with completeness and purity ~ 1 are consistent with those obtained with the lowest cut in intrinsic richness, namely $\lambda^*_{obs,min} = 23$.

We obtain the following constraints for the case of completeness and purity $\simeq 1$:

$$\begin{cases} \Omega_m = 0.27^{+0.03}_{-0.02} \\ \sigma_8 = 0.85^{+0.03}_{-0.03} \\ S_8 = 0.81^{+0.01}_{-0.01} \end{cases} \tag{5.11}$$

For the case of $\lambda^*_{obs,min} = 23$, instead, we have:

$$\begin{cases} \Omega_m = 0.270^{+0.009}_{-0.009} \\ \sigma_8 = 0.864^{+0.014}_{-0.014} \\ S_8 = 0.820^{+0.004}_{-0.004} \end{cases} \tag{5.12}$$

In both cases, we can see that these results are remarkably consistent with those obtained by modelling $N(z, M)$ in *Pipeline I* (see Section 5.7.3). Therefore, the methods developed in the two pipelines considered in this Thesis work, lead to consistent results on the constraints on Ω_m, σ_8, S_8

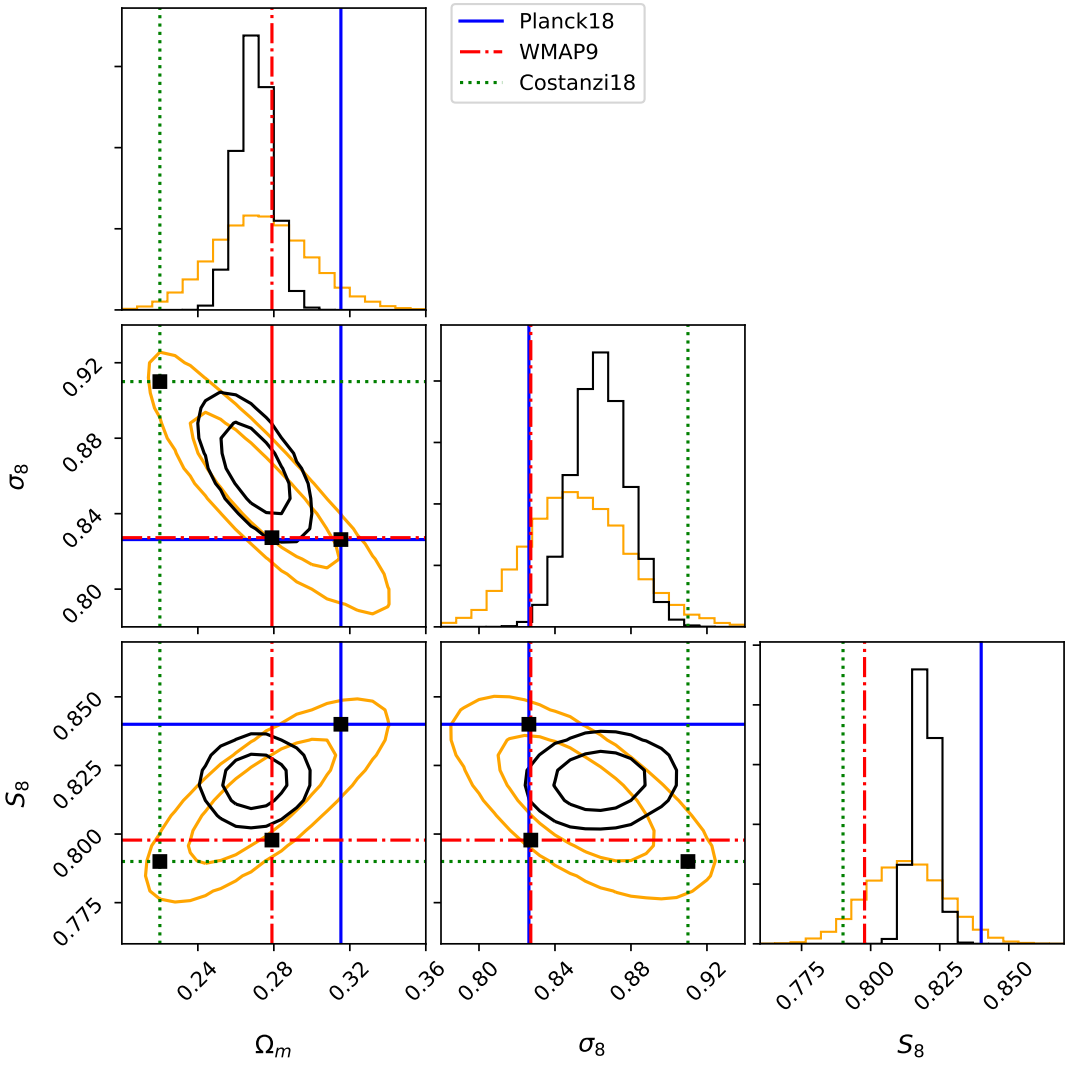

Figure 5.24: Visualization of the consistency between the confidence contours obtained by modelling $N(z_{obs}, \lambda^*_{obs})$ in Pipeline II, by considering the results obtained with the assumption of the minimum cut in intrinsic richness, $\lambda^*_{obs,min}$ (black plots), and the high richness regime (orange plots). We show the confidence contours at 68% and 95% in the parameter spaces defined by $\Omega_m - \sigma_8$, $\Omega_m - S_8$ and $\sigma_8 - S_8$, along with the marginalized histograms. The blue solid lines represent the values of Planck18, the red dashed lines represent WMAP9, while the green dotted lines provide the values obtained by Costanzi18.

5.10 Super sample covariance

As we outlined during the presentation of our results, we are neglecting several sources of uncertainty in the modelling of our data. However, we need large simulations in order to derive most of the additional contributions to include into the covariance matrix of our likelihood.

Nevertheless, among the sources of error to be considered in the likelihood function, we can include the most peculiar: the *super sample covariance* (SSC). Due to the limited portion of Universe observed, the measure of the background density of matter from a survey of galaxies can be intrinsically biased. Indeed, in the context of the description of the matter density in the Universe by means of Fourier modes, the local observables can be modulated by density fluctuations with wavelength larger than the survey size. That is, the sample derived from a survey could reflect a local overdensity or underdensity, implying a bad characterization of the mean background density of the Universe. The role of the SSC is to account for the fluctuations of the measured background density, parametrized as δ_b, with respect to the true value. In particular, for each bin of redshift, labeled as i, we will introduce a variable $\delta_{b,i}$.

To account for this contribution, we consider a new expression for the likelihood. Following Lima & Hu (2004) and Lacasa & Grain (2019), the new likelihood considered for the modelling of cluster number counts has the following functional form:

$$\mathcal{L} = \int \mathrm{d}\boldsymbol{\delta}_b^{n_z} \left[\prod_{i,j} \mathrm{Poiss}\left(N_{i,j} | \bar{N}_{i,j} + \frac{\partial N_{i,j}}{\partial \delta_{b,j}} \delta_{b,j} \right) \right] \cdot \mathrm{Gauss}(\boldsymbol{\delta}_b | 0, S)\,. \tag{5.13}$$

This likelihood is, thus, a convolution of a Poissonian likelihood, the first term of the integrand, and a Gaussian likelihood, the second term. In particular, the Poissonian likelihood describes the cluster counts, while, as we shall discuss, the Gaussian is referred to the SSC. In Eq. (5.13), i and j are the labels of the bins of observed intrinsic richness and redshift, in the framework of *Pipeline II*. As a consequence, $N_{i,j} \equiv N(\Delta\lambda^*_{obs,i}, \Delta z_{obs,j})$ is the observed cluster number counts in a bin of intrinsic richness and redshift, while $\bar{N}_{i,j}$ is the model defined in Eq. (5.10). The term $\partial N_{i,j}/\partial\delta_{b,j}$ is the response of the counts, the measure of how the counts vary with changes of the background density, and is expressed as

$$\begin{aligned} \frac{\partial N_{i,j}}{\partial \delta_{b,j}} = & \int_0^\infty \mathrm{d}z\ \Omega \frac{\mathrm{d}V}{\mathrm{d}z\mathrm{d}\Omega} \int_0^\infty \mathrm{d}M\ n(M,z)\, b(M,z)\ \cdot \\ & \cdot \int_{\Delta\lambda^*_{obs,i},\, \Delta z_{obs,j}} \mathrm{d}\lambda^*_{obs} \mathrm{d}z_{obs}\ P(z_{obs}|z, \Delta\lambda^*_{obs,i}) P(\lambda^*_{obs}|M, z_{obs})\,. \end{aligned} \tag{5.14}$$

That is, the response is equal the model described in Eq. (5.10), in which we also include the contribution of the linear bias $b(M,z)$. The mean of each Poissonian

distribution in Eq. (5.13) is perturbed by the product of this term and the density fluctuation $\delta_{b,j}$ defined in the j-th redshift bin.

Turning to n_z in Eq. (5.13), it is the number of redshift bins considered in the modelling procedure, and it defines the dimension of the integral. Considering for example three redshift bins at once, by modelling $N(z_{obs}, \lambda^*_{obs})$, we have three different integration variables $\delta_{b,j}$, with $j = 1, 2, 3$. Furthermore, each $delta_{b,j}$ is a variable of the Gaussian distribution in Eq. (5.13), which thus is multivariate in general. This Gaussian is centered on zero and has covariance matrix S, which has dimension $n_z \times n_z$. This matrix quantifies the covariance between the variables $\delta_{b,j}$ in the bins of redshift considered, and each element of S is expressed as

$$S_{j,j'} = \frac{1}{2\pi^2}\frac{1}{f_{sky}}\int \mathrm{d}k\ k^2 P(k)\frac{U_j(k)}{I_j}\frac{U_{j'}(k)}{I_{j'}}\ , \tag{5.15}$$

where $U_j(k)$ has the form

$$U_j(k) = \int \mathrm{d}V_j\ W_j^2(z_j) g(z_j) j_0(k r_j), \tag{5.16}$$

while I_j is expressed as

$$I_j = \int \mathrm{d}V_j\ W_j^2(z_j). \tag{5.17}$$

In these equations, V_j is the comoving volume within the j-th redshift bin, $P(k)$ is the linear power spectrum, g is the linear growth factor of the perturbations, j_0 is the Bessel spherical function, and the terms W_i refer to the window functions, assumed as top-hat in our case. Lastly, f_{sky} is the sky fraction covered by the survey, defined by the effective area which in our case is 377 deg^2.

In order to implement the formalism for $S_{j,j'}$ in our C++ libraries, the CosmoBolognaLib, we referred to the codes in Python provided by Lacasa & Grain (2019). In our analysis, we do not explicitly compute the integral in Eq. (5.13). Conversely, we assume the natural logarithm of another likelihood $\mathcal{L}'$, corresponding to the integrand of Eq. (5.13), namely

$$\ln \mathcal{L}' = \ln \left[\prod_{i,j} \mathrm{Poiss}\left(N_{i,j} | \bar{N}_{i,j} + \frac{\partial N_{i,j}}{\partial \delta_{b,j}} \delta_{b,j} \right) \cdot \mathrm{Gauss}(\boldsymbol{\delta}_b | 0, S) \right]. \tag{5.18}$$

Therefore we set $\boldsymbol{\delta}_b = \{\delta_{b,1}, ..., \delta_{b,n_z}\}$ as free parameters of the model, with Gaussian priors defined by the diagonal of the S matrix. Since the S matrix depends on the cosmological parameters Ω_m and σ_8, the values of its elements change at every step of the chain, which is computed in order to derive the posteriors of Ω_m and σ_8. In turn, a variation of S implies the change of the prior on $\boldsymbol{\delta}_b$. At the end of the chains, we marginalize over $\boldsymbol{\delta}_b$ to derive the posteriors of our parameters of interest.

5.10.1 Including the SSC in *Pipeline II*

In order to obtain the most reliable results, we make use of *Pipeline II*. Therefore, in this framework, we consider the additional contribution of the SSC, which takes place in the likelihood function, as discussed in the previous section. We consider in a first instance the modelling of $N(\lambda^*_{obs})$ in a given bin of redshift. As we can see in Fig. 5.25, where we show the case of the first redshift bin as an example, the inclusion of the SSC in the modelling provides the same results obtained in the case of a simple Poissonian likelihood. Then, the perturbations of the Poissonian probability functions in Eq. (5.13) are negligible, along with the contribution of the Gaussian.

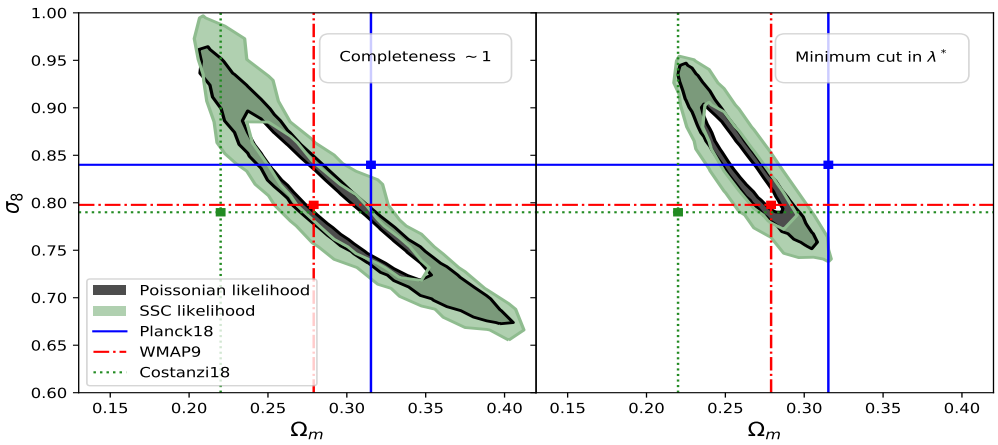

Figure 5.25: Comparison of the confidence contours obtained from the assumption of a Poissonian likelihood (black bands) and a SSC likelihood (green bands), in the case of the modelling of $N(\lambda^*_{obs})$ in the redshift bin $z \in [0.1, 0.3]$. On the left we show the confidence contours obtained by considering the pure and complete regime, while the case for the lowest cut in intrinsic richness is shown on the right. Despite the confidence contours obtained by considering the SSC seem to be larger, we do not rely on this feature for the moment.

Conversely, by modelling $N(\lambda^*_{obs}, z_{obs})$, that is by considering simultaneously in the modelling the three redshift bins $z \in [0.1, 0.3]$, $[0.3, 0.45]$, $[0.45, 0.6]$, it turns out that the SSC produces a systematic shift of the confidence contours along the direction of the $\Omega_m - \sigma_8$ degeneracy, namely along S_8. This effect is shown in Fig. 5.26. The reason of these results resides in the S matrix in Eq. (5.13). When we consider only one bin of redshift, S is a scalar, and we see that this does not produce remarkable differences. When we consider more than one bin of redshift, instead, the terms out of the diagonal in the S matrix produce visible differences. In the case of the modelling of $N(\lambda^*_{obs}, z_{obs})$, including the SSC, we

obtain the following constraints on Ω_m, σ_8 and S_8:

$$\begin{cases} \Omega_m = 0.28^{+0.01}_{-0.01} \\ \sigma_8 = 0.85^{+0.02}_{-0.01} \\ S_8 = 0.82^{+0.01}_{-0.01} \end{cases} \tag{5.19}$$

We consider this as our best result, obtained by including 2816 objects.

Lastly, we point out that the SSC produces the same effects in the case of the cluster counts as a function of the mass M, namely by assuming the model described in Eq. (5.2). The reason is that, as we have discussed in Section 5.9, both the model for the cluster counts as a function of the mass and as a function of the intrinsic richness describe the observations in a very similar fashion. Then, the effects of the SSC in our work only depend on the covariance between the redshift bins, that changes as a function of the cosmological parameters, and on the assumed likelihood function for the description of the cluster counts, which in this work is always Poissonian.

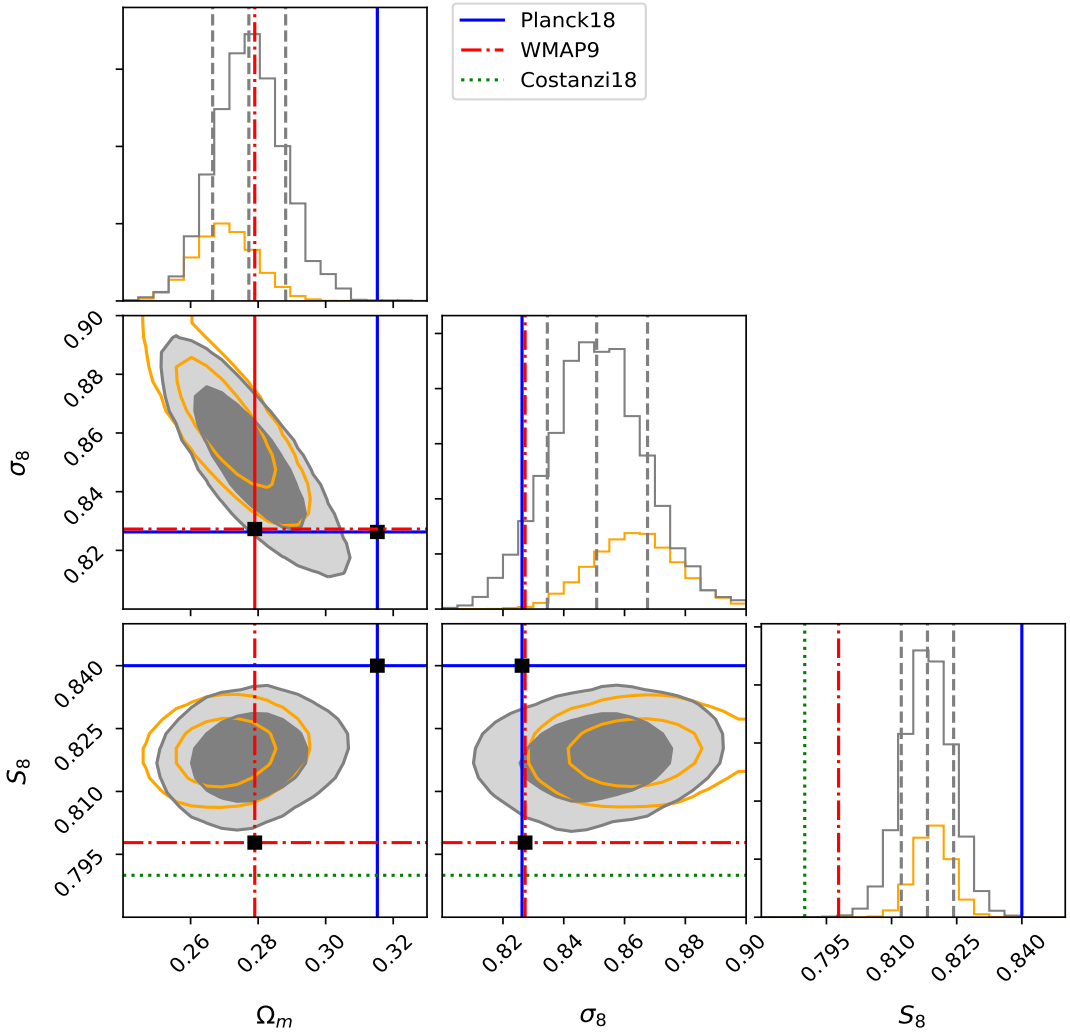

Figure 5.26: Comparison of the confidence contours obtained from the assumption of a Poissonian likelihood (orange contours) and a SSC likelihood (grey filled contours), in the case of the modelling of $N(\lambda^*_{obs}, z_{obs})$ for a cut in minimum intrinsic richness $\lambda^*_{obs,min} = 23$. The blue solid lines represent the values of Planck18, the red dashed lines represent WMAP9 values, while the green dotted lines provide the values obtained by Costanzi18.

Chapter 6

Discussion and conclusion

According to the ΛCDM cosmological model, the large-scale structure of the Universe results from the gravitational growth of local density perturbations, within an expanding Universe. Galaxy clusters are the tracers of the highest of such perturbations, and the development of advanced instrumentation, along with the combination of observations of galaxy clusters in different wavelengths, steadily enhance our knowledge of the Universe on large scales. Observations in X-rays, optical, NIR and also gravitational lensing studies allow to investigate in depth the properties of these objects. In this framework, it is necessary to construct pure and complete galaxy cluster catalogues up to high redshifts, in order to derive cosmological constraints from the physical properties of these structures.

In this Thesis we carried out a work on cluster counts based on a photometric catalogue of galaxy clusters, the AMICO KiDS-DR3 catalogue. The final sample consists of three redshift bins, $z \in [0.1, 0.3]$, $z \in [0.3, 0.45]$, $z \in [0.45, 0.6]$, in an effective area of 377 deg^2. Considering the intrinsic richness, λ^*, as our mass proxy, we performed an accurate analysis of the sample by making use of a scaling relation between the mass, M, and λ^*, calibrated on the objects of dataset. In this way we carried out an analysis by considering two different approaches, or pipelines, in order to derive the cosmological parameters Ω_m, σ_8 and S_8, assuming a ΛCDM model. As detailed in Chapter 5, the main results of this Thesis work can be summarized as follows:

- We carried out the analysis in the framework of the *Pipeline I*, based on the treatment of the uncertainties on redshifts and scaling relation by means of Monte Carlo extractions. In a first instance, we focused on the one-dimensional modelling, namely the counts as a function of the mass in a bin of redshift, $N(M)$. We found a good agreement between the constraints on cosmological parameters obtained with this method, and those obtained without performing Monte Carlo extractions. In addition, we found results in agreement with the results obtained in Planck18, WMAP9 and Cost-

anzi18.

- Focusing on the confidence contours and on the marginalized posteriors of the parameters Ω_m, σ_8 and S_8, we found a general inconsistency between the results in different bins of redshift.

- Considering the bi-dimensional modelling, $N(z, M)$, we derived constraints from the whole dataset. We obtained the following results by considering only the mass regime not affected by incompleteness and impurity:

$$\begin{cases} \Omega_m = 0.27^{+0.02}_{-0.02} \\ \sigma_8 = 0.86^{+0.02}_{-0.02} \\ S_8 = 0.81^{+0.01}_{-0.01} \end{cases} \tag{6.1}$$

  By considering the case of the lowest cut in minimum mass, instead, we found:

$$\begin{cases} \Omega_m = 0.258^{+0.007}_{-0.007} \\ \sigma_8 = 0.875^{+0.013}_{-0.013} \\ S_8 = 0.811^{+0.004}_{-0.004} \end{cases} \tag{6.2}$$

- Subsequently, we developed a new pipeline, namely *Pipeline II*, by introducing a new model for the theoretical description of cluster counts, based on two probability distributions which account for the uncertainties on the photometric redshifts and on the scaling relation. This model is a function of the observed intrinsic richness λ^*_{obs}, instead of the mass. By performing the one-dimensional analysis in a given redshift bin, we found that this new model provides constraints on the cosmological parameters that are in agreement with the model assumed for the *Pipeline I*.

- Then we modelled the entire dataset, and by accounting for the objects in the regime of completeness and purity $\simeq 1$, we found the following constraints:

$$\begin{cases} \Omega_m = 0.27^{+0.03}_{-0.02} \\ \sigma_8 = 0.85^{+0.03}_{-0.03} \\ S_8 = 0.81^{+0.01}_{-0.01} \end{cases} \tag{6.3}$$

  On the other hand, we found the following results on the cosmological parameters by considering

$$\begin{cases} \Omega_m = 0.270^{+0.009}_{-0.009} \\ \sigma_8 = 0.864^{+0.014}_{-0.014} \\ S_8 = 0.820^{+0.004}_{-0.004} \end{cases} \tag{6.4}$$

  Therefore, we found that *Pipeline I* and *Pipeline II* provide consistent results.

- Lastly, we introduced the super sample covariance in the analysis, by developing a new framework for the likelihood function. We found an interesting effect in the case of the bi-dimensional modelling of the whole dataset, consisting in a shift of the confidence contours in the parameter space $\Omega_m - \sigma_8$ along the S_8 direction. In this case, we found the following results:

$$\begin{cases} \Omega_m = 0.28^{+0.01}_{-0.01} \\ \sigma_8 = 0.85^{+0.02}_{-0.01} \\ S_8 = 0.82^{+0.01}_{-0.01} \end{cases} \tag{6.5}$$

These results represent our final best constraints obtained in this Thesis work. They are fully consistent with ΛCDM predictions, and competitive, in terms of uncertainties, with results of state-of-the-art cluster number count analyses.

In order to improve the analysis, in the near future we will perform new simulations aimed at assessing the uncertainty on the selection function. Furthermore, we will analyze the data from the weak-lensing analysis in order to better characterize the probability distribution $P(\lambda^*_{obs}|M, z_{obs})$ in the model defined in Eq. (5.10).

Bibliography

[1] P. Coles, F. Lucchin, *Cosmology, The Origin and Evolution of Cosmic Structure*, 2002, WILEY

[2] *Principles of Physical Cosmology*, 1993, Princeton University Press

[3] B. Ryden, *Introduction to Cosmology*, 2017, Cambridge University Press

[4] Siegfried Röser, *From Cosmological Structures to the Milky Way*, 2005, WILEY-VCH

[5] A. Einstein, *Zur allgemeinen Relativitätstheorie*, 1915, Sitzungsberichte der Königlich Preußischen Akademie der Wissenschaften (Berlin), Seite 778-786

[6] E. Hubble, *A Relation between Distance and Radial Velocity among Extra-Galactic Nebulae*, 1929, Proceedings of the National Academy of Sciences of the United States of America, Volume 15, Issue 3, pp. 168-173

[7] G. Lemaître, *Un Univers homogène de masse constante et de rayon croissant rendant compte de la vitesse radiale des nébuleuses extra-galactiques*, 1927, Annales de la Société Scientifique de Bruxelles A47: p. 49-59

[8] Planck Collaboration, *Planck 2018 results. VI. Cosmological parameters*, 2018, arXiv:1807.06209

[9] Suhail Dhawan, Saurabh W. Jha, Bruno Leibundgut, *Measuring the Hubble constant with Type Ia supernovae as near-infrared standard candles*, 2018, arXiv:1707.00715v2

[10] Adam G. Riess, Stefano Casertano, Wenlong Yuan, Lucas M. Macri, Dan Scolnic, *Large Magellanic Cloud Cepheid Standards Provide a 1% Foundation for the Determination of the Hubble Constant and Stronger Evidence for Physics Beyond LambdaCDM*, 2019, arXiv:1903.07603v2

[11] A. Friedmann, *Über die Krümmung des Raumes*, 1922, Zeitschrift für Physik, Volume 10, pp. 377-386

[12] A. Riess et al., *Observational Evidence from Supernovae for an Accelerating Universe and a Cosmological Constant*, 1998, The Astronomical Journal, Volume 116, Issue 3, pp. 1009-1038

[13] Mo H. J., White S. D. M. *An analytic model for the spatial clustering of dark matter haloes*, 1996, MNRAS, 282, 347

[14] T. X. Thuan, Y. I. Izotov *Big Bang nucleosynthesis and the baryonic content of the universe*, 2000, arXiv:astro-ph/0012382

[15] A. Linde, *Inflationary Cosmology*, 2007, arXiv:0705.0164

[16] Press, William H.; Schechter, Paul, *Formation of Galaxies and Clusters of Galaxies by Self-Similar Gravitational Condensation*, 1974, ApJ 187, pp. 425–438.

[17] M. Chevallier and D. Polarski, *Accelerating Universes with Scaling Dark Matter*, 2001, International Journal of Modern Physics D, vol. 10, pp. 213–223

[18] E. V. Linder, *Exploring the Expansion History of the Universe*, 2003, Physical Review Letters, vol. 90

[19] F. Zwicky, *Die Rotverschiebung von extragalaktischen Nebeln*, 1933, Helvetica Physica Acta, Vol. 6, p. 110-127

[20] A. Cavaliere, R. Fusco-Femiano, *X-rays from hot plasma in clusters of galaxies*, 1976, Astronomy and Astrophysics, vol. 49

[21] G. O. Abell, *The Distribution of Rich Clusters of Galaxies*, 1958, Astrophysical Journal Supplement, vol. 3, p.211

[22] R. G. Bower, J. R. Lucey, R. S. Ellis, *Precision photometry of early-type galaxies in the Coma and Virgo clusters: A test of the universality of the colour-magnitude relation. I - The data. II. Analysis*, 1992, MNRAS, vol. 254, p. 589-613

[23] E. S. Rykoff et al., *redMaPPer I: Algorithm and SDSS DR8 Catalog*, 2014, ApJ

[24] R. A. Sunyaev, Ya. B. Zeldovich, *The Observations of Relic Radiation as a Test of the Nature of X-Ray Radiation from the Clusters of Galaxies*, 1972, Comments on Astrophysics and Space Physics, Vol. 4, p.173

[25] K. Vanderlinde et al., *Galaxy Clusters Selected with the Sunyaev-Zel'dovich Effect from 2008 South Pole Telescope Observations*, 2010, ApJ, vol. 722

[26] T. A. Marriage et al., *The Atacama Cosmology Telescope: Sunyaev Zel'dovich Selected Galaxy Clusters at 148 GHz in the 2008 Survey*, 2011, ApJ, vol. 737

[27] Jens Erler, Kaustuv Basu, Jens Chluba, Frank Bertoldi, *Planck's view on the spectrum of the Sunyaev-Zeldovich effect*, 2018, MNRAS, vol. 476

[28] L. Grego et al., *Galaxy Cluster Gas Mass Fractions from Sunyaev-Zeldovich Effect Measurements: Constraints on* Ω_m, 2000, ApJ

[29] J. E. Carlstrom, G. P. Holder, E. D. Reese, *Cosmology with the Sunyaev-Zel'dovich Effect*, 2002, Annual Review of Astronomy and Astrophysics, Vol. 40, p. 643-680

[30] A. C. Fabian, *Cooling Flows in Clusters of Galaxies*, 1994, Annual Review of Astronomy and Astrophysics, Volume 32, 1994, pp. 277-318

[31] H. Böhringer et al., *XMM-Newton observations of M 87 and its X-ray halo*, 2001, A& A 365, L181-L187

[32] J. R. Peterson et al., *X-ray imaging spectroscopy of Abell 1835*, 2001, A& A 365, L104-9

[33] J. C. Vernaleo, C. S. Reynolds, *AGN Feedback and Cooling Flows: Problems with Simple Hydrodynamic Models*, 2006, ApJ, vol. 645, no. 1

[34] S. Borgani, *Cosmology with clusters of galaxies*, 2006, arXiv:astro-ph/0605575

[35] A. Mana et al., *Combining clustering and abundances of galaxy clusters to test cosmology and primordial non-Gaussianity*, 2014, MNRAS, vol. 434, p. 684–695

[36] F. Marulli, A. Veropalumbo, L. Moscardini, A. Cimatti, K. Dolag, *Redshift-space Distortions of Galaxies, Clusters and AGN*, 2017, A& A, vol. 599

[37] H. Park et al., *Alcock-Paczynski Test with the Evolution of Redshift-Space Galaxy Clustering Anisotropy*, 2019, ApJ, vol. 881, no. 2

[38] Y. J. Xue, X. P. Wu, *The* $L_X - T$, $L_X - \sigma$, *and* $\sigma - T$ *Relations for Groups and Clusters of Galaxies*, 2000, ApJ, 538, 65

[39] S. W. Allen, A. E. Evrard, A. B. Mantz, *Cosmological Parameters from Observations of Galaxy Clusters*, 2011, Annual Review of Astronomy and Astrophysics, vol. 49, pp 409-470

[40] T. Reiprich, H. Böhringer, *The Mass Function of an X-Ray Flux-limited Sample of Galaxy Clusters*, 2002, ApJ, 567, 716

[41] J. R. Bond, S. Cole, G. Efstathiou, N. Kaiser, *Excursion set mass functions for hierarchical Gaussian fluctuations*, 1991, ApJ, vol. 379, p. 440-460

[42] R. K. Sheth, G. Tormen, *Large-scale bias and the peak background split*, 1999, vol. 308, p. 119-126

[43] M. Costanzi et al., *Dark Energy Survey Year 1 Results: Methods for Cluster Cosmology and Application to the SDSS*, 2018, arXiv:1810.09456

[44] F. Pacaud et al., *The XXL Survey XXV. Cosmological analysis of the C1 cluster number counts*, 2018, arXiv:1810.01624

[45] Bellagamba F., Maturi M., Hamana T., Meneghetti M., Miyazaki S., Moscardini L., *Optimal filtering of optical and weak lensing data to search for galaxy clusters: application to the COSMOS field*, 2011, MNRAS, 413, 1145

[46] Fabio Bellagamba, Mauro Roncarelli, Matteo Maturi, Lauro Moscardini, *AMICO: optimised detection of galaxy clusters in photometric surveys*, 2018, arXiv:1705.03029v2

[47] Matteo Maturi, Fabio Bellagamba, Mario Radovich, Mauro Roncarelli, Mauro Sereno, Lauro Moscardini, Sandro Bardelli, Emanuella Puddu, *AMICO galaxy clusters in KiDS-DR3: sample properties and selection function*, 2019, MNRAS, vol. 485, pp. 498-512

[48] R. Laureijs et al., *Euclid Definition Study Report*, 2011, arXiv:1110.3193

[49] Schechter P., *An analytic expression for the luminosity function for galaxies*, 1976, ApJ, 203, 297

[50] Navarro J. F., Frenk C. S., White S. D. M., *A Universal Density Profile from Hierarchical Clustering*, 1997, ApJ, 490, 493

[51] de Jong J. T. A., et al., *The third data release of the Kilo-Degree Survey and associated data products*, 2017, A& A, 604, A134

[52] Kuijken K., *OmegaCAM: ESO's Newest Imager*, 2011, The Messenger, 146, 8

[53] Capaccioli M., Schipani P., *The VLT Survey Telescope Opens to the Sky: History of a Commissioning*, 2011, The Messenger, 146, 2

[54] Driver S. P., et al., *GAMA: towards a physical understanding of galaxy formation*, 2009, Astronomy and Geophysics, 50, 5.12

[55] Driver S. P., et al., *Galaxy and Mass Assembly (GAMA): survey diagnostics and core data release*, 2011, MNRAS, 413, 971

[56] Liske J., et al., *Galaxy And Mass Assembly (GAMA): end of survey report and data release 2*, 2015, MNRAS, 452, 2087

[57] Fabio Bellagamba, Mauro Sereno, Mauro Roncarelli, Matteo Maturi, Mario Radovich, Sandro Bardelli, Emanuella Puddu, Lauro Moscardini, Fedor Getman, Hendrik Hildebrandt and Nicola Napolitano, *AMICO galaxy clusters in KiDS-DR3: weak-lensing mass calibration*, 2019, arXiv:1810.02827v2

[58] Medezinski E., et al., *Planck Sunyaev-Zel'dovich Cluster Mass Calibration using Hyper Suprime-Cam Weak Lensing*, 2017, preprint, arXiv:1706.00434

[59] Federico Marulli, Alfonso Veropalumbo, Michele Moresco, *CosmoBolognaLib: C++ libraries for cosmological calculations*, 2016, &C, 14, 35

[60] Federico Marulli, et al., The XXL Survey. XVI. The clustering of X-ray selected galaxy clusters at z 0.3, 2018, A&A, 620, 1

[61] Tinker, J., Kravtsov, A. V., Klypin, A., et al., *Toward a Halo Mass Function for Precision Cosmology: The Limits of Universality*, 2008, ApJ, 688, 709

[62] Watson, W. A., Iliev, I. T., D'Aloisio, A., et al., *The halo mass function through the cosmic ages*, 2013, MNRAS, 433, 12

[63] Despali, G., Giocoli, C., Angulo, R. E., et al., *The universality of the virial halo mass function and models for non-universality of other halo definitions*, 2016, MNRAS, 456, 248

[64] Stanek, R., Rudd, D., Evrard, A. E., *The effect of gas physics on the halo mass function*, 2009, MNRAS, 394, L11

[65] Velliscig, M., van Daalen, M. P., Schaye, J., et al., *The impact of galaxy formation on the total mass, mass profile and abundance of haloes*, 2014, MNRAS, 442, 2641

[66] Bocquet, S., Saro, A., Dolag, K., Mohr, J. J., *Halo mass function: baryon impact, fitting formulae, and implications for cluster cosmology*, 2016, MNRAS, 456, 2361

[67] Goodman J. & Weare J., *Ensemble samplers with affine invariance*, 2010, Comm. App. Math. Comp. Sci., 5, 65

[68] G. Hinshaw et al., *Nine-year Wilkinson Microwave Anisotropy Probe (WMAP) Observations: Cosmological Parameter Results*, 2013, arXiv:1212.5226

[69] E. Rozo et al., *Cosmological Constraints from the SDSS maxBCG Cluster Catalog*, 2009, ApJ, vol. 708, n. 1